Variability of Coastal Upwelling South of Madagascar

Heriniaina Juliano Dani Ramanantsoa

Thesis presented for the degree of

DOCTOR OF PHILOSOPHY

Department of Oceanography
UNIVERSITY OF CAPE TOWN
South Africa

May 2018

I confirm that I have been granted permission by the University of Cape Town's Doctoral Degrees Board to include the following publication(s) in my PhD thesis, and where co-authorships are involved, my co-authors have agreed that I may include the publication(s):

Ramanantsoa, J.D., Krug, M., Penven, P., Rouault, M. and Gula, J., 2018. Coastal upwelling south of Madagascar: Temporal and spatial variability. *Journal of Marine Systems*, 178, pp.29-37. Doi: 10.1016/j.jmarsys.2017.10.005.

Ramanantsoa, J.D., Penven, P., Krug, M., Gula, J. and Rouault, M., 2018. Uncovering a New Current: The Southwest MAdagascar Coastal Current. *Geophysical Research Letters*, 45(4), pp.1930-1938. Doi: 10.1002/2017GL075900.

SIGNATURE:.....DATE: 30 May 2018

NAME: Heriniaina Juliano Dani Ramanantsoa.....STUDENT NUMBER: RMNJUL001

I dedicate this work to my Parents, Julienne and Henri Ramanantsoa.

Abstract

Madagascar's southern coastal marine zone is a region of high biological productivity which supports a wide range of marine ecosystems, including fisheries. This high biological productivity is attributed to coastal upwelling. The thesis seeks to characterise the variability of the coastal upwelling south of Madagascar.

The first part of the thesis provides new insights on the structure, variability and drivers of the coastal upwelling south of Madagascar. Satellite remote sensing is used to characterize the spatial extent and strength of the coastal upwelling. A front detection algorithm is applied to thirteen years of Multi-scale Ultra-high Resolution (MUR) Sea Surface Temperatures (SST) and an upwelling index is calculated. The influence of winds and ocean currents as drivers of the upwelling are investigated using satellite, in-situ observations, and a numerical model. Results reveal the presence of two well-defined upwelling cells. The first cell (Core 1) is located in the southeastern corner of Madagascar, and the second cell (Core 2) is west of the southern tip of Madagascar. These two cores are characterized by different seasonal variability, different intensities, different upwelled water mass origins, and distinct forcing mechanisms. Core 1 is associated with a dynamical upwelling forced by the detachment of the East Madagascar Current (EMC), which is reinforced by upwelling favourable winds. Core 2 which appears to be primarily forced by upwelling favourable winds, is also influenced by a poleward eastern boundary flow coming from the Mozambique Channel. This intrusion of Mozambique Channel warm waters could result in an asynchronicity in seasonality between upwelling surface signature and upwelling favourables winds.

The second part of the thesis focuses on the interaction between the intrusion of warm water from Mozambique channel and the upwelling cell in Core 2. Cruise datasets, satellite remote sensing observations and model data analyses are combined to highlight the existence of a coastal surface poleward flow in the south-west of Madagascar: the South-west MAdagascar

Coastal Current (SMACC). The SMACC is a relatively shallow (<300 m) and narrow (<100 km wide) warm and salty coastal surface current, which flows along the south western coast of Madagascar toward the south, opposite to the dominant winds. The warm water surface signature of the SMACC extends from 22°S (upstream) to 26.4°S (downstream). The SMACC exhibits a seasonal variability: more intense in summer and reduced in winter. The average volume transport of its core is about 1.3 Sv with a mean summer maximum of 2.1 Sv. It is forced by a strong cyclonic wind stress curl associated with the bending of the trade winds along the southern tip of Madagascar. The SMACC directly influences the coastal upwelling regions south of Madagascar. Its existence is likely to influence local fisheries and larval transport patterns, as well as the connectivity with the Agulhas Current, affecting the returning branch of the global overturning circulation.

The last part of the thesis provides a holistic understanding of the inter-annual variability of the upwelling cells associated with the multiple forcing mechanisms defined in the first two parts of this work. Results reveal that the upwelling cells, Core 1 and Core 2, have different inter-annual variabilities. Inter-annual variability of Core 1 is associated with the East Madagascar Current (EMC) while Core 2 is linked with the South-west MAdagascar Coastal Current (SMACC). Inter-annual changes in the EMC occur as a result of oscillations in the South Equatorial Current (SEC) bifurcation off Madagascar, while the inter-annual variability in the SMACC is influenced by the cyclonic wind stress curl inter-annual variability. The upwelling is also linked with global/regional climate modes. Both Cores are highly correlated with the Subtropical Indian Ocean Dipole (SIOD). Core 2 is also correlated to the Indian Ocean Dipole (IOD). Both cores are significantly correlated with the El Niño-Southern Oscillation (ENSO) after 12 months lag.

Acknowledgements

Fitiavan'Andrimanitra no maha toy izao ahy (*Divine's loves carried me to be better*)... I am grateful to the God for the wellbeing, strength and wisdom that were necessary to complete this thesis.

This thesis should not be possible without my supervisors. I am deeply thankful to my supervisors who guided, supported and encouraged throughout my PhD. Thank you, Dr Marjolaine Krug, I highly appreciate your helps, patience of teaching, and carrying me all the way to make me like this today. Thank you, Prof Mathieu Rouault, for giving the opportunity to undertake a PhD, for your precious advices, and financial support that you provided. Thank you, Prof Pierrick Penven, for being more as a friend than a supervisor. Working with you was the key of my PhD. Thank you, Dr Jonathan Gula, for helping me without compromises and have accepted to share your precious experiences to refine my PhD.

I would like to thank University of Cape Town which supports myself during my PhD through a scholarship. I would also like to thank the Department of Oceanography which allowed me to use the departmental resources to make this PhD possible.

I wish to express my sincere thanks to the following institutions who supported myself during my scientific mobilities, conferences and technical accessories needed to conduct the PhD: Nansen-Tutu center, ICEMASA, Sarchi-Chair Climate and Modelling, RAMI, LABEX-MER, LOPS, WIOMSA, IOC-UNESCO-Africa and the IH.SM.

I would like to express my endless gratitude to my parent, Julienne and Henri Ramanantsoa, who have transmitted the highest knowledge: the Wisdom. Your wisdoms directed me all the way to see problems as an opportunity helping me to achieve this challenge.

I am also using this opportunity to express my gratitude to everyone who supported throughout this thesis. I can not list all of them because of the worry to forget someone.

Misaotra bevata (*Thank you so much*)

Contents

List of Tables

List of Figures

Chapter 1

Introduction

Coastal upwelling is a physical oceanic process whereby alongshore winds and ocean current, cause an upward displacement of water from the subsurface towards the upper layer of the ocean. Coastal upwelling leads to increased nutrient levels near the surface, thus promoting phytoplankton growth and marine biological productivity with positive implications for the fishery industry (Bakun 1975, Kämpf & Chapman 2016).

The south of Madagascar is renowned as a hot spot of marine biological production due to the presence of coastal upwelling (Bemiasa 2009). Several new biological species collected in the region were recently uncovered and recorded in global taxonomy accounts (Manghisi et al. 2015, Houart & Héros 2015, Boo et al. 2016). Records have also shown that the waters south of Madagascar have the highest numbers of fish stocks in the island (Pripp et al. 2014, Paubert et al. 2015, Breuil & Grima 2014).

Despite such productivity, historical records reveal that the south of Madagascar has experienced severe episodic famines due to cyclic low precipitation that result in drought conditions within the region (Randriamahefasoa 2013). The occurrence of the famine has been largely attributed to local and/or regional ocean-atmosphere oscillation cycles (Allison et al. 2009). The cyclic drought has had severe social and economic consequences on the livelihoods of local fishermen living in the southern Madagascar region (Allison et al. 2009, Le Manach et al. 2012). Cold upwelled water appears to decrease evaporation and moisture flux leading to less rainfall, in a process similar to that observed in the Somali coastal upwelling region, east of Africa (Sousa et al. 2016). Several climate factors are responsible for drought event south of Madagascar, but the air-sea interaction involving the upwelling is believed to be one precursor catalysing dry

weather conditions (Paubert et al. 2015).

A good knowledge of the ocean circulation and variability south of Madagascar is important for a better understanding of the regional and global circulation (Nauw et al. 2008, Srokosz et al. 2015). The oceans south of Madagascar are a major source of water for the Agulhas Current (de Ruijter et al. 2004, **?**). Oceanic variability south of Madagascar regulates the retroflection of the EMC and can drive changes in the Agulhas Current (Lutjeharms 1988, Quartly et al. 2006).

Therefore, coastal upwelling South of Madagascar is believed to have a direct and/or indirect impacts on the biology, meteorology and ocean circulation at both local and regional scales. Based on the above mentioned socio-economic and scientific aspects, there is a crucial need to understand the variability of the coastal upwelling south of Madagascar.

1.1 Motivations for the study

The present study seeks to improve our understanding of the variability and drivers of the coastal upwelling south of Madagascar.

Coastal upwelling is a physical process of ocean dynamics which causes the ascension of nutrient-rich water towards the surface, where they become available for phytoplankton growth (Barber & Smith 1981, Kämpf & Chapman 2016). Phytoplankton is a microscopic photosynthetic algae which is considered the first producer within the marine ecosystem. Phytoplankton is a primary food source for zooplankton, and together, both phytoplankton and zooplankton serve as food sources for higher-level predators in the marine food chain. Consequently, there is significant correlation between various coastal upwelling events and ocean productivity, as well as marine biomass (Demarq & Faure 2000, Figueiras et al. 2002, Chavez & Messié 2009, Hood et al. 2017). The high productivity of marine life observed in the region south of Madagascar is attributed to coastal upwelling.

The southern Madagascan region still remains one of the most under-developed parts of the country. The south of the island is marginalized in terms of its capacity to develop agriculture, farming and other relevant livelihood support activities. Marine resources therefore provide substantial support to maintain the coastal livelihoods of marginalized people. Coastal upwelling regions south of Madagascar have a strong social and economic value as they support

rural livelihood and the local fishery industry (Allison et al. 2009, Bemiasa 2009). The socio-economic value derived from coastal upwelling provides further motivation for the investigation of the spatial and temporal characteristics of the coastal upwelling south of Madagascar (Davies et al. 2009, Bemiasa 2009).

In a regional context, the variability of the ocean circulation south of Madagascar is a major source of variability for the Agulhas Current (Nauw et al. 2008, **?**). The East Madagascar Current (EMC), one of the main contributors to the Agulhas Current (**?**), carries an important part of the water circulating south of Madagascar (Lutjeharms et al. 2000, Ponsoni et al. 2016). The upwelled waters are among of those water masses (DiMarco et al. 2000, de Ruijter et al. 2004). At the southern extension of the EMC, dipole mesoscale eddies (cyclonic and anticylonic) form and propagate westward towards the Agulhas Current system (de Ruijter et al. 2004, Ridderinkhof et al. 2013). The upwelled waters could influence the generation of eddies, but occurrences and variabilities associated with upwelled water are still not well understood (Quartly et al. 2006, Ridderinkhof et al. 2013).

At the southern extension of the EMC, part of the flow incoming from the EMC veers eastward towards the Madagascar basin (Longhurst 2001). Literature also suggests that this eastward flow is thought to favour the formation of the phytoplankton bloom in the open ocean because it carries the water upwelled from the South Madagascar coastal regions (Longhurst 2001, **?**, Srokosz et al. 2015).

Based on this general context, upwelled water plays an important role in contributing to the ocean circulation in the region, and is a key component for marine productivity at the coast, as well as in the open ocean. Investigating the variability and drivers of the upwelling south of Madagascar should improve our knowledge on the marine production and the variability of the ocean circulation south of Madagascar.

1.2 Objectives, approaches and structure

This study provides a holistic understanding of coastal upwelling processes south of Madagascar by addressing the following questions:

1. **What is the spatial extent of the coastal upwelling and how does it change in time?**

Previous studies (DiMarco et al. 2000, Machu et al. 2002) have attempted to define the regional extent of the coastal upwelling regions but no study has ever investigated temporal changes and the spatial distribution of upwelled waters. In this thesis, satellite observations are used to clearly identify upwelling cells occurring along the southern Madagascan shores and to show how the geographical extent of upwelling cells changes over time.

2. **How does coastal upwelling south of Madagascar change seasonally?**
   While a few studies have investigated the temporal variability of the coastal upwelling south of Madagascar (Machu et al. 2002, Ho et al. 2004), none of them addressed the issue of seasonal variability. Upwelling indices derived from satellite observations of SST and winds are used to characterise the seasonality of the coastal upwelling south of Madagascar. The biological response to the upwelling variability is investigated using estimates of Chlorophyll-a concentration from satellite.

3. **What are the drivers of coastal upwelling ?**
   Based on previous work (DiMarco et al. 2000, Machu et al. 2002), the mechanisms promoting upwelling remain unclear. The multiple forcings generating the upwelling are clarified in the present study using multi-sensors satellite observations, in-situ data analyses, realistic model simulations and idealised model experiments.

4. **What is the link between the Mozambique channel water and the upwelling south of Madagascar?**
   The link between the Mozambique Channel water and the upwelling has never been explored before. Satellite observations, in-situ data, ocean model outputs and Lagrangian simulations are used to address this link.

5. **What regulates the inter-annual variability of upwelling cells?**
   Here we investigate how the upwelling intensity varies at inter-annual time-scales taking into account both local and remote forcing processes. Satellite observation, model output and climate mode oscillation indexes have been used to characterise long-term variations of the upwelling.

The thesis is organized as follows: Chapter 2 provides a literature review of coastal upwelling processes in both a regional and global context; Chapter 3 provides a detailed account of the data and methods used; Chapter 4 responds to the first three research questions related to the spatial

and seasonal variability of the south Madagascar coastal upwelling; Chapter 5 concentrates on drivers of the upwelling; Chapter 6 focuses on coastal upwelling inter-annual variability. Lastly, Chapter 7 concludes and summarises the main findings of this study.

Chapter 2

Literature review

This chapter provides a synopsis of key bodies of literature relevant to upwelling systems at the global scale, as well as within the regional context of Madagascar. The literature review seeks to highlight linkages between ocean currents, upwelling events and ocean productivity in the coastal regions south of Madagascar.

2.1 Upwelling south of Madagascar in a global context

Coastal upwelling is an upward motion of deep water occurring along the coast which is a result of atmospheric and/or oceanic forcing. As the water reaches the surface of the ocean, it is usually cold and rich in nutrients. Due to this oceanographic occurrence, upwelling tends to promote biological growth within different layers of the marine food chain, which promotes phytoplankton blooms.

Coastal upwellings are usually characterised by the following properties: colder surface water, high biological productivity, low sea level height and intense alongshore winds (Bakun 1975, Demarq & Faure 2000, Veitch 2009). These characteristics tend to be utilized in quantifying and distinguishing between different types of coastal upwelling.

A wind-driven upwelling is a coastal upwelling induced by an alongshore wind (Vazquez-Cuervo et al. 2013). This process is characterised by alongshore winds, generating an offshore Ekman transport, and reducing sea water levels as the surface water mass is displaced (Bakun 1975). Thereafter, surface water becomes colder than the surrounding water, and phytoplankton blooms are promoted.

Coastal upwelling can be also induced by ocean currents. The interaction of a current with the topography can generate an uplift of water from the deep ocean to the surface. This also results in cold water and high phytoplankton concentration at the surface layer (Schaeffer et al. 2013). Surface water signatures, based on temperature, chlorophyll concentration, sea level height and wind intensity, are used to identify the incidence of coastal upwelling.

Globally, various types of coastal upwelling have been categorized based on their locations, as well as based on the main forces driving the upwelling.
Figure 2.1 depicts the major coastal upwelling regions around the world (Kämpf & Chapman 2016). The upwelling ecosystems identified in the map are classified as wind-driven (including continuous and seasonal) and the "others", which are not primarily driven by winds.

The major upwelling regions are the Eastern Boundary Upwelling (EBU) regions along the shores of Peru, Chile, west Africa, Portugal and California. These upwelling systems are adjacent to regions characterised by the high pressure associated with wind gyre patterns and are continuously forced by alongshore winds (Chavez & Messié 2009, Kämpf & Chapman 2016). EBU regions are renowned for their biological productivities over large areas of the ocean along the coast.

Southeastern Australia, Brazil, eastern Africa and northern Arabian seas belong to the Western Boundary Upwelling (WBU) regions. These upwelling systems are also forced by seasonal winds and/or dynamically driven through the interaction between western boundary currents and the continental shelf topography. Western boundary currents contribute to coastal upwelling in many regions of the world, thus considerably enhancing global ocean productivity (Kämpf & Chapman 2016).

Among the upwelling regions listed above, the south Madagascar coastal upwelling system is one of the smallest in size, and could be classified according to any of the existing standard categories due to its location, which is in between the EMC and the Mozambique Channel. This particular upwelling system is included in the category "Other" (Figure 2.1), which means that the mechanism of the upwelling system is still not well documented.

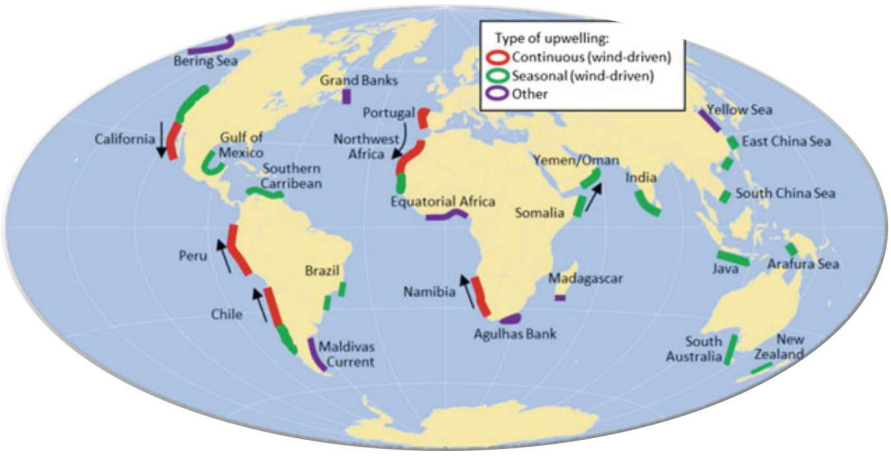

Figure 2.1: Location of the major upwelling regions categorized by forcing mechanisms, taken from Kämpf & Chapman (2016) (*see page 47*).

2.2 Regional context

The current section provides a review of the regional oceanographic process that could remotely or directly interact with the upwelling south of Madagascar.

2.2.1 South Equatorial Current (SEC) and Madagascar

The South Equatorial Current (SEC) flows east-to-west in the South Indian Ocean (SIO) between 10°S and 20°S. The South Equatorial Current is driven by the southeasterly trade winds (Nauw et al. 2008, Hood et al. 2017).

In the south-west Indian Ocean, the South Equatorial Current is known to bifurcate into two branches off the east coast of Madagascar. The northward branch becomes the North Madagascar Current (NMC) and the southward branch becomes the EMC (Lutjeharms 1976, Swallow et al. 1988). However, the precise position of the SEC bifurcation is still not clearly defined due to a lack of observational data in the upstream East of Madagascar Current region. In the past, the South Equatorial Current bifurcation off Madagascar was said to occur around 17°S at the surface (Swallow et al. 1988) and around 20°S around 800-900 m depth (Chapman et al. 2003). The southward shift of the South Equatorial Current bifurcation integrated in certain depth described by Chen et al. (2014) is consistent with the maps of steric height presented by Ridgway & Dunn (2007) (*in their Figure 2*) and can explain the apparent inconsistency between results, from previous works, and the position of the separation obtained at depth

suggested by Chapman et al. (2003).

In his book, Lutjeharms (2006) states that the South Equatorial Current separation along the Madagascar coastline occurs further north, at a latitude of about 15°S. More recently, Chen et al. (2014) report a South Equatorial Current bifurcation latitude shifting from 17.5°S at the surface to 19°S at 400 m depth. Chen et al. (2014) also show a discrepancy in the location of the South Equatorial Current bifurcation of 1.2° between the mean circulation depicted from the World Ocean Database 2009 data sets and that derived using 19-years of altimetry. The estimation-based on altimetry positioned the South Equatorial Current bifurcation at 16.9°S. The impact that variations in the South Equatorial Current bifurcation have on the EMC and on the coastal upwelling regions south of Madagascar remains unknown.

2.2.2 East Madagascar Current (EMC)

The South Equatorial Current bifurcates in two directions after hitting the east coast of Madagascar. The poleward branch, which flows alongshore until the southern tip, is the EMC (Swallow et al. 1988). The EMC is a poleward warm western boundary current. The estimated mean volume transport is 18.3 Sv (Ponsoni et al. 2016). The EMC is regulated by the common characteristics of western boundary currents described by Stommel (1948), who explained that they are driven by zonal integrated wind-stress curl over the width of the subtropical region.

Historically, the EMC was documented for the first time by Lutjeharms et al. (1981). In that study, drifter trajectories and Expendable Bathythermograph (XBT) sections were combined to characterize the EMC behaviour. Lutjeharms et al. (1981) estimate an EMC volume transport of 41 Sv based on in-situ observations. Lutjeharms (1988) introduces evidence of the EMC as a miniature western boundary current, which contributes to Agulhas Current, by using an infrared remote sensing approach. He also questions the consistency of the EMC retroflections. In the vicinity of 25°S, the EMC was noticed to retroflect toward the Indian Ocean during an investigation study undertaken by Quartly et al. (2006). They used Sea Surface Height (SSH) signals from altimetry and outputs from a numerical model, OCCAM, to characterise the EMC retroflection.

Two recent consecutive works from Ponsoni et al. (2015, 2016) have shed a new light on the dynamics of the EMC. Ponsoni et al. (2015) investigated long-term observation of the EMC using combination of Acoustic Doppler Current Profiler (ADCP) and Rotor Current Meter (RMC) mooring array measurements placed at the east coast of Madagascar during 2.5 years of

record. Ponsoni et al. (2015) found the presence of the East Madagascar Undercurrent (EMUC) whose core is located at 1260 m depth and at 26 km offshore. They noted that the EMUC has a bi-monthly and semi-annual periodicity.

Ponsoni et al. (2016) combined the long-term observation of ADCP data sets, used in Ponsoni et al. (2015), with satellite observation to derive volume transport and characterise the inter-annual variability of the EMC. Their findings showed that the mean volume transport of the EMC is 18.3 Sv and maximum can reach 50 Sv. They also showed that part of the EMC variability is influenced by the arrival of westward-propagating mesoscale eddies (cyclonic and anticyclonic) from the Indian ocean.

Lutjeharms & Machu (2000), DiMarco et al. (2000) and Ho et al. (2004) suggest that the EMC is an important component that influences the coastal upwelling south of Madagascar. Reviews related with the interaction of EMC and the upwelling will be more developed in Section 2.3.

2.2.2.1 EMC retroflexion concept

Introduced by Lutjeharms et al. (1981), the East Madagascar Current (EMC) is portrayed as having a western boundary current characteristics and perceived to retroflect, based on series of Expendable Bathythermograph (XBT) measurements during oceanographic cruise at the east coast of Madagascar used in the study.

Later on, Lutjeharms (1988) had confirmed that the EMC does indeed retroflect. He demonstrated the EMC retroflexion by using SST satellite imagery.

The concept of the EMC retroflexion was re-considered by Quartly et al. (2006). Using a various type of satellite data sets and OCCAM numerical model, the ocean colour and infra-red imagery proved the evidence of an EMC Retroflexion. The sequences of satellite images were consistent with the model output which also revealed that the intermittency of anticyclonic eddies moving westward may explain the source of retroflexion features of the EMC.

Using the similar approaches in Quartly et al. (2006), Siedler et al. (2009) mentioned that the southern branch of the East Madagascar Current (SEMC) separates in two directions at the south of Madagascar. The first branch flows toward the Agulhas Current system, while the second branch retroflects toward the Subtropical Indian Ocean Countercurrent (SICC). They used data sets from satellite observations and a nested high resolution model to demonstrate the evidence of the EMC retroflexion. They found a good agreement of this separation between

the patterns of SEMC shown in observational data and in the nested model. However, there is no literature which mentioned the seasonal or inter-annual occurrence of the EMC retroflexion, except de Ruijter et al. (2004) who pointed out the possible link between the upwelled water variability and the occurrence of the EMC retroflexion during investigation of pathways and generation of the cyclonic eddies study at the south-east of Madagascar.

2.2.3 Dipole of mesoscale eddies at the south of Madagascar

After the separation of the EMC at the south-east coast of Madagascar, dipoles of mesoscale eddies, cyclonic and anticyclonic, are formed at the south of the island and propagate toward the African coast. The cyclonic eddies originate mostly from the southern tip of the Madagascan coast, while the anti-cyclonic eddies generally form further in the region south-west of the island (de Ruijter et al. 2004, Siedler et al. 2009, Ridderinkhof et al. 2013). Halo et al. (2014) revealed that the seasonal eddy formation is influenced by the variability of the SEMC flux which is the southern extension of EMC. Halo et al. (2014) also provide important information on the hydrographic properties of the cyclonic eddies, which have different characteristics depending on the location of their formation, between south-west and south-east. The occurence of mesoscale eddy dipoles south of Madagascar exhibits an inter-annual variability. This inter-annual variability is influenced by the El Niño-Southern Oscillation (ENSO) (Ridderinkhof et al. 2013). The variability of eddies contributes significantly to the large-scale circulation (Halo et al. 2014), such as to the variability of the retroflection of the Agulhas Current (AC) (Ridderinkhof et al. 2013).

2.2.4 Phytoplankton bloom south-east of Madagascar

Away from the coast, the phytoplankton bloom south of Madagascar is a large and irregular occurrence of phytoplankton growth in the Madagascar basin. It is one of the largest open-ocean chlorophyll bloom, equivalent to one percent of the global ocean surface (**?**). Still much remains uncertain about the drivers and the variability of this open-ocean phytoplankton bloom. However, the coastal upwelling south of Madagascar is suggested as a hypothesis enabling the bloom (**?**). Longhurst (2001) was the first to investigate the incidence of the bloom. Longhurst (2001) found that the bloom was intense at the beginning of each year, except in 1998. Thereafter, Uz (2007) revisited the south-east Indian Ocean bloom described by Longhurst (2001). Compared to other works which described the bloom, Uz (2007) distinctly mentioned that the bloom is

not caused by the enrichment coming from the bottom of the ocean. He also could not find a plausible correlation between the intensity of the bloom with any physical parameters. An alternative hypothesis by Uz (2007) suggests periodical cyclonic activity, causing a landfall rich in mineral, transporting iron from island towards the South Indian Ocean Countercurrent (SICC), which coincide with the incidence of bloom. Uz (2007) also did not mention if the upwelling could impact fertilization processes. Additional information about the bloom of phytoplankton will be provided in the next subsection to highlight the importance of the upwelled water for the regional circulation.

2.3 Coastal upwelling south of Madagascar

Figure 2.2 provides a historical review of upwelling events, based on published works which have mentioned the "upwelling South of Madagascar". The timeline shows the number and the evolution of past published work.

The 5 publications in blue in Figure 2.2 were the first to provide insights into the physical drivers of the coastal upwelling south of Madagascar and of its variability. The two publications shown in the green colour linked the biological productivity to the upwelling system, based on fisheries surveys. The remaining publications address the broader implications of the upwelling at local and regional scales.

The timeline will be used as a frame for the literature survey by categorising those published works in each domain enumerated above.

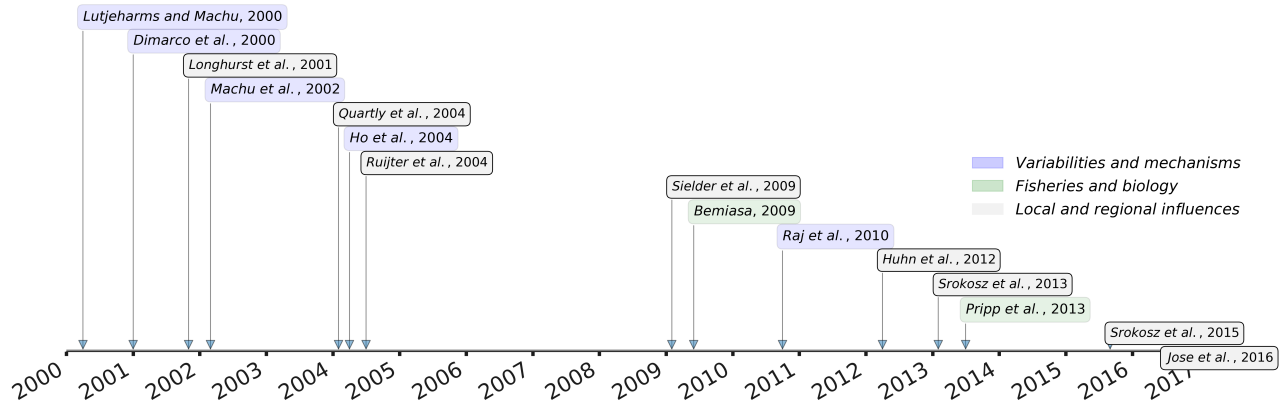

Figure 2.2: Timeline summarising existing work on the upwelling south of Madagascar. The blue colour distinguishes works which primarily emphasize the upwelling south of Madagascar, its variability and mechanisms. The green colour depicts some works which focuses on upwelling and fisheries coupling. The grey colour represents works which mentions the contribution of the Madagascan coastal upwelling to the regional circulation.

2.3.1 What forces the coastal upwelling South of Madagascar and its variability ?

The literature (Lutjeharms & Machu 2000, DiMarco et al. 2000) on the history of upwelling south of Madagascar is relatively recent and limited. The earliest research on the topic was only conducted in 2000. Moreover, in the past two decades, several advanced observation systems had just arrived in ocean sciences. The study of the upwelling became possible due to the improved resolution of satellite remote sensing (wind, SST, chlorophyll, sea level), the development of ocean models, and initiatives to explore the Indian Ocean through oceanographic expeditions. Therefore, the ability of scientists to observe the region south of Madagascar has significantly increased over the last two decades with both improved and more frequent satellite observations.

Based on the timeline, the following section chronologically presents studies (coloured in blue on Figure 2.2) that described the coastal upwelling and its associated mechanisms.

Lutjeharms & Machu (2000) were among the first to investigate coastal upwelling South of Madagascar and revealed the presence of an upwelling cell inshore of the EMC. The paper exploited Sea Surface Temperature (SST) and Ocean Colour satellite observations to characterize the surface water signature associated with the upwelling, such as colder water and increased chlorophyll concentration. Lutjeharms & Machu (2000) found that the implied upwelling cell is more apparent in Ocean Colour than in the SST. Coastal upwelling inshore of the EMC seems to be prevalent under all wind conditions. Lutjeharms & Machu (2000) also suggested that the

upwelling cell is probably not wind-driven and that an intense upwelling is linked to a strong western boundary current, the EMC, over the abrupt topography irregularities. However, samples of satellite observations were not consistent enough to derive significant conclusions about drivers of the upwelling system.

Later in that year, DiMarco et al. (2000) used two years of SST imagery (July 1998 through April 2000) to study the coastal upwelling south of Madagascar. They showed a sequence of upwelling incidences marked by cold water on the coast. DiMarco et al. (2000) reported that the cooler temperature appears to be important in mid-February with the strength of alongshore wind-stress and it reduces in mid March. They also noted that upwelling was present during the period of 1999, but with a much smaller temperature change. DiMarco et al. (2000) concluded that the coastal upwelling was caused by a combination of upwelling-favorable wind-stress and frictional interaction between a western boundary current (EMC) and the adjacent continental shelf. They also highlighted limitations due to the lack of wind-stress data to examine the relative strength between those two forcing mechanisms.

A hydrographic investigation was undertaken for the first time in the upwelling region, south-east of Madagascar, during the Agulhas Current Sources EXperiment (ACSEX-2) oceanographic cruise (Machu et al. 2002). Machu et al. (2002) revealed important results from this hydrographic campaign. Through several hydrographic sections in the upwelling region, they showed uplifted isotherms toward the surface: an indication that upwelling is occuring. In the same locations, Chlorophyll-a concentrations, from in-situ measurements, are also higher. Adding to the hydrographical investigation, remote sensing monitoring was simultaneously undertaken. Machu et al. (2002) confirmed the presence of a high Chlorophyll concentration observed in the satellite ocean colour product. From the combination of satellite imagery and in-situ observation, Machu et al. (2002) came up with a hypothesis that the change in the bathymetry and the steep slope at the south-east of Madagascar seems to favour the generation of a cyclonic eddy between the coast and the EMC core. Wind Ekman transport due to the wind stress mentioned by DiMarco et al. (2000) may interact with the cyclonic eddy to enhance the intensity of the upwelling.

Ho et al. (2004) brought a new understanding on the variability of the upwelling south of Madagascar and the role of the EMC in driving this upwelling. Ho et al. (2004) investigated the spatial and temporal variability of the upwelling using monthly SeaWiFS images during the period of September 1997 to November 2001. Ho et al. (2004) used an Empirical Orthogonal

Function (EOF) analysis to show that the upwelling is more intense in austral winter of each year except 1999 and in austral summer of each year except 2001. They were also the first who pointed out that the mechanisms generating upwelling may be difficult to define because of the multiple forcing interactions inducing upwelling which are still not well understood. Ho et al. (2004) thus suggested that the position and variability of the EMC interacted significantly with the incidence of the upwelling. They suggested that the mechanism of the interaction can be explained by a "shear wave propagation" theory.

Raj et al. (2010) characterized the intra-annual and inter-annual variability of Chlorophyll-a concentration in the South-western Indian Ocean and attempted to explain the causes of these variabilities.

During this work, Raj et al. (2010) included the upwelling south of Madagascar to be one of the sources which promoted high Chlorophyll-a concentration in the South-western Indian Ocean. Raj et al. (2010) revealed the evidence of coastal upwelling through the analysis of WOCE XBT sections collected in 1994 and 1995. The XBT vertical sections of temperature in the upper 800 m showed an uplift of the isotherm near 45°E. Results showed that the upwelling was pronounced during March 1995. They also found that the Mixed Layer Depth (MLD) inside the upwelling region exhibited a seasonal cycle which was shallower during the austral summer and deeper in austral winter based on a profile-based MLD climatology (de Boyer Montégut et al. 2004). Raj et al. (2010) highlighted that the changes in the upwelling along the south of Madagascar shores influenced the phytoplankton bloom in the South West Indian Ocean on the intra-annual and inter-annual time-scales. Raj et al. (2010) concluded that the major source of the nutrient-rich water generating the bloom originated from the upwelled coastal waters.

While upwelling was not the main focus of Raj et al. (2010) work, their study provided significant insights into the seasonal and inter-annual variability of chlorophyll concentration and MLD in the upwelling region.

Works cited above were not able to fully describe the variability of the coastal upwelling due to the scarcity of dataset available and high cloud contamination in the region, reducing coverage by satellite observations. Wind dataset used could not represent well dominant winds in the region and in-situ datasets were limited. No clear explanation was provided for the impact of the EMC on the upwelling. The alongshore wind is also not defined clearly as the main driver. On top of that, the pattern of upwelling variability seems to evoke the presence of a different spatial pattern for the upwelling cell.

2.3.2 Biological response to upwelling event

The two publications coloured in green shown in the timeline (Figure 2.2) investigated the link between the upwelling and fishery productions.

Bemiasa (2009) and Pripp et al. (2014) confirmed the high biological productivity south of Madagascar. Both suggest that biological richness in the region is due to the upwelling. Bemiasa (2009) undertook a study to understand the variability of anchovy, sardines and octopus production south-west of Madagascar and relate it to environmental parameters such as SST and Chlorophyll concentration. The study applied a statistical model based on Effort Per Units (EPU) of artisanal and industrial catches to estimate the species stock. Bemiasa (2009) also discussed the seasonal variability of the biological productivity, based on the catches surveys, which can be explained by the influence of the fertilization generated by the upwelling at the south of the island. The result revealed that the production peak of anchovy, sardines and octopus occurred during the upwelling favorable season. Bemiasa (2009) has also evoked a connexion between the upwelling cell and the south west coast of Madagascar. Bemiasa (2009) argued that enrichment found south west of Madagascar can be attributed to the upwelling at the southern tip.

Estimates of biomass from acoustics fishing survey instrument and trawl catches during a survey in September 2009 along the west coast of Madagascar showed high fish biomass (Pripp et al. 2014). The total acoustic survey for Clupeoids, Carangids and associated pelagic species on the southern shelf was approximately 16 000 tonnes of the pelagic fishes representing 90 % of the total. Pelagic and demersal trawl catches throughout the survey confirmed the estimates derived from the acoustics survey result. Based on the total catches during the survey, highest catches were observed at the southern tip. The pelagic average catch for the southern region was about 980 kg/hour. The highest catches of bottom trawl were obtained on the continental shelf where the mean of catch per unit reached 397 kg/hour. The number of catches highlighted by Pripp et al. (2014) demonstrated the evidence of high biological productivity associated with the upwelling zone.

2.3.3 Linkages between coastal upwelling and regional ocean circulation

The current subsection provides a holistic understanding of physical and biological impacts of the upwelling on the regional ocean circulation, based on works coloured in grey in the timeline.

The formation of the phytoplankton bloom in the Madagascar basin was suggested to be linked with the upwelled water south of Madagascar. We note that several works have investigated of the phytoplankton bloom characteristics but we focus on the possible link between the upwelled water variability and the bloom occurrences.

Longhurst (2001) was among the first to mention a possible link between upwelling system and the bloom of chlorophyll in the Madagascar basin. Longhurst (2001) explained that the EMC could generate a mesoscale anticyclonic eddy by flowing inshore. This eddy is a precursor of the EMC flow retroflection described that induces upwelled water displacement toward the Madagascar basin. Siedler et al. (2009) reinforced the hypothesis about the connection between the EMC and the Indian Ocean. They mentioned that approximately 50 % of the EMC volume transport contributed to the Agulhas current, while 40 % retroflected toward the Indian Ocean during an investigation of the South East of Madagascar Current (SEMC) retroflection characteristics. During the same study, Siedler et al. (2009) used satellite ocean colour images to illustrate the south-westward and south-eastward propagation of high chlorophyll concentration pattern due to the presence of the upwelling.

In a particle tracer experiment, Huhn et al. (2012) also showed that particles moved eastward from the southern tip of Madagascar toward the Madagascar basin.

Consecutive works by **?**Srokosz et al. (2015), which are focused on the variability and mechanism of the phytoplankton bloom, pointed out the contribution of upwelled water to promote the phytoplankton bloom occurring at the south-east of Madagascar. **?** found that the combined contribution of deep chlorophyll ascension induced by mesoscale eddies and upwelled water could be the mechanism promoting the phytoplankton bloom. They also confirmed that the inter-annual variability of the bloom is linked with the inter-annual variations in the coastal upwelling as the main iron supplier.

From the numerical experiment, Srokosz et al. (2015) validated the hypothesis that the flourishing bloom was due to iron advection from Madagascar sediment, transported by mesoscale

eddies to the south-east. However, they admitted that it was difficult to isolate quantitatively iron from sediment at the coast and from river run-off from more inland.

Results in these works supported the information that upwelled water at the south of Madagascar could be the source of the nutrient-rich water propagating toward the South Indian Ocean promoting the open-ocean phytoplankton blooms in the Madagascar bassin, as reported by Longhurst (2001) and Quartly & Srokosz (2004*a*).

The generation of mesoscale eddies (cyclonic and anticylonic) south of Madagascar has been suggested to be linked with the upwelled water south of Madagascar.
Quartly & Srokosz (2004*a*) investigated mesoscale variability south-east of the Mozambique Channel. They used SeaWiFS chlorophyll concentration to observe the patterns of the eddies. Quartly & Srokosz (2004*a*) argued that cyclonic eddies south-east of Mozambique occurred intermittently, appeared to pre-form in the lee of the southern tip of Madagascar, and induced high-productivity coastal waters. The formed cyclonic eddy propagated westward toward the African coast. Indeed, upwelling south of Madagascar should play a role for the formation of cyclonic eddies. However, Quartly & Srokosz (2004*a*) also recognized that it is difficult to identify the chlorophyll signature propagations from upwelling or/and cyclonic eddies during a change in the wind and the EMC, and that further work on this topic is required.
de Ruijter et al. (2004) combined observations from satellite altimetry and in-situ hydrographic and ADCP measurements collected during the ACSEX cruise to characterize the mesoscale eddy field south of Madagascar. Findings revealed that the formation of dipoles south of Madagascar could be attributed to the separation of the EMC from the continental shelf at the southern tip of Madagascar. The dipoles are generated at irregular intervals and then they propagate westward toward the African coastline. de Ruijter et al. (2004) found that cyclonic eddies formed at the inshore edge of the EMC while anticyclonic eddies seemed to form before cyclonic eddies and originate directly from the EMC flow. Irregularities and inter-annual variability were influenced by the SEC bifurcation, the strength of the EMC and the links with large-scale climate variability (El-Niño Southern Oscillation/Indian Ocean Dipole cycles). Interestingly, this work revealed that cyclonic eddies were formed along the continental slope where upwelling cell occurs. de Ruijter et al. (2004) raised the assumption that increase in cyclonic eddies vorticity coincided with an intense upwelling event such as in February/March 2000 mentioned by DiMarco et al. (2000).

Jose et al. (2016) removed the non-linear term of momentum advection in the Navier-Stocks equation, in a coupled physical-biogeochemical simulation. The objective of the study was to understand the inertial processes on the dynamic of mesoscale eddies upon the biological production in the Mozambique channel. One of their findings mentioned that the decrease of chlorophyll concentration south-west of Madagascar may be due to the dissipation of chlorophyll exerted by the mesoscale eddies. Another main finding of this paper mentioned that the momentum advection of the current provoked the detachment of the EMC along the coast. This information is very important to understand the characteristics of the EMC and its influence on the chlorophyll concentration at south of Madagascar. As mentioned by Lutjeharms & Machu (2000), DiMarco et al. (2000), Ho et al. (2004), advection of the EMC is highly associated with the coastal upwelling incidence. Related to that, the EMC detachment along the coast should be the precursor of the chlorophyll concentration to the south of Madagascar through the upwelling and the south-east Madagascar phytoplankton bloom explained above.

Works described above mentioned the important links between mesoscale eddies dipole formation and coastal upwelling south of Madagascar as well as connections between the coastal upwelling regions and the development of open-ocean phytoplankton blooms in the Madagascar basin. These works suggested the importance of investigating the variability of the upwelling which can influence the variability of general circulation in the region.

2.3.4 Linkage between south of Madagascar waters and the large-scale Indian Ocean variability

The Indian Ocean is affected by important climatic variations (Wilkinson et al. 1999, Hoerling et al. 2004). Inter-annual variability of Indian Ocean is thought to be dominated by the Indian Ocean Dipole (IOD) (Marchant et al. 2007) and by the El-Niño Southern Oscillation (ENSO) variability mode (Ashok et al. 2001, Ashok, Guan, Saji & Yamagata 2004, Kug et al. 2006), which may occur in conjunction with or independently from Indian Ocean Dipole variability. Both Indian Ocean Dipole and El-Niño Southern Oscillation do not fully explain all the inter-annual variabilities influencing the Indian Ocean climate (Reason & Mulenga 1999, Behera & Yamagata 2001). Behera & Yamagata (2001) and Morioka et al. (2013) suggested the presence of a tropical dipole event discovered recently in the Indian Ocean, which also influences strongly the tropical level of the Indian Ocean: the Subtropical Indian Ocean Dipole (SIOD). Subtropical

Indian Ocean Dipole is the occurrence of SST anomaly in two regions of positive and negative SST anomalies around the tropics. Positive phases of Subtropical Indian Ocean Dipole tend to have cold SST anomalies off Australia region and warm SST anomalies south of Madagascar region, and vice-versa for the opposite phase (Behera & Yamagata 2001).
These climate oscillations are associated with strong air-sea interactions and drive change in wind regimes, precipitation rate and ocean dynamics in the Indian Ocean (Kumar et al. 1999, Reason & Mulenga 1999, Saji et al. 1999, Pfeiffer & Dullo 2006). The air-sea interaction driven variability in the Indian Ocean may impact on the inter-annual variability of the south-west Indian Ocean circulation (De Ruijter et al. 2005, Palastanga et al. 2006, 2007) where the coastal upwelling south of Madagascar is located.

Limited works have investigated the impact of the climate oscillation influencing the coastal upwelling. Little is known about the tele-connection between the large scale Indian Ocean circulation and south of Madagascar at inter-annually time scale. Characterising the inter-annual variability of the ocean circulation and the dominant winds at the south of Madagascar, including their respective forcings, should explain the inter-annual variability of the coastal upwelling.

2.4 Similar coastal upwelling in other regions

Few upwelling systems are comparable to the south Madagascar upwelling system. Several upwelling systems share common characteristics, but the upwelling east of Australia is the one that best resemble the upwelling south of Madagascar.

The upwelling off the east of Australia appears to be primarily driven by the interaction between the East Australian Current (EAC) and the continental shelf (Schaeffer et al. 2013). Roughan & Middleton (2002) identified four origins of nutrient enrichment mechanism of east Australian upwelling system. Roughan & Middleton (2002) explained that the first three main drivers of the nutrient supply system are highly related with the East Australian Current advection. They demonstrated that the highest nutrient concentration is attributed to the "encroachment" for the East Australlian Current onto the shelf. The widespread nutrient distribution is driven by the detachment of East Australian Current from the coast. And a simple increase of East Australlian Current advection also generates nutrient enrichment by itself. The wind-driven upwelling also contributes significantly to the east Australian upwelling

system. Roughan & Middleton (2002) also raised an interesting interaction and combination between these various mechanisms. They observed that the effect of topographically induced upwelling is combined with the encroachment East Australian Current early in summer. Additionally, the EAC separation from the coast allows a pre-conditioning effect to surface water layers for a favourable wind-driven upwelling.

The coastal upwelling south of Madagascar seems to be induced predominantly by the EMC. This is comparable to the topographically-induced upwelling observed for the east Australian upwelling. This does not exclude the role of a wind-driven upwelling. The wind can play a role as a conditioner to favour the effect of the current in driving the upwelling.

Chapter 3

Data, Models and Lagrangian simulation

3.1 Satellite products description

A range of selected satellite products from various sensors and platforms are selected for this study. Comparisons between products are conducted to assess the satellite data set's reliability and limitations in the identification of upwelling occurrences.

3.1.1 Satellite Surface Temperature

Satellite observations of Sea Surface Temperature (SST) are most widely used to identify the cold surface water signature associated with upwelling events (Benazzouz et al. 2014). In this study, several SST products are used to characterise the spatial, seasonal and inter-annual variability of the coastal upwelling.

The Moderate-Resolution Imaging Spectroradiometer (MODIS) level 2b SST is downloaded from the NASA Ocean Color Nasa website and processed by the Marine Remote Sensing Unit (MSRU, Cape Town, South Africa). Monthly composites of SST are derived from the 1 km gridded L3 Aqua and TERRA MODIS daily maps. SST monthly averages are calculated by taking into account the number of daily valid observations to construct each monthly composite. Figure 3.1 summarises that MODIS TERRA satellite observation provide enough valid pixels within the upwelling zone to be able to construct the SST seasonal cycle. Valid pixels recorded

in the upwelling region are above 60 % for all months except for December and January which are less than 30 %. This is due to the high evaporation occurring above the warm surface current, East Madagascar Current (EMC), which generated massive atmospheric cloud cover inhibiting satellite measurements.

MODIS SST is chosen because the infrared observations from the MODIS sensor demonstrated a high level accuracy (Emery et al. 2001) and have been used in other upwelling investigation (Dufois & Rouault 2012), however, are highly limited by atmospheric contamination (Guan & Kawamura 2004).

To improve the coverage limited in MODIS SST, the Multi-Scale Ultra-High Resolution (MUR) SST is also used in this study. The MUR SST is a gridded, blended, and gap-free dataset developed by NASA-JPL. It is produced by merging data from MODIS, AMSR-E, WINDSAT, and AVHRR SST products on a 0.011° grid. It combines the capacity of high-resolution infrared waveband (1 km resolution) and the signal-crossing of the atmosphere by microwaves waveband (25 km resolution) which are not impeded by clouds. MUR SST is validated with surface observations which came from ship and buoy measurements (Vazquez-Cuervo et al. 2013).

MUR SST data is provided with its "SST Error" generated during the merging processes. Errors are produced from each data product before and after the merging. The error before the merging is due to the incomplete coverage primarily caused by clouds for infrared product and errors obtained from successive geographical corrections caused by the swaths and orbits gaps. The error after the merging is generated during the calculation of mean values in producing the gap-free SST fields (Vazquez-Cuervo et al. 2013, Liu & Minnett 2016).

The more the value of the errors tends to become small, the reliability will be higher.

Figure 3.2 provides an annual cycle of the SST errors calculated in the upwelling zone. Figure 3.2 shows that less of 0.36°C of SST error occurred in the upwelling zone while the EMC SST error attained 0.39 °C during summer.

Vazquez-Cuervo et al. (2013) reveal that the MUR SST product is well suited to the study of coastal upwelling processes. Adding to that, Gentemann et al. (2017) reveals the accuracy of MUR SST in representing the anomaly of a marine heat wave occurring along northeast Pacific coastal zone during the 2015 El Niño event. This confirms the ability of MUR SST to capture variability near the coastal zone explained in that study.

Figure 3.3 is a scatter plot of pairs of independent variables, MUR SST and the MODIS

level 2b SST, which reveals the level of linear relationship between the data sets.
A comparison between the MUR SST and the MODIS level 2b SST reveals that both mean SST inside the upwelling region during period of 2003 to 2015 are strongly correlated with a correlation factor of 0.992 significant at the 0.95 level (Figure 3.3). Figure 3.3 also shows that SST datasets have similar medians and similar Probability Density Functions (PDF).

In order to describe inter-annual variability of SST in the upwelling zone, the multi-channel Advanced Very High Resolution Radiometer (AVHRR) SST Pathfinder SST version PFV5.0 dataset (https://podaac.jpl.nasa.gov/AVHRR-Pathfinder), covering the period from 1981 to 2009 on a 4 km resolution grid is used. The Pathfinder SST data set is also compared with the MUR SST (Appendix A.1), where agreement between products is demonstrated by a strong linear relationship in the order of 0.995 for a significant correlation factor at 0.95 level (Figure 3.4). Similar comparison applied to above SSTs, Figure 3.4 also illustrates that MUR SST and SST Pathfinder have similar value of medians and similar Probability Density Functions (PDF).

The SST product comparisons are the primary process for generating a long time series from MUR SST and extended by Pathfinder SST dataset to obtain a 36-years series of SST data during the period from 1982 to 2017.

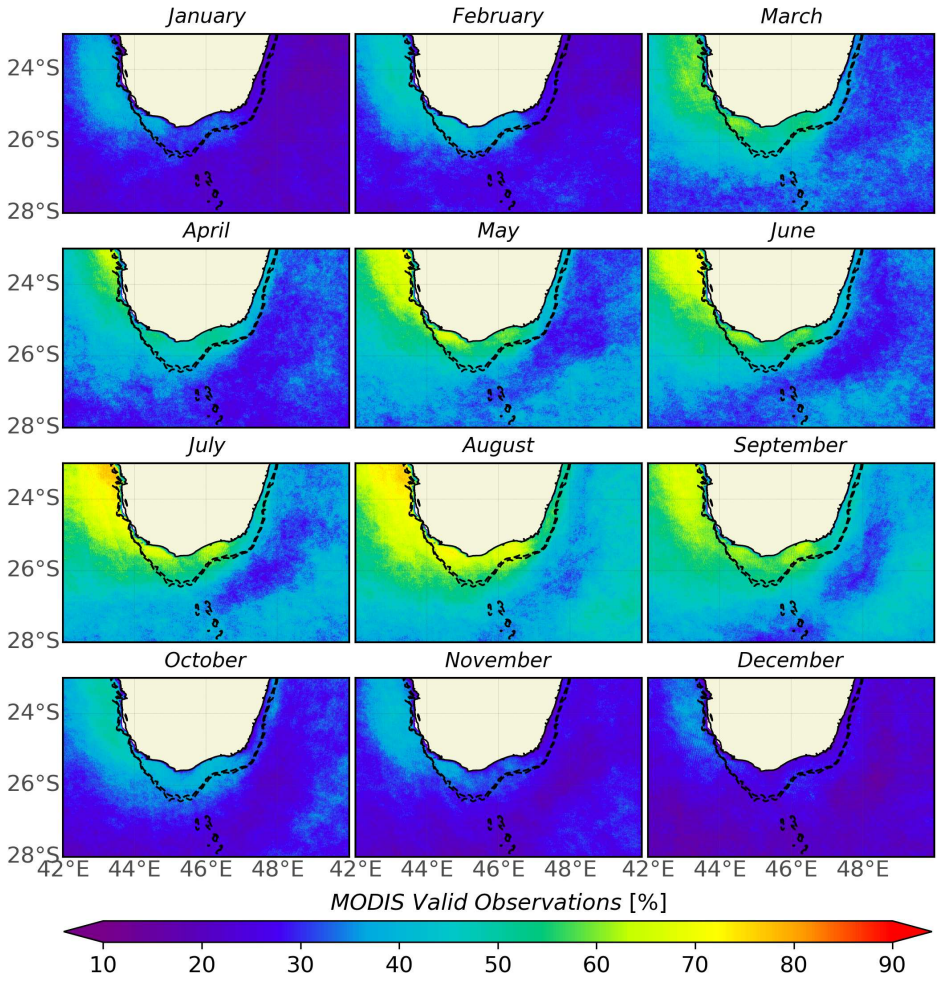

Figure 3.1: Annual cycle of valid data recorded from MODIS TERRA satellite observation, in percent, during the period 2003 to 2015. Black dotted lines are isobath 500 and 1000 m.

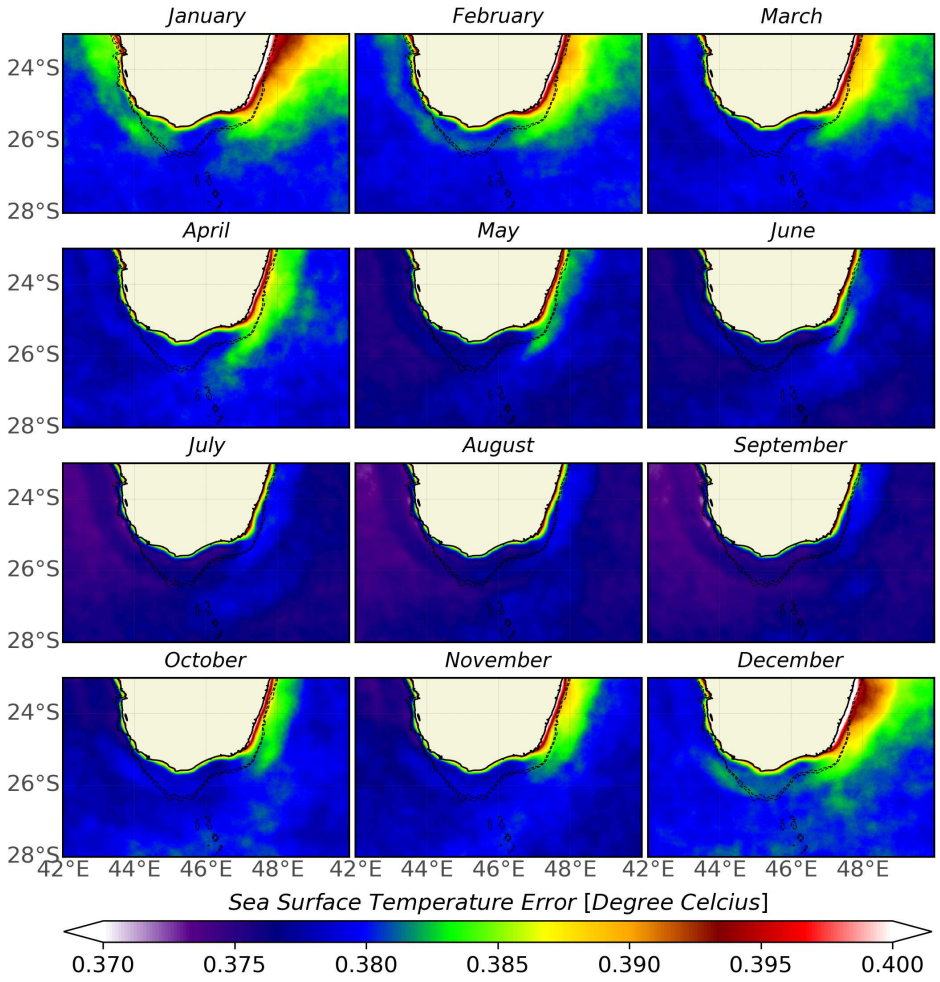

Figure 3.2: Annual cycle of SST error from MUR SST product, during the period 2003 to 2015. Black dotted lines are isobath 500 and 1000 m.

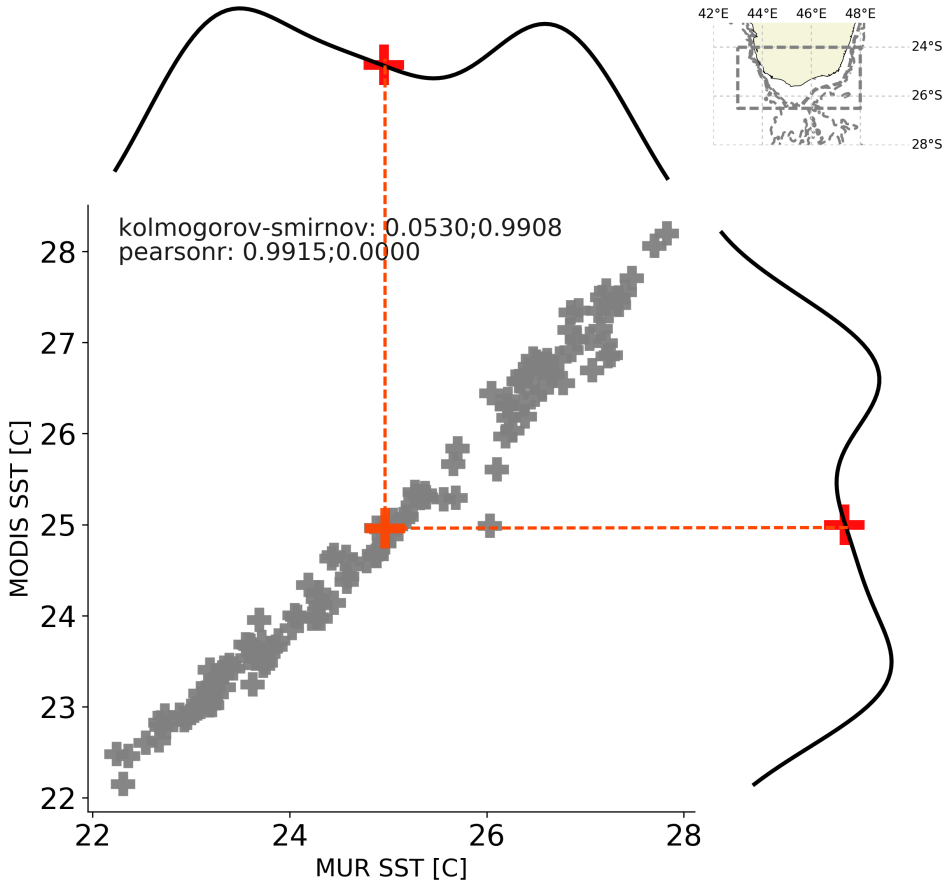

Figure 3.3: Scatter plot illustrating the linear agreement between time series from Infrared radiometry SST product (MODIS Terra) and Merge blended SST product (MUR) retrieved from the upwelling south of Madagascar zone over the period 2003 to 2015. Plots in each lateral sides are the re-projected Probability Density Function (PDF) from each time series. Red crosses positioned the value of medians (first percentile) in each data distribution. Linear coefficient correlation (Pearson) qualifies the linear relationship between data distributions. Kolmogorov-Smirnov coefficient represents distance between the two Probability Density Functions. Strong coefficients represent that data repartitions follow similar Probability Density Function.

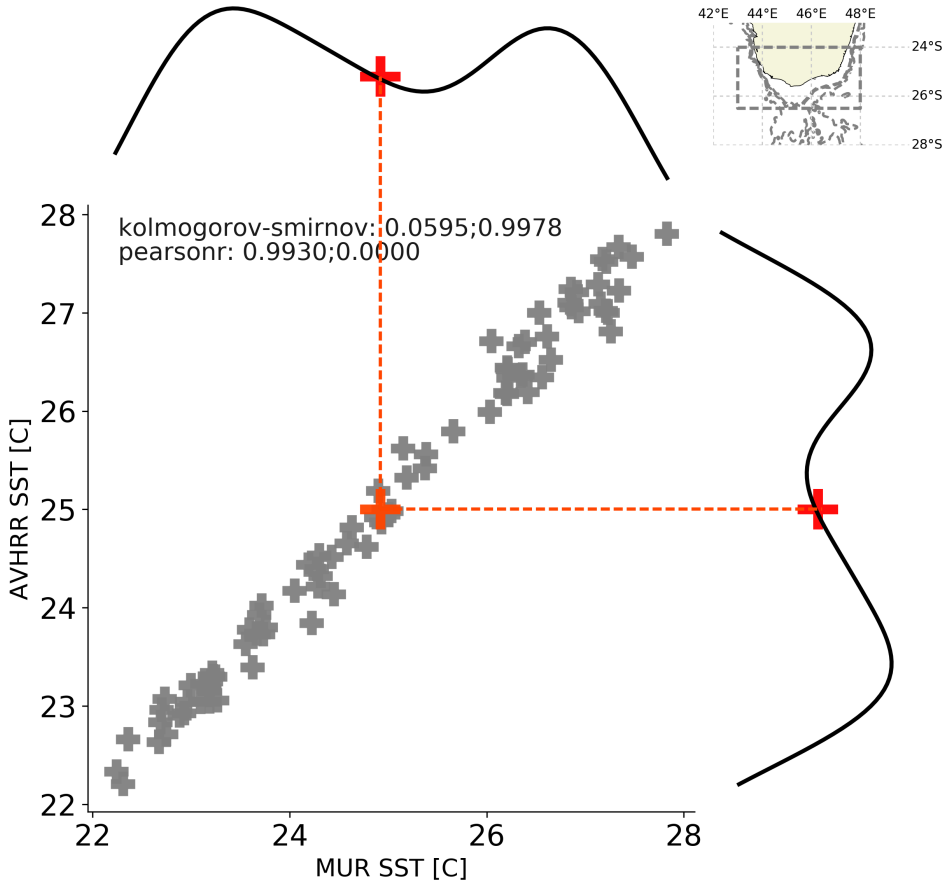

Figure 3.4: Scatter plot illustrating the linear agreement between time series from Merge blended SST product (MUR) and AVHRR SST product retrieved from the upwelling south of Madagascar zone during the period 2003 to 2013. Plots in each lateral sides are the re-projected Probability Density Function (PDF) from each time series. Red crosses positioned the value of medians (first percentile) in each data distribution. Linear coefficient correlation (Pearson) qualifies the linear relationship between data distributions. Kolmogorov-Smirnov coefficient represents distance between the two Probability Density Functions. Strong coefficients represent that data repartitions follow similar Probability Density Function.

3.1.2 Ocean winds

The measurement of ocean wind is measured from space from the wind-roughness of sea surface resulting from the interaction of the atmospheric motion relative to the surface of the ocean (Wentz 1992). Satellites transmit the backscattered power received from the sea surface roughness signature to calculate the surface wind using microwave radiometry (Shirtliffe 1999). The common reference height for near-surface ocean wind measurements is situated at ten meter of sea surface (Large & Pond 1981).
Ocean winds have been widely used to measure wind-driven upwelling intensity (Bakun 1975). Accuracy in observations of both wind speed and direction are necessary to derive accurate upwelling intensity induced by the wind (Bakun 1975, Large & Pond 1981). Selecting sea surface product wind is an important step before characterising a wind-driven upwelling.

Direction of the wind needs adequately to be parallel with the coastline structure to promote upwelling (Benazzouz et al. 2014). For that, products which sufficiently represent intensity and direction of the wind on the coastal zone are required to represent the wind-driven upwelling. At the South of Madagascar, the coastal topography structure is characterised by an important bending at the southern tip. The direction of the coastline at south of Madagascar changes between 45.5°E and 46°E. The coastline from 46°E and 47°E tends in North-East direction while between 45.5°E and 44°E follows a North-West direction. Change in the coastline direction can influence and impact on the effectiveness of the winds to drive upwelling. Therefore, it is necessary to analyse wind inside zones before and after the bending. We define suitable wind product for the study by comparing four wind data products: QuickSCAT, ASCAT, CCMP-FLK and Era-Interim.

The QuickSCAT wind data set is the global surface wind product provided by NASA (Risien & Chelton 2008). Data are measured from the near polar synchronous orbital QuikSCAT satellite. In this study, we used pre-gridded (L3) QuickSCAT data at 0.25° resolution grid over the 1999 to 2009 period. Daily wind data are downloaded from (`https://winds.jpl.nasa.gov/missions/quikscat/`). Thereafter, monthly composites are calculated from daily maps.

Winds are derived using observations from the Advanced SCATterometer (ASCAT) onboard the Meteorological Operational (Metop) launched by the EUropean organisation for the exploitation of METeorological SATellites (EUMETSAT). The ASCAT wind product is an improved surface wind speed and direction dataset which is subjected to stringent quality control procedure to remove bias due to the rain and coastal contamination (Global 2013). In this

study, monthly composites are derived from the pre-gridded (L3) ASCAT daily maps (https://podaac-opendap.jpl.nasa.gov/opendap/allData/ascat/preview/L2/metop_a/25km/) at 0.25° resolution grid over the 2009 to 2016 period.

The CCMP-FLK (Cross-Calibrated Multi-Platform/First-Look Analyses) wind dataset was derived from the Cross-Calibrated Multi-Platform (CCMP) project. The product merges satellite observations from SSM/I (Special Sensor Microwave Imager), SSMIS (Special Sensor Microwave Imager/Sounder), AMSR-E (Advanced Microwave Scanning Radiometer - Earth Observing System), QuikSCAT (Quick Scatterometer), SeaWinds, WindSat (Satellite-based polarimetric microwave) and other satellite instruments as they become available from REMSS. The CCMP-FLK wind dataset also includes observations from Tropical Rainfall Measuring Mission - Microwave Imager (TRMM TMI) ocean surface winds from the Tropical Rainfall Measuring Mission (TRMM) platform (Atlas et al. 2011). In this study, monthly composites of CCMP-FLK are collected from NASA data portal https://podaac-opendap.jpl.nasa.gov/opendap/allData/ccmp/L3.5a/monthly/flk/. We use the gridded level 4 data at 0.25° resolution grid, over the period from 1990 to 2011.

The ERA-Interim atmospheric reanalysis is a wind product provided by the European Centre for Medium-Range Weather Forecasts (ECMWF) (Dee et al. 2011). ERA-Interim is a global gridded data product covering the period from 1 January 1989 onwards. Monthly composites are constructed from the 3-hourly surface wind with a 0.25° resolution grid.

Comparison-test was applied to products listed above derived from different technics of measurement for their capacity to measure wind in the upwelling region: two from scatterometry (QuickSCAT, ASCAT), one from cross-calibration (CCMP-FKL) and the last is a reanalysis (ERA-Interim). Inshore wind data in CCMP-FLK and ERA-Interim have been removed to maintain consistency with the QuickSCAT and ASCAT data which don't have data near the coast for the further comparison.

As we have the same grid resolution in each product which is 0.25° (25 km), we masked the land including the first pixel from the coastline in the wind product CCMP-FKL and the ERA-Interim reanalysis to be comparable with the QuickSCAT and ASCAT wind product spatial structure, using similar approach applied in the south-east Pacific coastal upwelling (Croquette et al. 2007).

To identify better the differences between products, wind data are extracted in three specific zones (Figure 3.5). The main zone covers the upwelling region (Figure 3.5 (grey box in the

map)). Two small zones are extracted from the main zone: Zone 1 is the zone before the bending (East of the southern tip (Red in the map)), and zone 2 after the bending (West of the southern tip (blue in the map)).

Figure 3.5 shows wind roses from the four wind data products described above which characterise direction and intensity of wind taken inside the upwelling region (grey box in the map). Wind roses show that the upwelling regions are strongly influenced by the easterly trade winds. All panels "a, b, c, d" show that wind blows towards two well defined directions which are towards the west (270°) and North-west directions (305°). Winds towards (270°) appear to be predominant for all products except for QuickSCAT. Although products depicted the same direction, intensities and densities of wind data appeared to be different in each product.

Before the southern tip (zone 1), QuickSCAT and ASCAT show a clear westward predominant direction and their velocities are quite similar. CCMP-FKL and Era-Interim appeared to have similar directions which are the westward and a south-west direction (180°). In term of speed, CCMP-FKL and ERA-Interim appear to have low velocities, averagely between 5 to 6 ms^{-1}, while QuickSCAT and ASCAT can exceed 7 ms^{-1}. After the southern tip (zone 2), all products depicts a North-west direction (305°) with a velocity averaged between 6 to 7 ms^{-1}. Based on the comparison provided above, products show similar features but different intensities in the upwelling region. ASCAT wind product appear to show features existent in all products. Therefore, the study opts to use mostly the ASCAT wind product.

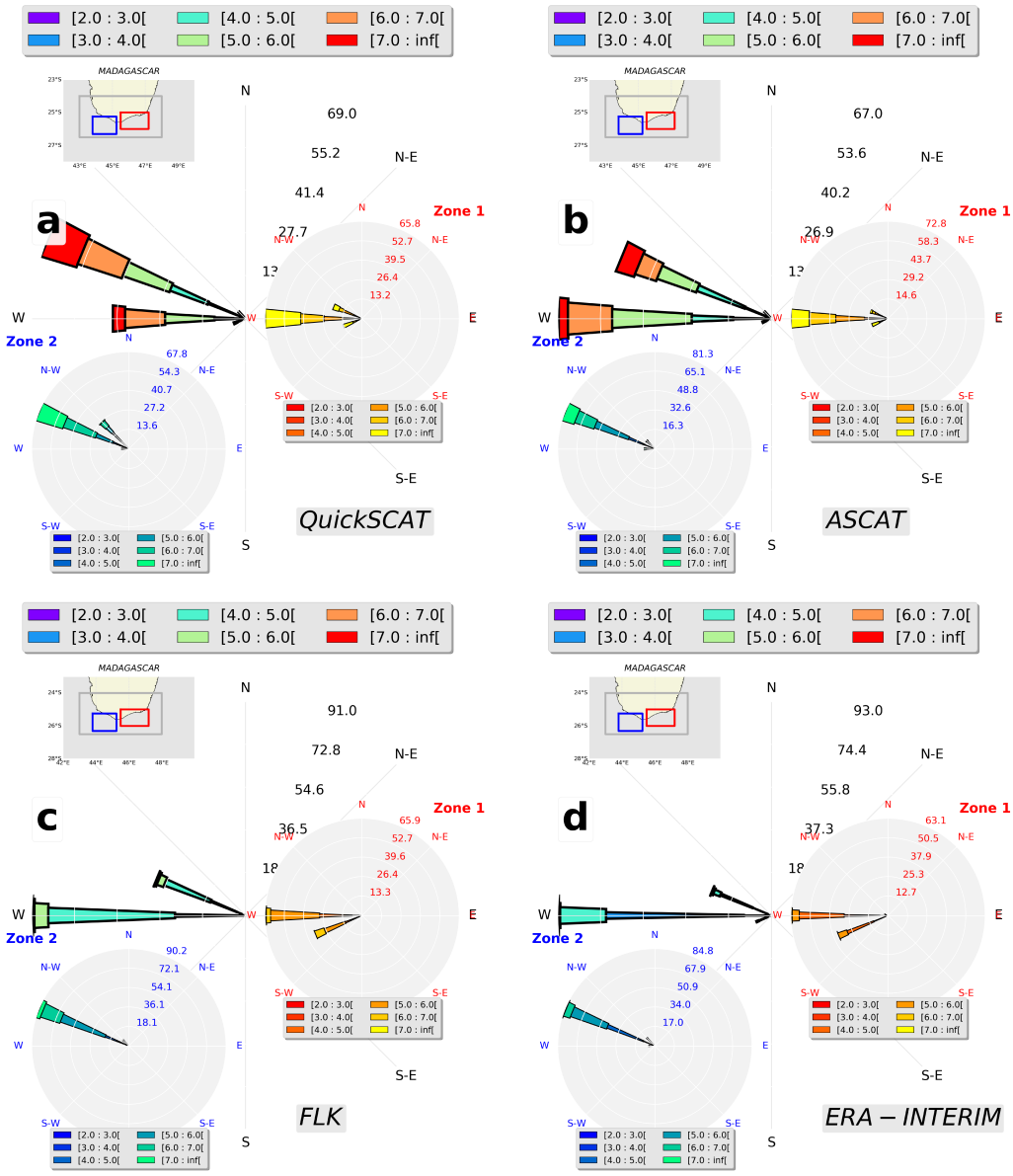

Figure 3.5: Wind roses of surface wind intensity from different products in the upwelling zone. Large wind roses in the middle represent wind intensity and direction retrieved from the entire upwelling area (from the grey rectangle on the map), while small polar plots represent surface wind intensities and directions retrieved from the rectangle in red (called zone 1) and in blue (called zone 2). a- Wind rose in the upwelling zone derived from QuickSCAT, b- ASCAT, c- CCMP-FLK and d- Era-Interim.

3.2 Ocean model: CROCO

Very few in-situ measurements were undertaken in the region of the upwelling and there is a real lack of observations of the vertical structure of the water column in the upwelling region. Land contamination also makes it difficult to estimate the reliability of satellite data at the coast to investigate the mechanism associated with, as explained in the subsections above (3.1). Therefore, the study uses CROCO ocean model to reproduce the upwelling system and reinforce findings found in observational analyses.

Coastal and **R**egional **O**cean **CO**mmunity model (CROCO) is part of a new generation of three dimensional ocean circulation model previously named Regional Ocean Modeling System (ROMS_AGRIF) (Debreu et al. 2012, Shchepetkin & McWilliams 2005). CROCO (`https://www.croco-ocean.org/`) is a numerical computational model conceived to simulate the dynamics of the ocean in three dimensions, based on the numerical resolution of Naviers-Stokes equations (Shchepetkin & McWilliams 2005, Debreu et al. 2012). The Naviers Stokes equations are the primitive equations governing the motion of the ocean (Chorin 1968). CROCO solves the primitive equations in a planetary rotating frame and takes into account Boussinesq and hydrostatic approximations for an incompressible ocean (Shchepetkin & McWilliams 2005). Detailed description of the equation solved by CROCO model are fully presented by Haidvogel & Beckmann (1999), Shchepetkin & McWilliams (2005), Debreu et al. (2012). CROCO uses the σ-coordinate system. The CROCO vertical layer structures are conceived to follow the bottom topography structure which allows the model solution to have an important interaction with the topography (Shchepetkin & McWilliams 2005). A CROCO configuration requires the surface, lateral and the sea floor boundaries conditions to be prescribed as initial input parameters for the calculation process (Shchepetkin & McWilliams 2005).

The CROCO model solutions provide principal physical parameters: u, v, T, S, ζ, which are reproduced in three dimensional structures of ocean dynamics (Debreu et al. 2012).

Additional explanations of CROCO specificities and the approximated numerical model equations are fully provided in Appendix A.1.

According to the needs elaborated in the beginning of this subsection, two model configurations are launched. The first configuration is a realistic simulation which reproduces the real state of the ocean dynamics, and another configuration is used for sensitivity experiments.

3.2.1 Realistic Simulation

In order to reproduce the vertical column structure of the upwelling system, a realistic oceanic simulation is required. The simulated upwelling is compared with various observation data sets with the purpose of evaluating the model solution which will be elaborated later on in this section.

3.2.1.1 Model configuration

Outputs of a nested configuration of the CROCO are used in this study. A large-scale domain is defined as parent grid while a small regional domain is the child grid. The first simulation is applied to the parent domain, which has a lower resolution, with the aim to solve large-scale patterns. The parent simulation provides the boundary conditions for the following simulation which is the child model. The child model has a higher resolution and focuses on a regional scale. In return, the child model also provides an improvement to the parent model solution (Debreu et al. 2012). The two-way nested approach allows a run with a high-resolution grid at low cost.

The parent grid resolution is $\frac{1}{4}^\circ$ degree, and the domain extends from 10°W to 102.25°E and 3.18°S to 55.7°S, while the child resolution is $\frac{1}{12}^\circ$ degree grid over the 6.08°E to 54.16°E and 7.49°S 46.43°S region (Figure 3.6). The vertical grid of the child model consisted in 60 levels with the following values of surface, bottom and minimum depth-stretching parameters: theta s=5, theta b=0, hc=10 m.

The model is run over the period 1993-2013 using a $\frac{1}{12}^\circ$ degree resolution nested grid (Figure 3.6), and the outputs were averaged every day.

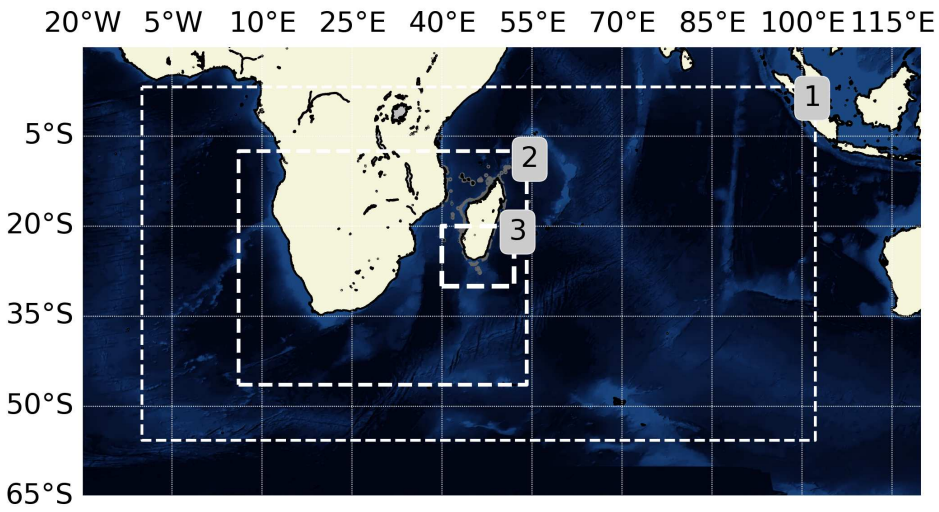

Figure 3.6: Areas covered by the models. (1) and (2) are the realistic simulation, where (1) is the parent domain and (2) is the child domain. (3) is the domain used for the idealised simulation.

3.2.1.2 Topography, surface forcing and lateral boundaries condition

The model topography is derived from General Bathymetric Chart of the Oceans (GEBCO) dataset (`www.gebco.net`) with 30 seconds grid spatial resolution grid. Both parent and child grid topographies are smoothed in order to keep the slope of bathymetry structure with the aim to avoid errors associated with vertical layers of σ (Haidvogel & Beckmann 1999) .

The model surface conditions are derived from the ERA Interim atmospheric reanalysis (Dee et al. 2011) , collected from the European Centre for Medium-Range Weather Forecasts (ECMWF) (`http://apps.ecmwf.int/datasets/data/interim-full-daily/levtype=sfc/`), to calculate wind stress using a bulk formulation (Fairall et al. 1996).

The lateral boundary conditions are forced by the Mercator global ocean reanalysis GLORYS (Ferry et al. 2012).

At the start of the simulation, 3 years are used for the model spinup.

The model outputs are compared with satellite observations (Figure 3.7). The main characteristics of the upwelling are well reproduced in the model (Figure 3.8).

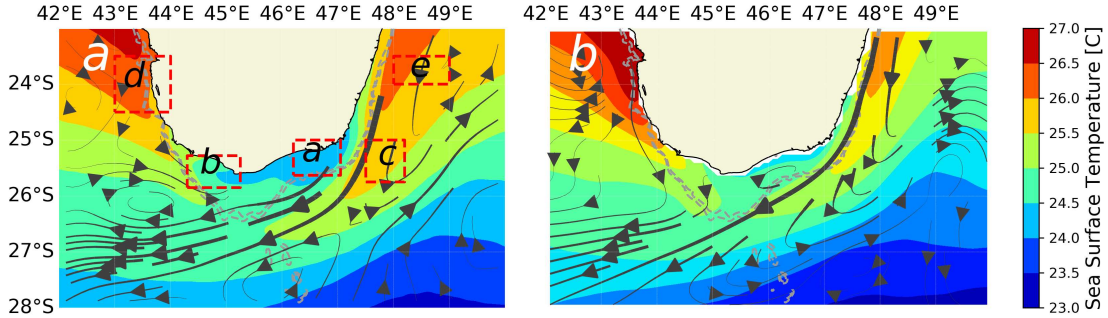

Figure 3.7: Comparison between satellite observations and the model outputs. (a) Mean MUR SST and streamlines of mean ocean velocity from GlobCurrent over the period 2003-2015. (b) Mean SST and streamlines of mean ocean velocity from the model over the period 1993-2013. Red rectangles (a, b, c, d, e) are zones where time series were extracted for the comparison between model output and satellite observations.

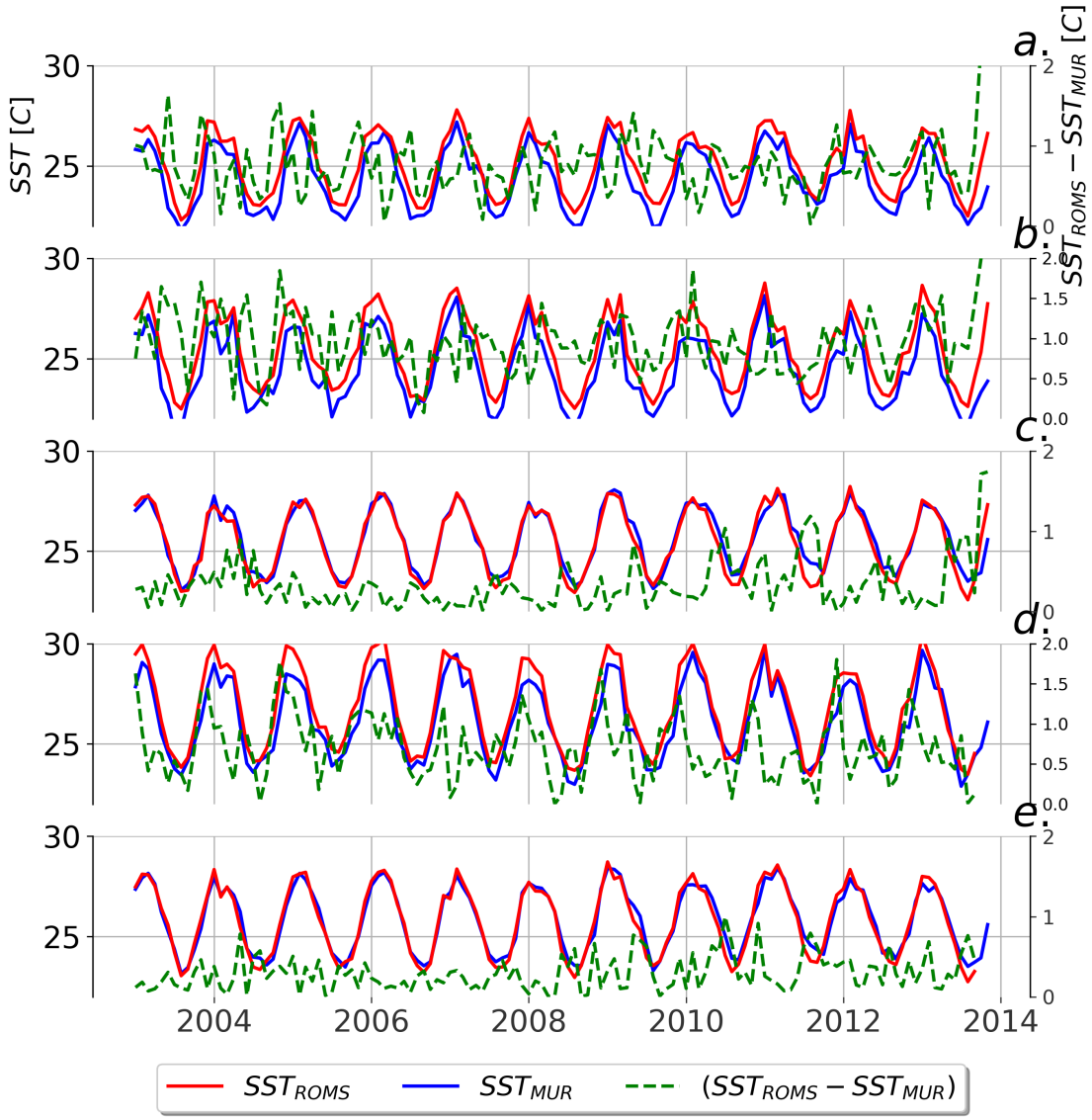

Figure 3.8: Comparison between satellite observations and the model outputs. SST time series from the model (red) and MUR product (blue) spatially averaged over the regions highlighted with the red rectangles shown in Figure 3.7. Timeseries of SST differences (Green) between the model and the MUR SSTs.

3.2.2 Idealised Simulation

3.2.2.1 Model configuration

The response of the coastal upwelling to different forcings is investigated by conducting idealized simulations.

The aim of the idealized test is to isolate the different contributions of wind and currents to force the upwelling. Wind and current are the main parameters which regulate the upwelling mechanisms based on the literature review (Chapter 2). The changes applied to these parameters (increase or decrease) are expected to produce a significant sensitivity in the upwelling system. The parameter targeted for the sensitivity test is the along-shore wind stress (Risien & Chelton 2008, Benazzouz et al. 2014, Jose et al. 2016). Only wind sensitivity is applied because result from the test can indicate if the wind induces significant change, otherwise, ocean current contribution will be considered as the upwelling main driver.

An idealised simulation requires a "reference simulation" which is the normal run. Thereafter, the reference simulation is compared with the idealised simulation where we applied modification in the surface forcing to quantify separate contributions of these two upwelling forcing mechanisms.

3.2.2.2 Topography, surface forcing and lateral boundaries condition

The grid extended from 40°E to 53°E and from 10°S to 30°S (Figure 3.6) with a resolution equal to $\frac{1}{12}^{\circ}$ degree. The number of vertical levels configured is 40 levels. Vertical grid parameters applied are theta s=6, theta b=0 and hc=10 m.

The topography used during the simulation is the two minutes worldwide bathymetry (ETOPO 2) which is available within the CROCO package at `https://https://www.croco-ocean.org/download/croco-project/`.

The simulation used is a one way simulation and it is a climatology run.

QuikSCAT wind climatology, at $\frac{1}{4}^{\circ}$ degree resolution, is the surface forcing applied for the simulation and interpolated to the CROCO grid afterwards.

The lateral boundaries of the model are initialized with salinity and temperature monthly climatological fields from the World Ocean Atlas (WOA 2005) at 1° (Conkright et al. 2002) spatial resolution.

The model is run for 10 years, in which the outputs were averaged every 5 days. The integrated

physical properties of the model showed stable conditions after the third year. Therefore, the analyses applied for the study started from the fourth year into the end.
The model gives a good representation of the upwelled water at the south of Madagascar which we will show in detail in the following chapter.

3.2.2.3 Idealised approach

The subsection explains the applied approach to reduce the wind stress intensity in the upwelling region without changing the local circulation.
A circle surrounding the upwelling region is defined. The wind stress selected inside the circle is reduced following the Gaussian filtering. The wind stress is reduced to be equal to zero in the center of the circle and increases progressively following the typical Gaussian curve until the radius of the circle. We note that the intensity of wind stress is reduced only inside the upwelling area (inside the circle) without changing the intensity of wind stress outside the upwelling area.

$$P(i,j) = \mathbf{Coeff}\ e^{(i-i_0)^2+(j-j_0)^2/2\,\mathbf{r}^2} \tag{3.1}$$

Where i_0 and j_0 are the center coordinates of a selected circle covering the targeted region, $\mathbf{r}$ is the radius and **Coeff** is the approximated coefficient for the Gaussian function which is equal 1 to retain the wind data in the selected area. Equation 3.1 is the reformulation of the standard Gaussian function (Vázquez et al. 1999) applied for two dimensional distribution in i and j dimensions.
Equation 3.1 is applied to the wind stress and it is illustrated in the Figure 3.9 which shows the change applied to the surface forcing for the idealised simulation.

3.3 Lagrangian experiment

Lagrangian dispersion models have been widely used to study a broad domain in oceanography such as fish larvae dispersion (Lett et al. 2008), plastics convergence in the open ocean (Maes et al. 2018), displacement of water masses (Vic et al. 2018), optimisation of marine top predators migrations (Kai et al. 2009), and so forth.

The Lagrangian trajectory simulation model is a developed concept for investigating displacement of a fluid parcel in a circulation system. Lagrangian dispersion modelling provides trajectories and dispersions in various scale of an element which can be passively transported with the flow, using ocean velocity fields $\vec{u} = (u, v, w)$, mostly from three dimensional ocean model output (Vic et al. 2018).

In this study, Lagrangian experiment is performed to investigate pathways of upwelled water propagations. An off line Lagrangian advection code described by Gula et al. (2014) is adapted for this investigation. The Lagrangian drifter-tracking code algorithm is written in Fortran, and is wrapped in Python for the easy interoperability in different utilisation.

The Lagrangian drifter-tracking code is computed to advect parcel of water in three-dimensional velocity fields, $\vec{u} = (u, v, w)$, using model solution from the realistic configuration (Subsection 3.2.1). A particle tracking model is applied to study upwelled water pathways using a fourth-order Runge-Kutta (RK4) integration method (Vic et al. 2018).

Particle tracking model solving the equation:

$$X_i(x_0, y_0, z_0)^{n+1} = X_i(x_0, y_0, z_0)^n + \int_{t_0+n\Delta t}^{t_0+(n+1)\Delta t} u_i(x, y, z, t)\, dt \tag{3.2}$$

The passive progression at each time step from n to $n+1$ period using three-dimensional velocity fields $\vec{u}$ is shown in equation 3.2. The second term of the equation 3.2 is the time integral requiring differential equation RK4 method solver.

Advection of particles is applied in each gridded locations from the model solution.

Particles can be seeded in three dimensional coordinates, vertical and horizontal location criteria, using the model solution dimension.

Particles can be released with continuous injection or once-off release by injection. Injection is the method applied to the $n+1$ particles which will be released at the same positions (origin) every time step and through all simulations. In this study, once-off release was performed for all Lagrangian investigations applied in this study.

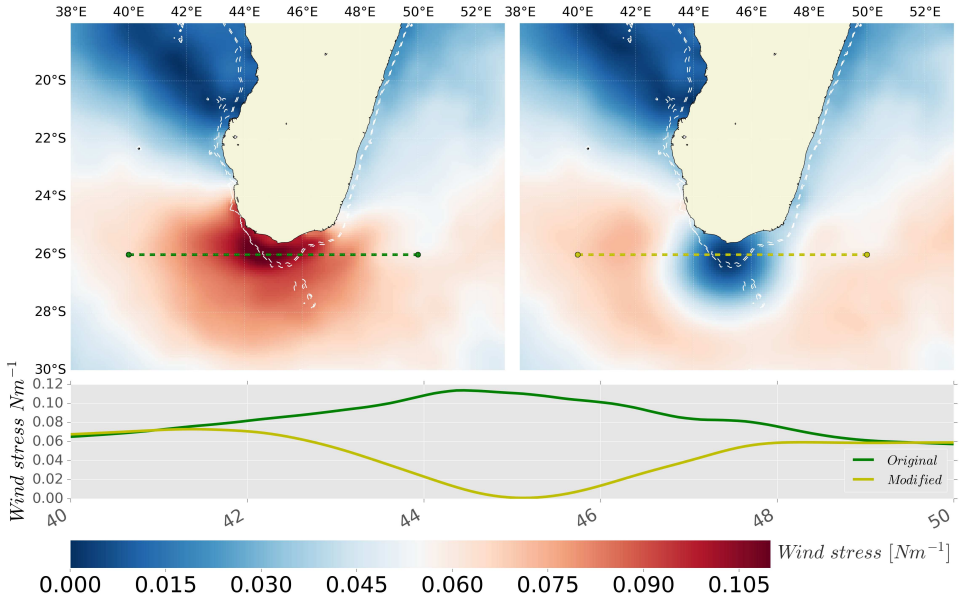

Figure 3.9: (Top-left) Wind stress climatology data from scatterometer QuickSCAT product covering the period 1999 to 2009. Dotted lines are a reference line to test the original and modified wind stress. (Top-right) Wind stress climatology data modified after applying the Gaussian approach in the upwelling area. (Bottom) Longitudinal variation of the original and modified wind stress cropped from the dotted reference line.

Chapter 4

Spatial and seasonal variability

This chapter is based on the work published as:

Ramanantsoa, J.D., Krug, M., Penven, P., Rouault, M. and Gula, J., 2018. Coastal upwelling south of Madagascar: Temporal and spatial variability. *Journal of Marine Systems*, 178, pp.29-37. Doi: 10.1016/j.jmarsys.2017.10.005.

4.1 Introduction

The marine coastal regions south of Madagascar are highly productive (Bemiasa 2009, Pripp et al. 2014). Biological production in these coastal regions is driven by an active coastal upwelling, which boosts coastal ocean fertilization. Several local biological studies have further confirmed that the coastal upwelling south of Madagascar is a hotspot of marine biological productivity (Houart & Héros 2013, Rakotoarinivo 1998). Satellite observation of Sea Surface Temperature (SST) and Chlorophyll-a concentration can be used to identify upwelling regions south of Madagascar as shown in Figure 4.1. In that synoptic map, cold waters near the coast associated with high Chlorophyll-a concentrations are indicative of a coastal upwelling event. A better understanding of the upwelling variability south Madagascar is essential to adequately manage and preserve these ecologically and economically important coastal regions (Bemiasa 2009).

Coastal upwelling south of Madagascar may also impact productivity over the larger south Indian Ocean. The region south-east of Madagascar and within the Southern Indian Ocean

Counter Current (Siedler et al. 2009) is subject to one of the largest chlorophyll blooms observed in the open ocean (Longhurst 2001, Wilson & Qiu 2008). The formation, propagation and termination of this bloom remain a topic of active research (Srokosz et al. 2015), but several studies point to a possible link between the coastal upwelling regions of Madagascar and the large bloom of phytoplankton spreading in south Indian ocean (Huhn et al. 2012, **?**). Consequently there is a strong need to adequately characterise and understand the mechanisms which drive this upwelling.

Limited studies have addressed the seasonality and variability of the coastal upwelling south of Madagascar. Ho et al. (2004) were the first to investigate its seasonality. Their work was based on an analysis of observations of Chlorophyll-a concentrations derived from the SeaWiFs sensor over the period 1997-2001. They showed that upwelling along the South Madagascar coastline was greater during the austral winter (May-Oct) than in the austral summer (Nov-Apr) months. A later study by Raj et al. (2010) further suggested that shallower mixed layer during summer season tended to promote the summer upwelling.

Coastal upwelling south of Madagascar is thought to be driven by coastal winds (DiMarco et al. 2000) and/or interactions between the East Madagascar Current (EMC) and the shelf (Lutjeharms & Machu 2000). DiMarco et al. (2000) argued that wind stress in austral summer favors upwelling events. However, Lutjeharms & Machu (2000) did not find a significant correlation between the wind and the presence of upwelled water near the coast. Instead, Machu et al. (2002) suggested that the formation of cyclonic eddies through interactions between the EMC and the continental shelf could influence the strength of the upwelling. Ho et al. (2004) also showed a link between upwelling and the EMC. The influence of the EMC on the coastal upwelling was later confirmed by the idealized modeling work of Jose et al. (2016) which illustrates the potential effects of the detachment of the EMC on vertical velocities.

This chapter seeks to provide an improved understanding of the spatial extent and seasonal variability of the upwelling south of Madagascar and clarify its complex generating mechanisms. For that purpose, we use satellite observations and outputs from an ocean numerical model.

Subsection 4.2 describes the observations, model and techniques used in this study. Subection 4.3 presents the characteristics of the upwelling cells, their extents, and their seasonal variations. Subection 4.4 addresses the relative role of the wind and the ocean currents as drivers of the coastal upwelling. A discussion and conclusions are presented in Subsection 4.5.

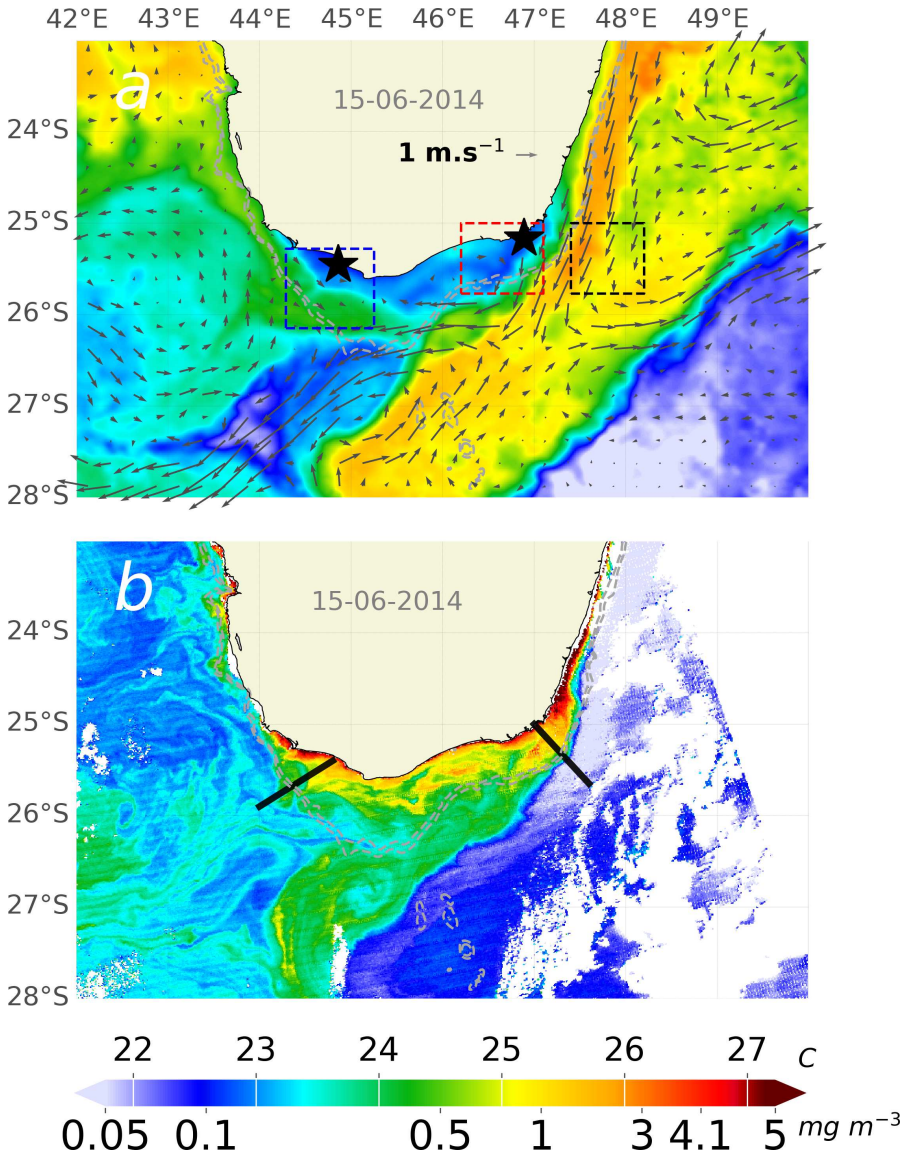

Figure 4.1: Correspondence between inshore cold water and Chlorophyll-*a* concentration response. (a) Map of sea surface temperature on the 15/06/2014 south of Madagascar. The black arrows represent the geostrophic current. Black stars are the position where the Lagrangian particles are released. The boxes are the relevant location for computing the sea surface temperature-based Coastal Upwelling Index. The red box (numbered 1) will represent upwelling cell Core 1, the blue box (numbered 2) will represent upwelling cell Core 2 and the black box will represent the offshore temperature. (b) Chlorophyll-*a* concentration on the same day. Dashed contour lines are the isobaths at 500 m and 1000 m depth. Black lines are transects taken inside respective upwelling cells.

4.2 Data, model and method

4.2.1 Observation

Table 4.1: Data sets and their sources. The first column lists the data source and the sensor (when applicable, in parentheses), the second column is the variable measured or estimated, the third column is the temporal resolution, the fourth column the spatial resolution (in degree), the fifth column the data record length, and the sixth column the Internet resource from which the data were downloaded.

Data source (sensor)	Variable	Composite	Grid resolution [Degree]	Period	URL
Aqua (MODIS)	Chlorophyll-a	Monthly	1/100	2003-2015	http://www.afro-sea.org.za/
MUR	SST	Monthly	1/100	2003-2015	http://mur.jpl.nasa.gov/
MetOp-A (ASCAT)	Wind	Monthly	1/4	2009-2015	http://www.ifremer.fr/cersat/en/data/data.html/
GlobCurrent	Surface currents	Monthly	1/4	2003-2015	http://www.ifremer.fr/opendap/cerdap1/globcurrent/

Table 4.1 details the dataset used in this chapter. The Multi-Scale Ultra-High Resolution (MUR) SST is used in this chapter based on the product reliability of showing the coastal upwelling demonstrated in Chapter 3. Since we are focusing on the seasonal cycle, we use monthly data calculated from daily data.

Wind fields observed from the Advanced Scatterometer dataset (ASCAT METOP-A) (Table 4.1) were used. The ASCAT sensor is less prone to rain and land contamination (Hilburn et al. 2006) and therefore well suited for coastal regions. This wind product is operationally monitored and processed through EUMETSAT (Hasager et al. 2015).

The Moderate-Resolution Imaging Spectroradiometer (MODIS) Chlorophyll-a was downloaded from the NASA Ocean Color Nasa website and processed by the Marine Remote Sensing Unit (MSRU, Cape Town, South Africa). Monthly composites of Chlorophyll-a concentrations are derived from the 1 km gridded L3 Aqua MODIS daily maps.

The GlobCurrent product is a combination of geostrophic currents from satellite altimetry and Ekman currents calculated from ECMWF ERA INTERIM reanalysis winds (Johannessen et al. 2015). The GlobCurrent data are provided at a 3-hourly frequency, and on a 1/4 degree grid resolution. They are combined as monthly composites for this study.

We also used a 2.5-year time series (10/2010 to 02/2013) of the EMC volume transport to investigate the relationship between EMC and upwelling intensity. The EMC transport data were derived from Acoustic Doppler Current Profiler (ADCP) observations collected across the EMC at a latitude of 23°S. The dataset provided by the NIOZ (Royal Netherlands Institute for Sea Research), was collected during the INATEX research project (Ponsoni et al. 2016).

4.2.2 Model set up and Lagrangian experiment

To investigate the physical drivers of the upwelling, we analysed outputs from a regional ocean model and performed additional numerical sensitivity studies. We used the outputs of a nested configuration of the Coastal and Regional Ocean Community model (CROCO) explained in the chapter 3.

The influence of the coastal circulation is investigated by tracking the origin of the water masses that feed into the coastal upwelling cells through a Lagrangian particle tracking experiment applied to the model outputs. To define major pathways of upwelled water, three-dimensional velocity fields are used to advect the particles of water backward in time over a two-month period. Particles are advected using the code described in Gula et al. (2014). Particles are released at the two locations shown as black stars in Figure 4.1. The particles are released every 5 m in the upper 50 m. 168 particles are released in a first upwelling cell (46.8°E - 47.2°E; 25.1°S - 25.5°S) (Core 1: southeast of Madagascar; Figure 4.1) and 126 in a second cell (44.7°E - 45.1°E; 25.45°S - 25.85°S) (Core 2: southern tip of Madagascar; Figure 4.1) every year from 2003 to 2013.

In addition, a second model configuration is used for idealized simulations. The model has a 1/12 degree grid resolution similar to the first configuration. It is forced by a QuickScat wind stress climatology and the boundary conditions are constructed from the World Ocean Atlas (Conkright et al. 2002). The model is able to reproduce the coastal upwelling. These idealized simulations are used to perform sensitivity studies and investigate the role of the wind stress, the EMC, and the coastal circulation as drivers of the coastal upwelling.

4.2.3 Upwelling frontal detection

A front detection algorithm is applied to monthly SST maps to identify surface temperature fronts south of Madagascar. The method proposed here is an adaptive Canny edge detector applied on multiple images (Canny 1986). Each monthly SST composite map is preliminarily low-passed filtered using a Gaussian filter with a sigma value of 1 (Higdon 1998), to omit small scale variability. A Sobel operator with a fixed 3x3 window is then used to highlight the regions associated with the strongest SST fronts in the monthly images (Simhadri et al. 1998, Ping et al. 2016). Following that step, only the strongest gradients in a 3x3 window and along both an East-West and North-South axis are selected (Othman et al. 2012). Afterwards, the monthly

upwelling fronts are defined as frontal regions tracked from a range of optimal thresholds of SST gradient following the formula in Othman et al. (2012), $T_{low} = \frac{1}{2}T_{high}$, where T_{low} is average lower gradient and T_{high} is the optimal higher gradient in our case falling with a range of 0.76°C.km^{-1} and 1.51°C.km^{-1}. Lastly, all monthly frontal maps are combined seasonally to identify only the zones with a high number of frontal occurrences.

4.2.4 Upwelling spatial extent

The spatial extent of the upwelling cell is estimated by following a surface isotherm encompassing the colder coastal upwelled waters. The value of isotherm used is calculated following Veitch et al. (2010), according to equation 4.1.

$$SST_{upwelling} = 0.25SST_{coast} + 0.75SST_{offshore} \tag{4.1}$$

where SST_{coast} [°C] is the lowest SST inside the upwelling zone located over the shelf south of Madagascar, and $SST_{offshore}$ [°C] is taken off the southern tip of Madagascar in the vicinity of the 1000 m isobath, averaged over the longitudes 45°E, 46°E and latitudes 26°S, 27°S.

4.2.5 Upwelling index

We computed a SST-based Coastal Upwelling Index (CUI) adapted from Demarq & Faure (2000) method:

$$CUI = \frac{SST_{offshore} - SST_{coast}}{SST_{offshore} - SST_{mean}} \tag{4.2}$$

Where SST$_{offshore}$ is the mean warm SST inside the black box in Figure 4.1, SST$_{coast}$ is the mean SST in red or blue box in Figure 4.1, and SST$_{mean}$ is the temporal average of SST$_{coast}$. The SST difference is taken between the monthly temperature in the coastal zone (SST$_{coast}$) for each upwelling cell (red box or blue box in Figure 4.1) and the offshore temperature (SST$_{offshore}$) at the same latitude inside the core of the EMC (black box in Figure 4.1) using a similar approach to that described in Benazzouz et al. (2014). The box chosen to derive SST$_{offshore}$ has been carefully selected to account for the influence of the EMC on coastal upwelling (Lutjeharms & Machu 2000, DiMarco et al. 2000, Ho et al. 2004). This difference is

normalized by dividing by the difference between $SST_{offshore}$ and the temperature averaged in time over both coastal boxes (SST_{mean}) to account for seasonal solar heating as described by Alvarez et al. (2011) and Gonzalez-Nuevo et al. (2014). The CUI ranged from a value of 0 (no upwelling) to values greater than 1 which are indicative of strong upwelling.

4.2.6 Cross Shore Ekman Transport

To test the influence of winds on coastal upwelling, we estimate the cross shore Ekman transport (CSET) following the methods described by Bakun (1975). The cross shore Ekman transport is derived using the component of the wind stress parallel to the coast.

$$\tau_{alonshore} = C_d \rho_a V^2 (\beta - \alpha) \tag{4.3}$$

$$CSET = \frac{\tau_{alongshore}}{\rho_o f} \tag{4.4}$$

Where, $\tau_{alongshore}$ $[m^2.s^{-1}]$ is the along shore wind stress, ρ_a $[kg.m^{-3}]$ is the density of air at 10 m above the water surface, Cd is the dimensionless drag coefficient following Large & Pond (1981), V $[m.s^{-1}]$ is the 10 m wind speed, α is the wind direction, β is the dominant coastline angle (azimuth), ρ_o $[kg.m^{-3}]$ is the density of water, and f is the Coriolis parameter.

4.3 Characteristics, extent, and seasonal variations of the upwelling cells

4.3.1 Spatial patterns of cold coastal temperature

The mean SST over the period 2003-2015 shows the presence of colder water close to the coast south of Madagascar (Figure 4.2a). This upwelled water lies over the shelf between the 0 m and the 500 m isobaths with the lowest temperatures near the shore. On average, this upwelled water is 1.65°C colder than the waters offshore. The upwelling extends from 24.4°S along the south-east coast, north of Taolagnaro (also called Fort Dauphin), to Cap Sainte-Marie (25.6°S), the southernmost point in Madagascar (Figure 4.2a). The transition between the cold upwelled water and the offshore warm water is sharp. The offshore warm water is transported by the

EMC from the east, and another warm water at the south-west appearing to be a surface flow extends from the Mozambique Channel to the western side of Madagascar (Figure 4.2a). The transition between cold and warm waters is more gradual in the southern part of the shelf, probably due to an important eddy variability there (Halo et al. 2014).

Figure 4.2b shows the root mean square (RMS) of the annual SST cycle. Warm surface waters associated with the EMC display less variability (1.45°C RMS) than those located further west where RMS values range from 1.7 to 2.1°C (Figure 4.2b). The largest RMS values of 2.1°C are encountered in the southwestern coastal regions located closest to the Mozambique channel. In comparisons, the SST RMS near Taolagnaro is of the same order of magnitude as is SST RMS within the neighbouring EMC waters.

The inter-annual SST RMS based on SST anomalies is shown in Figure 4.1c. Again, the inter-annual variability in the western coastal upwelling regions, off Cap Sainte-Marie, is higher. These upwelling regions are associated with inter-annual RMS values of 0.72°C. On the southeastern side, the upwelling coastal regions and the EMC both display low inter-annual variability with a RMS value of 0.4°C. These results suggest the presence of two distinct cold water bodies with different annual and inter-annual levels of variability: Core 1, in the southeastern corner of Madagascar, and Core 2, west of the southern tip of Madagascar.

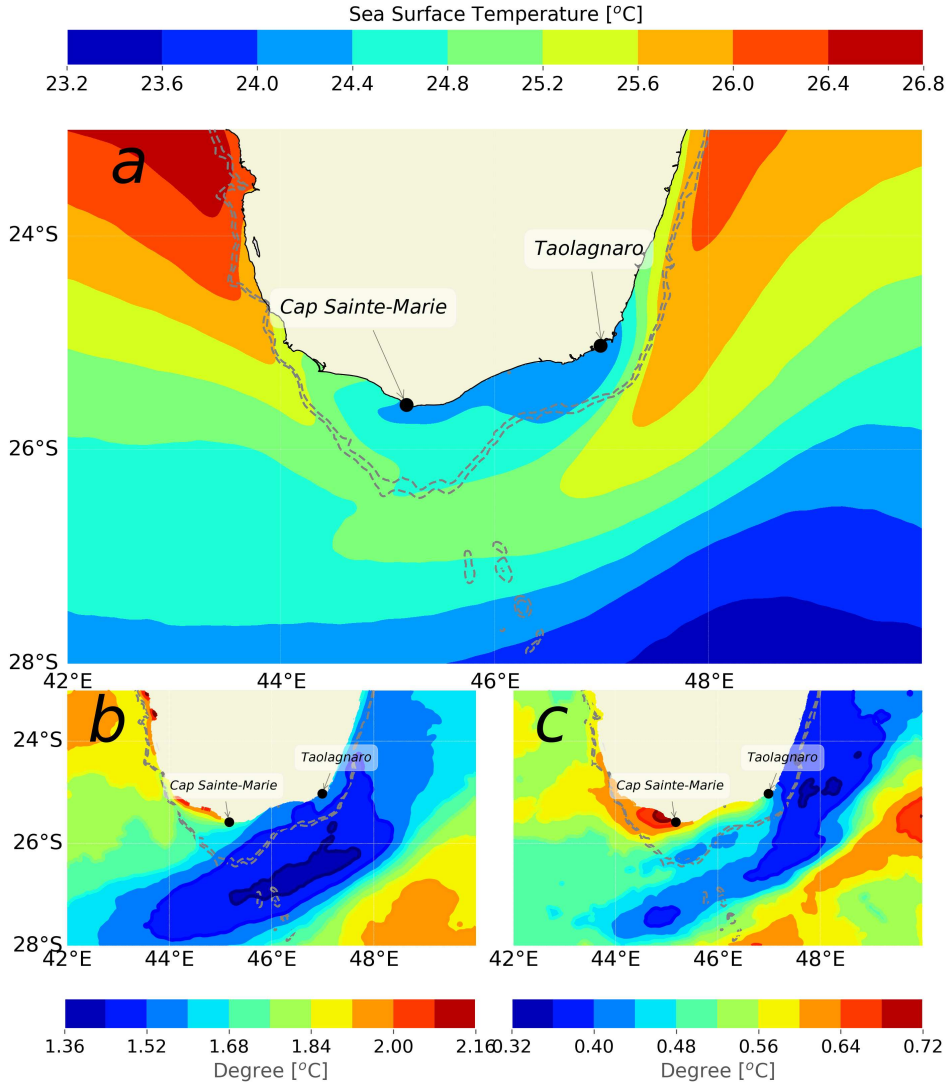

Figure 4.2: (a) Mean SST for 2003-2015 using MUR SST product which reflects the strong signature of inshore cold water, marker of coastal upwelling, south of Madagascar. Grey dotted lines are isobaths at 500 m and 1000 m. (b) Root Mean Square (RMS) of the annual SST variation. (c) Root Mean Square (RMS) of the interannual SST anomaly for 2003-2015.

Figure 4.3 shows the spatial distribution of the monthly occurrence of cold water events detected within the entire study region (43°E - 48°E; 24°S - 26.5°S). Coldest waters in the monthly dataset occur in two distinct locations. The first location (Core 1), lies in the south-east corner of Madagascar close to Taolagnaro, around 47°E and 25°S. Our analysis shows a fairly wide and scattered spatial distribution for these cold pockets of waters which encompasses the region of cold mean SST seen in Figure 4.2a. It is located at the inshore edge of the detached EMC, where a well-defined minimum of temperature can be observed throughout the year. The second region where cold waters occur is found at the south-west corner of Madagascar, in the vicinity of 45°E, where Core 2 is located. The spatial distribution of coldest water events in this region shows less scatter and a more coherent grouping and is coincident with the location of the mean colder water features in Figure 4.2a. These findings confirms that upwelling South of Madagascar, identified through the analysis of both mean and minimum surface water temperature values, occurs within 2 different cells: Core 1 and Core 2. The Core 1 is subjected to a high spatial spread and higher frequency of cold water events than in Core 2 (Figure 4.3). This explains the perennial behaviour of Core 1 which which shows less variability than Core 2 (Figure 4.2b and 4.2c).

Using the SST minima ($SST_{upwelling}$) associated with the two upwelling cores, defined in equation 4.1, we compute the percentage occurrence of colder water between 2003 and 2015 to determine the persistence of coastal upwelling south of Madagascar. Figure 4.3 shows that upwelling occurs in Core 1 almost 70% of the time, illustrating its permanent nature. The maximum value is about 50% for Core 2, in agreement with the higher variability seen on Figure 4.2.

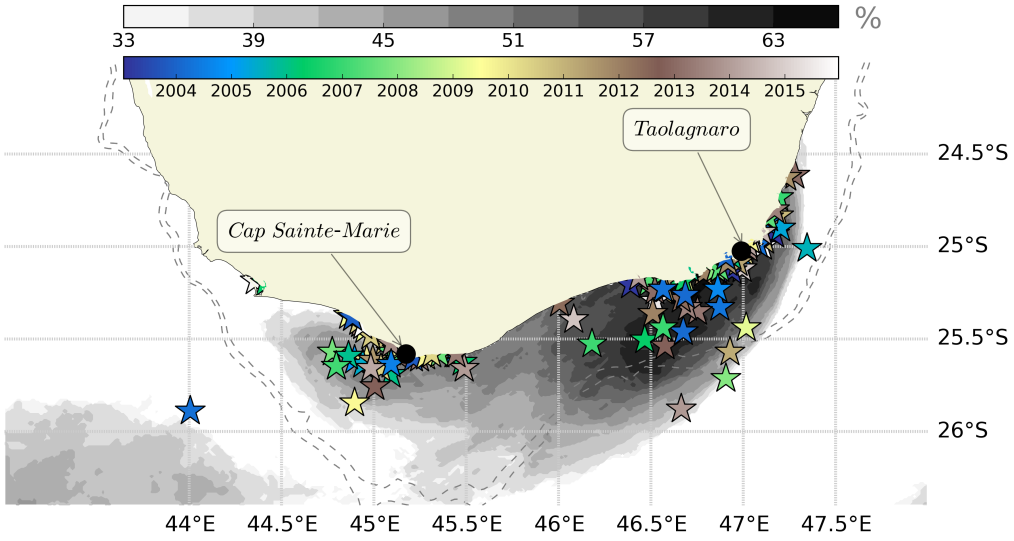

Figure 4.3: Spatial distribution of the lowest temperature. Stars represent the lowest temperature each month over the period 2003-2015 taken for the whole upwelling region. The occurrence of cold water (in %) over the same period, is shown in grey scales.

4.3.2 Seasonal extensions of the upwelling cells

The aim of this section is to highlight the seasonal characteristics of the two cores. To better identify regional variations in upwelling strength and spatial extent, we identify SST fronts with the frontal detection algorithm described in section 4.2.3 Figure 4.4 presents the occurrence of SST fronts between 2003 and 2015. These SST fronts delineate the borders of the two upwelling cores for each season. SST fronts are present all year long, east and west of Core 1, and on the southern part of the shelf, inshore of the EMC. SST fronts are also detected around Core 2 in Summer (JFM), Fall (AMJ) and Winter (JAS). This confirms the presence of two well-defined upwelling cores on the eastern and western part of the upwelling. The eastern boundary of Core 1 is quite spatially invariant throughout the year. It extends from the east coast to the southern tip of Madagascar, following the shelf break between the 1000 m and the 2000 m isobaths. However, the southern extension of Core 1 is more seasonally variable, being more defined in fall and winter and less evident in Spring (OND). The western boundary of Core 2 is distinguishable in summer, fall and winter (Figure 4.4). It starts from the southwestern corner of Madagascar at 25°S, and follows the shelf along the 1000 m isobath and in a southeastern direction. Another front can be observed south of Madagascar between the two cores (for example at 45°E in Winter, Figure 4.4c), highlighting their different water characteristics and

behaviour. The result emphasizes that Core 1 is almost permanent throughout the year but is more intense in autumn and winter. Core 2 is present for the first three seasons of the year but less visible in spring.

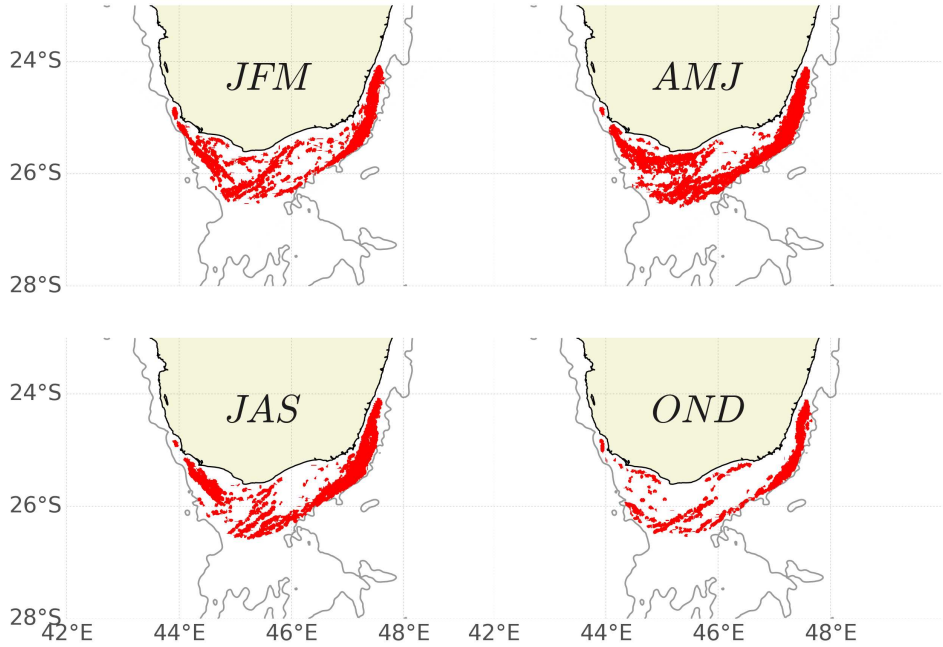

Figure 4.4: Seasonal distribution of coastal upwelling fronts based on SST. Red lines are SST fronts detected over the period 2003-2015, based on multiple image canny edge detection method. Grey lines are 2000 m isobath.

Based on a multisensor of satellite data analysis conducted by (Lutjeharms & Machu 2000), they observed that upwelling cell is more apparent in ocean colour than in the SST. Related to this, Figure 4.5 concomitantly provides a seasonal variation of SST and Chlorophyll-a concentration. Figure 4.5 shows spatial correspondence between cold water and Chlorophyll-a response in seasonally time scales. Figure 4.5 also reveals that the Chlorophyll-a concentration has a perennial signature throughout the year. The Chlorophyll-a concentration is maximum in JAS, while it is minimum in JFM and OND.

Now that we have identified two distinct upwelling cores, we will characterize the differences between these two cores and focus on upwelling intensities.

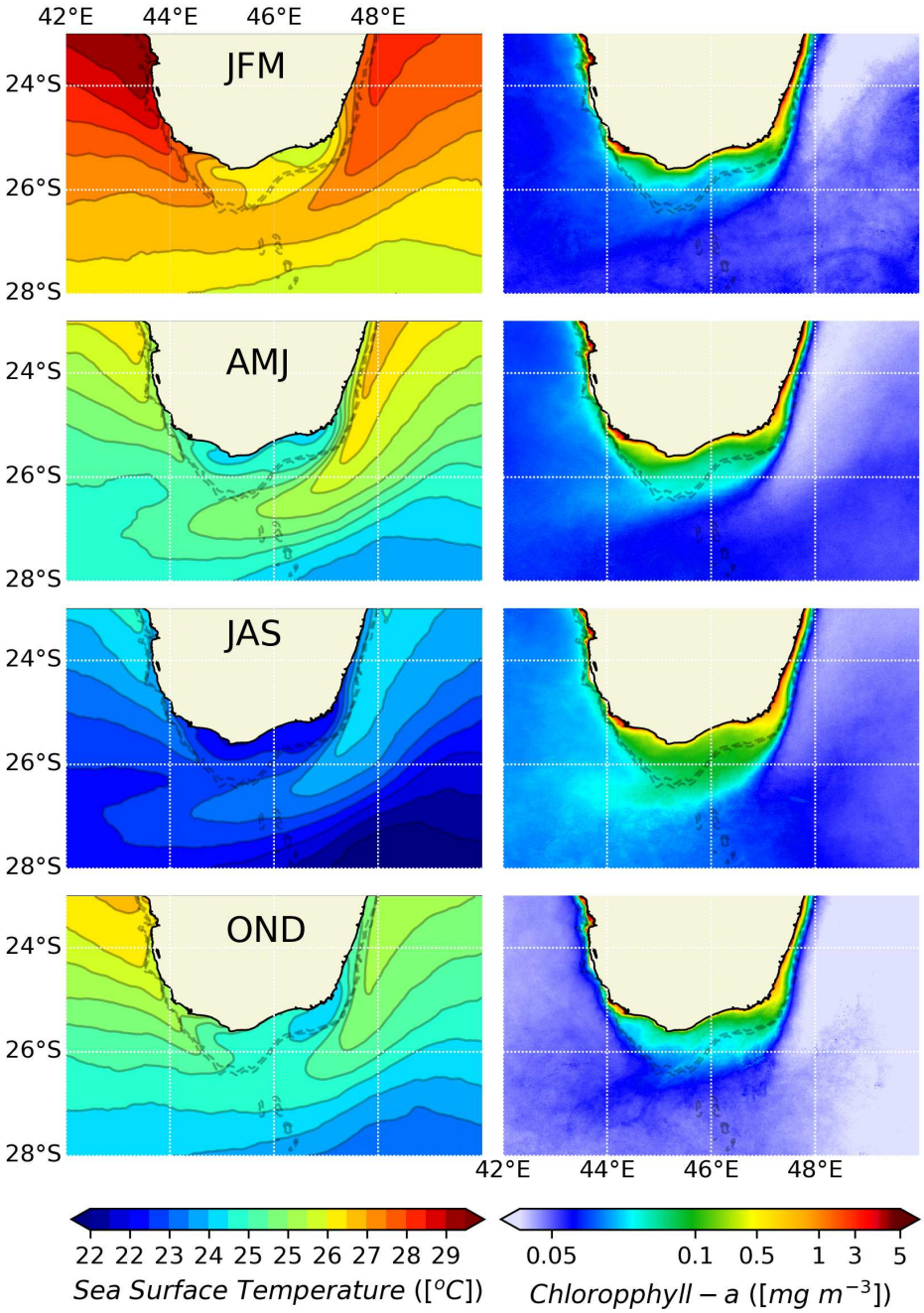

Figure 4.5: (Left) Seasonal map of SST from MUR product during the period of 2003-2015. Contour intervals represent 0.5°C of SST. (Right) Seasonal map of Chlorophyll-a concentration from MODIS Aqua product the same period. Dashed lines are isobath for 500 m and 1000 m depth.

4.3.3 Seasonal variations of core intensity

Figure 4.6 presents the monthly climatology of the upwelling index (CUI) based on SST, presented in section 4.2.5, for the upwelling cells in Core 1 (red bold line) and Core 2 (blue bold line). It also shows the seasonal variations in Chlorophyll-*a* concentration and offshore Ekman transport. The variability of the CUI is dominated by a seasonal cycle with a maximum in winter for the two cores. In agreement with the results presented in the previous section, CUI variations show that upwelling is present throughout the year in Core 1. For Core 2, although the CUI also reaches a value of about 0.5 in winter, it is much weaker with almost no upwelling from October to January. While temperature differences across an upwelling front are not necessarily linked to upwelling (Gunther 1936, Oram et al. 2008), several characteristics of Core 2 point to the occurrence of active upwelling. Between October and January, surface waters in Core 2 are still generally colder than those of neighbouring waters but the spatial extent of Core 2 decreases. The high variability which characterises Core 2 which at times masks the upwelling, is probably caused by the wider range of mechanisms which impact surface waters in Core 2. This is reflected in the CUI standard deviation value which is 0.16 for Core 1 and 0.25 for Core 2. This analysis is again coherent with our results from the previous section which indicate a high annual variability found in Core 2. The CUI time series (Figure 4.6) further shows that the seasonal cycles in the two cores are not in phase, with the maximum upwelling in Core 2 leading the maximum upwelling in Core 1 by one month. A significant linear relationship over the entire time series is found between the upwelling index and the Chlorophyll-*a* concentration for the two cores with a correlation of 0.72 for Core 2 and 0.58 for Core 1. These relationships confirm the link between surface cold water signature and increased in cholorophyll A concentration through upwelling.

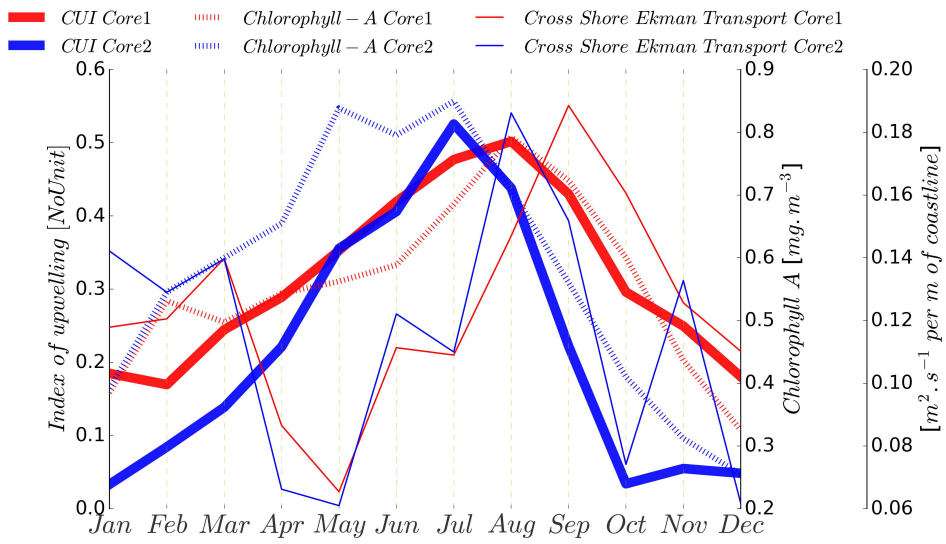

Figure 4.6: Bold solid lines are seasonal variation of coastal upwelling index. Dotted lines are seasonal variation of Chlorophyll-*a* concentration (mg.m^{-3}). Solid lines are seasonal variation of Ekman transport (m^{-2}.s^{-1} per meter of coastline) for Core 1 and Core 2 over the period 2003-2015.

Compared to the upwelling cells of Senegal and Morocco, where similar upwelling indices were used, the upwelling in the coastal regions of south Madagascar index is relatively weak. In the upwelling of Senegal and Morocco, temperature differences between the offshore and coastal regions are at times greater than 5°C and result in an upwelling index in excess of 1 (Demarq & Faure 2000, Benazzouz et al. 2014).

4.4 Mechanisms

4.4.1 Wind driven upwelling

The aim of this section is to identify the relationship between the CUI and wind forcing in each core. Cross Shore Ekman Transport (CSET) seasonal variations are calculated and plotted in Figure 4.6. We note that the CSET is calculated using dominant angles of the coastline from true East (18.3° for Core 1, −30° for Core 2), according to the equation 4.3, for orienting the wind stress direction following the shape of coastline at each Core.

For both cores, CSET seasonal variations present two periods of high intensity (winter and late summer) and decreases during two periods (fall and early summer) throughout the year. The first distinct phase is the increase of local wind and upwelling intensity in winter. Figure

4.6 shows that the CSET increases sharply from the beginning of winter (May) to late winter (September) for both cores. The upwelling indexes for both cores are also maximum in winter although they precede the maximum in cross-shelf Ekman transport. Another maximum of CSET is found in late summer (March) for both cores. This maximum is not as high as the winter peak and does not seem to be associated with a maximum in CUI (Figure 4.6). The CSET decreases significantly twice in a year. An important decrease happens at the beginning of summer (October-November). This decrease is coherent with the reduction of upwelling intensity at the end of winter. Another decrease of CSET is observed between March and May. During this period the wind stress decreases abruptly while the CUI remains strong in both cores. Next, we examine how changes in the orientation of the coastline and predominant wind directions impact on the intensity of the SST derived upwelling index.

In Figure 4.7, the south Madagascar coastline is smoothed to be able to extract the specific orientation of the different sections of the coastline. The sections are labelled “a” to “n”. We considered that the sections of coastline from “a to g” represent the Core 2 section, while the portions of coastline from “h to n” represent Core 1. The arrows indicate the mean wind direction in the upwelling region. Only wind speed and direction located over the shallow topography ($\leqslant$ 1000 m) are selected as potential drivers of upwelling wind-driven. We then compare the direction of the wind relative to the orientation of the coast for each portion of the smoothed coastline to explain the contribution of local wind to coastal upwelling intensity. Figure 4.7 also shows the wind roses characterising the direction and intensity of the wind in the upwelling region. The orientation of each coastline portion defined above is compared with the dominant wind direction illustrated by the wind rose (Figure 4.7). The figure shows the correspondence between the dominant direction of the wind and the orientation tangent to the coastline. The results reveal that the orientation of the coastline in the south of Madagascar favours upwelling condition, especially for the sections “i, j, k, l” in Core 1 and “c, d, e, f, g” in Core 2, where the wind blows tangentially to the coastline. Figure 4.7 shows that although the coastline presents a large curve, the wind is still mostly parallel to the coastline and therefore favorable to upwelling.

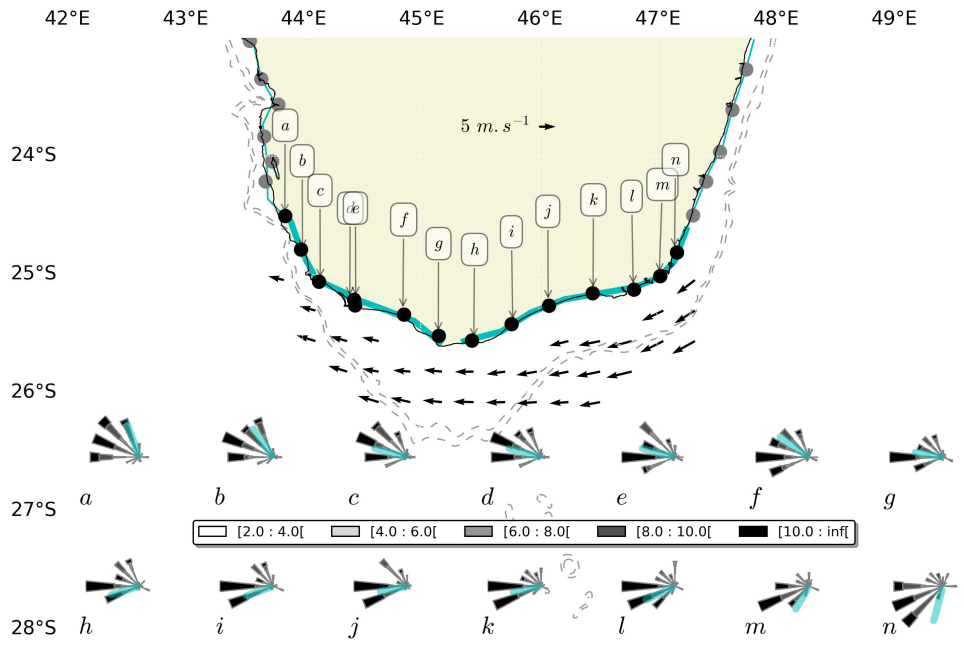

Figure 4.7: In the map "a, b,...,n" are sections of the smoothed coastline represented by the solid turquoise line; Arrows are the average wind. Wind roses are polar distribution of wind intensities and directions for each section of coastline. The turquoise solid lines in the wind roses show the orientation of the smoothed coastline.

Figure 4.8 shows the CSET calculated at different sections of coastline. The Hovmöller plot allows us to assess seasonal variations in the magnitude of the upwelling favorable winds. In agreement with Figure 4.6, high values of CSET occur during two distinct periods. The CSET is large in late winter and moderate during summer for specific sections of the coastline. The results confirm that winds are upwelling favorable in late winter (Aug-Sep) for sections "i, j, k, l" (Core 1) and sections "c, d, e, f, g" (Core 2). In winter, the intensity of the CSET is similar for Core 1 and Core 2, in spite of a wind speed reduction of approximately ~ 3 m.s^{-1} from Core 1 towards Core 2. This is due to the more favorable orientation of the coastline for Core 2. In summer, the CSET is moderately intense at the beginning of the year and decreases in late summer for both cores. The results demonstrate that the local winds promote moderate upwelling in late summer and strong upwelling in late winter. However, the winds are not well correlated with the upwelling index for either cores.

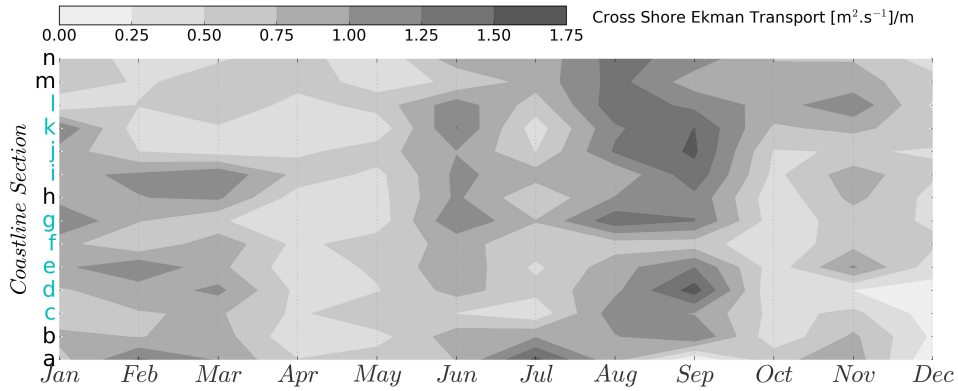

Figure 4.8: Annual variation of Cross-Shore Ekman transport ($m^2.s^{-1}$ per meter of coastline) perpendicular to the coastline sections. Tuquoise labels in y axis represent portions of coastline tangentially favourable for a wind-upwelling, where "i,j,k,l" for Core 1 and "c,d,e,f,g" for Core 2.

To further investigate the contribution of the local wind in generating upwelling, we perform idealized numerical simulations. Figure 4.9 shows that the annual mean SST from the reference simulation reproduces the coastal cold water representative of the upwelling. With weaker coastal winds, the upwelling signature is largely reduced, with SST up to 2°C warmer than in the reference experiment (Figure 4.9b). However, a patch of colder SST can still be seen inshore of the EMC, showing that the upwelling in Core 1 is also influenced by the presence of the EMC. In Core 2, the upwelling signature vanishes in the idealized experiment, thereby illustrating the greater role played by the wind as a driver of upwelling for Core 2. This result confirms that the wind is not the only mechanism at play and the interactions of currents such as the EMC interaction with the continental shelf likely plays a significant role in driving the upwelling. Next, we look at the influence of EMC on upwelling intensity.

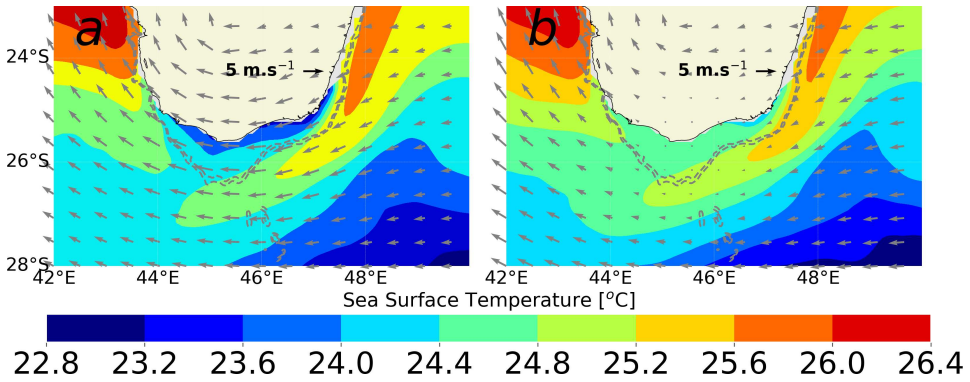

Figure 4.9: Mean SST from (a) the reference simulation, overwritten by the wind surface (arrows), and (b) the simulation with an attenuation of the wind stress above the region of upwelling. Arrows show the mean surface wind used for the simulations.

4.4.2 Influence of EMC on upwelling

Several authors have suggested that both the EMC and wind-driven upwelling act as drivers for the upwelling south of Madagascar (Lutjeharms & Machu 2000, DiMarco et al. 2000, Ho et al. 2004). Figure 4.10 presents monthly values of the upwelling index (CUI) in Core 1 and the volume transport (normalized by its standard deviation: 5.74 Sverdrups [1 Sv = 10^6 m^3 s^{-1}]) of the EMC at 23°S, upstream of the coastal upwelling over the 2.5 years period of available in-situ current observations (Ponsoni et al. 2016). A monthly Chlorophyll-a concentration time series taken in Core 1 highlights the phytoplankton response to the current forcing. Despite the relative short period of the volume transport data (28 months), the correlation between the SST upwelling index and the EMC volume transport time series is significant at 95% with a Pearson's correlation coefficient equal to 0.59. This confirms the influence of the EMC on the upwelling and explains why upwelling in Core 1 might persist despite winds not being upwelling favorable throughout the year. Modulations in the EMC transport also appears be associated with variations of the Chlorophyll-a concentration in Core 1 (correlation 0.28), although the seasonality shown in Figure 4.6 results in a minimum around January while the EMC is still strong. A very low correlation value of 0.11 between the EMC volume transport time series and the SST upwelling index for Core 2 shows that the EMC is not a direct driver of seasonal variability in Core 2. A Lagrangian experiment to investigate the sources of upwelled water in each core is used to better understand the connectivity (or lack thereof) between Core 1 and Core 2.

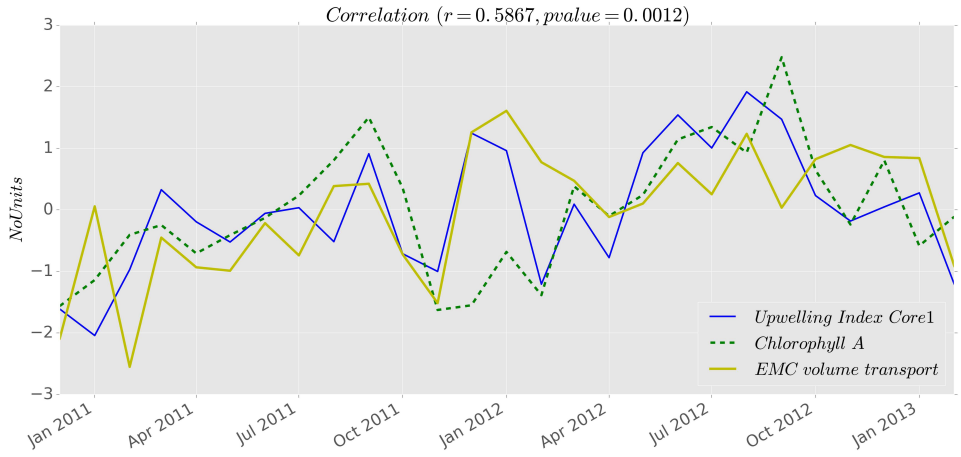

Figure 4.10: Time series coloured in blue is the coastal upwelling index inside Core 1 (normalized); Time series in yellow is the volume transport of East Madagascar Current (EMC) from ADCP transect located at 23°S (normalized). Green dash-dotted line is the Chlorophyll-a concentration inside Core 1 (normalized).

4.4.3 Origin of upwelled water

To identify the major pathways for the upwelled water of each core, we advect virtual Lagrangian particles backwards in time using the outputs of the model simulation shown in Figure 3.7. Figure 4.11 shows the horizontal density and longitudinal distribution of the origin of the particles two months before the upwelling intensity peaks in winter. The green boxes are the locations where particles are released before backward advection. The density of particles that reach Core 2 in two months is higher along the west coast of Madagascar in the Mozambique Channel, between 19°S and 26°S. The large majority of the particles [81.69 %] follow a coastal pathway along the west coast of Madagascar before reaching Core 2. A smaller proportion [18.31 %] of particles that upwell in Core 2 arrive from the East, carried by the EMC.

In contrast to Core 2, the particles upwelled in Core 1 arrive equally from both sides: 58.4 % from the EMC and 41.6 % from the Mozambique Channel. This shows that, although the EMC directly influences the upwelling in Core 1, it is not the only source of upwelled water.

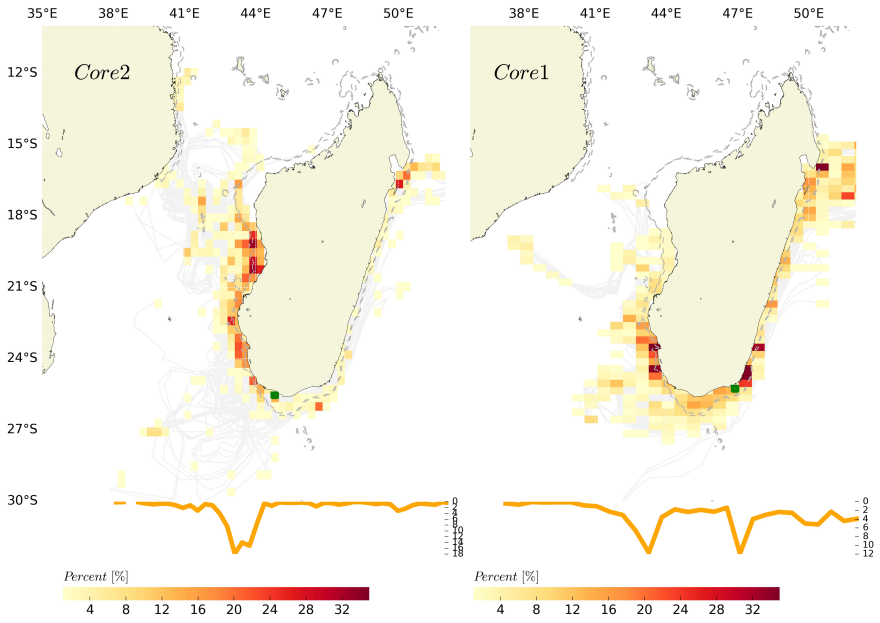

Figure 4.11: (top) Spatial probability of water parcels origin 2 months before upwelling for Core 2 (left) and Core 1 (right) during the period of 2003 to 2013. (bottom) Latitudinal average of the probability density function of particle distribution. Green boxes are the areas covered by particles at the initial position.

4.5 Discussions and conclusion

Coastal upwelling south of Madagascar occurs predominantly in two well-defined upwelling cores. The first core (Core 1) is located in the southeastern corner of Madagascar, between the coastal zone and the EMC, while the second core (Core 2) is located west of the southern tip of Madagascar. The temporal behavior of these two cores is different. Upwelling in Core 1 is perennial throughout the year with a maximum toward the end of austral winter, while weak upwelling occurs in Core 2 from October to January. These differences arise from the difference in the drivers generating coastal upwelling. Our analyses, based on satellite observations and model simulations show that upwelling in Core 1 is forced concurrently by the EMC and the wind. The significant correlation between the upwelling index and the EMC flow confirms the influence of the EMC on Core 1, in agreement with (Lutjeharms & Machu 2000, DiMarco et al. 2000, Ho et al. 2004). Ho et al. (2004) noted that the EMC strongly influences coastal upwelling along the southern Madagascan shores. Frontal variability in western boundary currents often leads to the formation of cyclonic eddies which can contribute to the promotion of upwelling

(Lee et al. 1991, Chia et al. 1982, Campos et al. 2000). The presence of such a cyclonic eddy and its potential role as a driver of upwelling was noted by Machu et al. (2002). In a recent work, Jose et al. (2016) used a coupled physical-biochemical model in the region and suppressed the momentum advection term in the Navier-Stokes equation. Jose et al. (2016) found that the coastal upwelling south of Madagascar disappears when the momentum advection (responsible for EMC detachment) is neglected in the model. Results from the model sensitivity study and the Ekman transport analysis show that the wind also drives upwelling in Core 1, in agreement with DiMarco et al. (2000). This dual forcing is suggested through the Lagrangian analysis which shows that the water particles in Core 1 arrive from both the east side, which is more induced by the EMC, and the west side from Mozambique Channel regions which is probably generated mainly by the wind. A combination of the EMC and local wind forcing appears to be at the origin of the upwelling maximum observed in winter since the EMC is slightly more intense at this time of the year (Quartly & Srokosz 2004*b*, Voldsund 2011) and the local wind is also stronger towards late winter / spring.

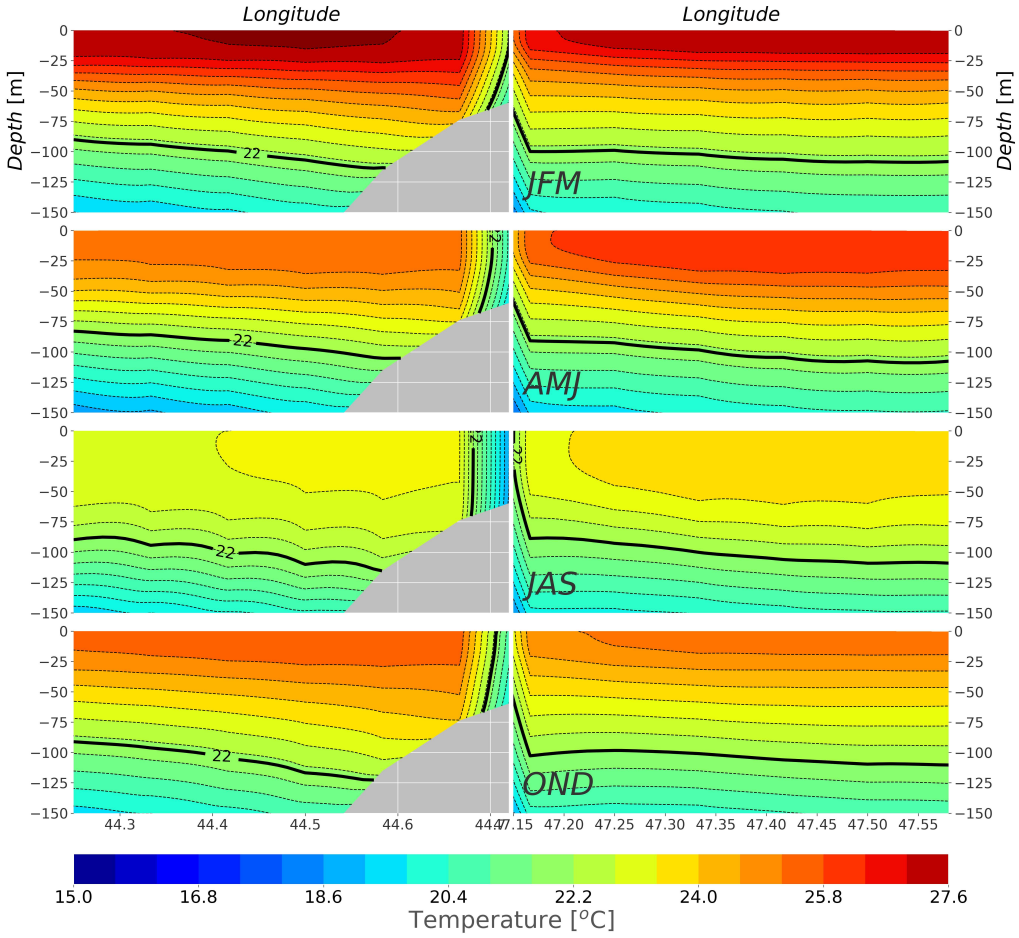

Figure 4.12: Vertical sections of temperature taken along the transect plotted in Figure 4.1b. (Left) Seasonal variations of temperature close to Core 2. (Right) Seasonal variations of temperature close to Core 1. Bold lines represent 22°C of isotherms.

An upwelling front detection reveals a second distinct upwelling region (Core 2) west of the southern tip of Madagascar. In contrast with the upwelling in Core 1, the upwelling in Core 2 is not linked with the EMC. This results in a higher SST variability for Core 2 at seasonal and inter-annual time scales. Although local coastal winds are upwelling favorable for generating Core 2, the timing of the maximum in offshore Ekman transport does not match the upwelling index maximum. The lack of correlation between upwelling and local wind was also reported by Lutjeharms & Machu (2000). Since the upwelling in Core 2 is not directly linked with the EMC, there must be other drivers of upwelling variability in this region besides the winds. The Lagrangian analysis reveals the presence of a warm poleward flow along the west coast of Madagascar, which transports water particles from warm waters of the Mozambique Channel

to Core 2. Such a warm poleward flow should result into a relatively deep thermocline along the southwestern shores of Madagascar. This is confirmed by cross sections in the realistic model simulation for each season, south-west of Madagascar (Figure 4.12 left). In contrast with the section south-east of Madagascar, where the geostrophic balance across the EMC results in an uplift of the isotherms (Figure 4.12 right), the poleward coastal flow is associated with a coastal deepening of the thermocline (represented here by the 22°C isotherm, Figure 4.12 left). In this case, although winds are upwelling favorable, warm waters are upwelled, resulting in a weak upwelling signature in SST. This situation can be compared with the California upwelling system, where a deepening in the thermocline occurs during El-Nino events (Huyer & Smith 1985). A large scale deepening of the thermocline associated with the poleward flow at the coast could be the reason why the intensity of the upwelling index becomes weaker during the summer in Core 2. DiMarco et al. (2000) have proposed that the summer upwelling is associated with the wind favorable upwelling. However, they did not exclude coastal circulation contributions.

In this study, we highlighted the presence of two separate upwelling cores south of Madagascar. The first core on the eastern side, inshore of the EMC, is associated with a dynamic upwelling driven by the detachment of the current, and upwelling favorable winds. The second core, more variable, is located west of the southern tip of Madagascar. While it is primarily forced by upwelling favorable winds, the intrusion of warm water from the Mozambique Channel may cause deviations from the seasonally wind driven upwelling cycle. The origin, nature and potential impact of warm water intrusions along the south-west shores of Madagascar are investigated in the next chapter.

Chapter 5

The South-west MAdagascar Coastal Current and the upwelling

This chapter is based on the work published as:

Ramanantsoa, J.D., Penven, P., Krug, M., Gula, J. and Rouault, M., 2018. Uncovering a New Current: The Southwest MAdagascar Coastal Current. *Geophysical Research Letters*, 45(4), pp.1930-1938. Doi: 10.1002/2017GL075900.

5.1 Introduction

The ocean circulation in the south-western Indian Ocean plays an important role in the return loop of the global overturning circulation (Gordon & Fine 1996, Talley 2013). In the south-west Indian Ocean, the South Equatorial Current separates in two branches against the east coast of Madagascar (de Ruijter et al. 2004). The northward branch, the North Madagascar Current, bifurcates again along the African continent and forms a poleward flow in the Mozambique channel dominated by large anticyclonic rings (Ullgren et al. 2012), with an estimated mean southward transport of 14 Sv (de Ruijter et al. 2002). The southward branch becomes the East Madagascar Current (EMC), transporting 20 Sv southward along the south-east coast of

Madagascar until the southern tip of the island (Ponsoni et al. 2016). Both southward flows are feeding the Agulhas Current system, contributing to the global overturning circulation. The oceanic circulation around Madagascar is currently not completely understood due to limited oceanographic campaigns and ocean dynamics studies. In a recent investigation of the upwelling structure at the southern tip of Madagascar, Chapter 4 reported that a significant amount of upwelled waters were not directly coming from the EMC but from the Mozambique Channel, following an alongshore poleward path at the south-west of Madagascar. This could be explained by the presence of a mean poleward warm surface current along the south-west coast of Madagascar, investigated in the current chapter.

Surface poleward flows along the west coasts of continents are rare in the subtropical latitudes. These include the Leeuwin Current, the Navidad Current and the Davidson Current. The Leeuwin Current is a permanent warm poleward flow along the west coast of Australia (Cresswell & Golding 1980) with a mean transport of 3.4 Sv (Feng et al. 2003). It flows against strong southerly winds, which regulate its seasonal intensities with a minimum transport in February and a maximum in June (Furue et al. 2017). The Leeuwin current also exhibits an inter-annual variability associated with El Niño-Southern Oscillation (ENSO) (Furue et al. 2017). The Navidad Current is a non-permanent warm surface current flowing northward, parallel to the shelves of Portugal and north-west Spain, and often observed during the Christmas period (Le Hénaff et al. 2011). The Davidson Current is also a non-permanent poleward surface current which is part of the California Current System along the west coast of North America (Lynn & Simpson 1987). Throughout fall and winter, the Davidson Current develops as a coastal counter current (Lynn & Simpson 1987).

In comparison to these well-documented currents, no studies have as yet revealed the existence of a poleward flow along the west coast of Madagascar in the different sketches of the surface circulation of the Indian Ocean (Schott & McCreary 2001, Schott et al. 2002, 2009). Tomczak & Godfrey (2013) even report possible events of an equatorward continuation of the EMC along the western flank of Madagascar (see their Figure 11.10). The only hint of a mean surface poleward flow west of Madagascar is that inferred from the dynamic topography map and model velocities at 46 m presented by Schott et al. (2009) (see their Figure 5 a and b).

Here, using in-situ and satellite observations as well as model data analyses, we show that a mean poleward warm surface current is present along the south-west coast of Madagascar: the South-west MAdagascar Coastal Current (SMACC). Then, we investigate the spatial extent,

transport pathways, and variability of the SMACC, and the mechanism responsible for its occurrence. The outline of the chapter is organised as follows: Subsection 5.2 details all datasets, model setup and methods used, Subsection 5.3 presents the results. Lastly, Subsection 5.4 provides an interpretation of the findings and summarises the main results.

5.2 Data, model and methods

SADCP (Shipboard Acoustics Doppler Current Profiler) current measurements were collected during four consecutive years of research cruises between 2007 and 2010 in the Mozambique Channel. SADCP data are used to confirm the direction and intensity of the flow south-west of Madagascar. Conductivity, Temperature and Depth (CTD) profiles, collected from cruises are also used to identify which water masses make up the SMACC. Details of cruise tracks are given in the Table 5.1 here below.

Table 5.1: Description of in-situ data used in this study together with the associated dates, vessels and research cruises

Data used	Code	Vessel	Cruise name	Date
SADCP	260	R.V. Antea	MESOP 2010	07-04-2010/08-05-2010
CTD	260	R.V. Fridtjof Nansen	ASCLME 2009	09-08-2009/16-08-2009
SADCP	260	R.V. Fridtjof Nansen	ASCLME 2009	09-08-2009/16-08-2009
SADCP	300	R.V. Fridtjof Nansen	ASCLME 2008	24-08-2008/07-09-2008
SADCP	340	R.V. Algoa	ACEP 2007	10-09-2007/23-09-2007

SADCP data are used to confirm the direction and intensities of the southward flow at the south west of Madagascar. Conductivity, Temperature and Depth (CTD) profiles, collected from cruises operated in the region (Table 5.1) are also used to identify which water masses make up the SMACC.

The Multi-Scale Ultra-High Resolution (MUR) sea surface temperature (SST), provided on a 0.011° spatial grid (Vazquez-Cuervo et al. 2013), is used to determine the surface signature of the SMACC.

The surface displacements from the Argo-Based Deep Displacement Dataset (ANDRO) (Ollitrault & Rannou 2013), averaged over 2 degree bins to retain enough observations, are used to compute mean surface velocities.

Trajectories of all available surface drifters encountered south-west of Madagascar are collected from the Global Drifter Programme database (http://www.aoml.noaa.gov/envids/

gld/krig/parttrk_id_temporal.php).

We used the outputs of a two way nested configuration of the Coastal and Regional Ocean Community model (CROCO) (Debreu et al. 2012, Shchepetkin & McWilliams 2005). The model was run over 1993-2014 and has a $\frac{1}{12}$ degree horizontal resolution. The model surface conditions are derived from the ERA Interim atmospheric reanalysis (Dee et al. 2011). The lateral boundary conditions are forced by the GLORYS ocean reanalysis (Ferry et al. 2012). A complete description and evaluation of the configuration are shown in Chapter 3. Lagrangian simulations are also undertaken to advect water parcels following the code described in Gula et al. (2014).

We tested the influence of the wind stress curl on the mean poleward flow using a Sverdrup relation (Sverdrup 1947) forced by the SCOW climatology of wind stress curl (Risien & Chelton 2008), as expressed here below:

$$v = \frac{\mathbf{k}.\nabla \times \tau}{H_0 \, \beta \, \rho_0} \tag{5.1}$$

where v is the meridional velocity in a surface layer of depth H_0 (m), $\mathbf{k}$ is the unit vector in the vertical direction, β is the meridional gradient of the Coriolis parameter, ρ_o is the mean water density (1025 kg m^{-3}), τ (N m^{-2}) is the wind stress. Results are compared with the mean circulation computed from the CROCO model outputs averaged over the same depth (H_o).

5.3 Results

5.3.1 Horizontal structure of the SMACC

A significant amount of upwelled water south of Madagascar is coming from the Mozambique Channel (Figure 5.1a). Based on the result found in Chapter 4, the backtracking Lagrangian particles analyses revealed that 81 % of particles followed consistent pathways along the south-west coast of Madagascar before reaching the upwelling cell, while 19 % arrived from the EMC. This suggests the presence of a mean poleward current along the south-west coast of Madagascar, the SMACC.

The SMACC is present in the model and observations (Figure 5.1c and Figure 5.1d). Its signature is visible in SST as a warm tongue of water extending southward along the coast. The warm tongue starts in the vicinity of 22°S in the north and extends southward to 25.5°S.

The average surface temperature of this warm flow ranges from 27.2°C upstream to 25.1°C downstream. This water appears to originate from the warm surface waters present in the Mozambique Channel further north (Halo et al. 2014). The downstream temperature is cooler, probably as a result of air sea interactions and/or mixing with colder upwelled coastal water and waters pumped by cyclonic eddies south of Madagascar (Ridderinkhof et al. 2013).

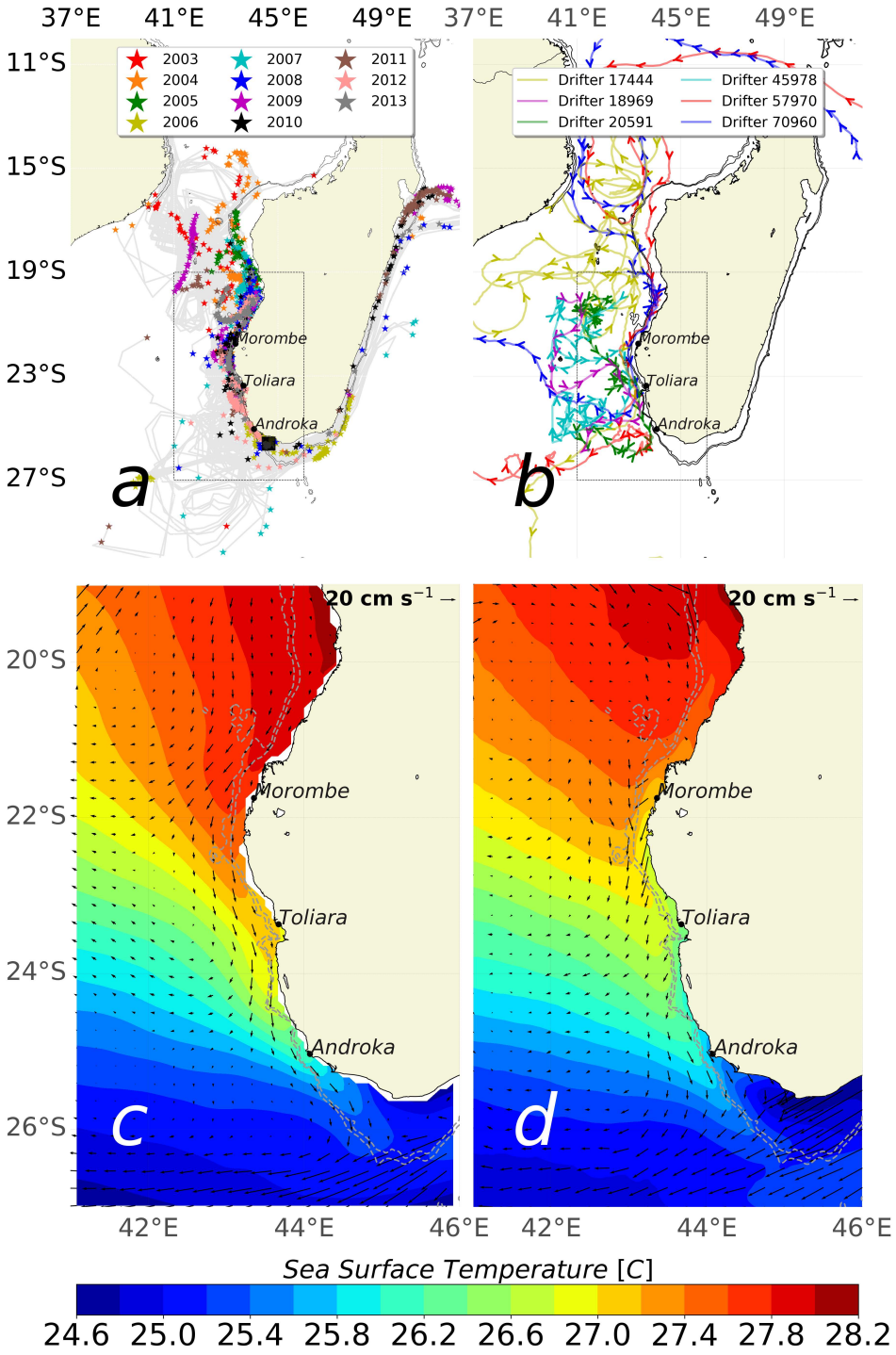

Figure 5.1: a- Inter-annual distribution of origin (small stars) and tracks (grey lines) of Lagrangian particles seeded in the upwelling cell south of Madagascar (box in black) and backtracked for 2 months, over the period of 2003-2013. The dotted rectangle shows the region of interest, south-west of Madagascar. Dashed lines show 500 m and 1000 m isobaths. b- Trajectories of all available surface drifters within the Global Drifter Programme database (Lumpkin & Pazos 2007) passing in the south-west of Madagascar. c- Mean SST and surface currents (arrows) from the model over the period 1993-2013. d- Mean SST from MUR satellite product over 2003-2015 and mean surface currents (arrows) derived from ANDRO surface displacements covering the period from 1995 to 2016 (Ollitrault & Rannou 2013).

Mean observed currents derived from the ARGO floats surface displacement (ANDRO) (Ollitrault & Rannou 2013) show a clear alongshore southward flow toward the southern tip of Madagascar. Trajectories of all available drifters extracted from the Global Drifter Programme database (Lumpkin & Pazos 2007) passing in the region of the SMACC also show directions and pathways consistent with the presence of the SMACC (Figure 5.1b). Chronologies of these drifters are recapitulated in Table 5.2 here below.

Table 5.2: Time periods corresponding to drifters passing the SMACC region, through the rectangle in Figure 5.1 (lat: 19°S - 27°S ; lon: 41°E - 46°E)

Number of drifter	Period
Drifter 17444	03/01/2001 - 02/02/2001
Drifter 18969	24/11/1997 - 15/02/1998
Drifter 20591	13/09/2002 - 17/02/2003
Drifter 45978	16/09/2005 - 15/12/2005
Drifter 57970	10/01/2007 - 03/03/2007
Drifter 70960	05/03/2009 - 31/03/2009

Figure 5.2 shows geostrophic velocities derived from 4 different mean dynamic topographies RIO 2005 (Rio & Hernandez 2004), CLS 2009 (Rio et al. 2011), CLS 2013 (Rio et al. 2014) and Maximenko 2015 (Maximenko et al. 2009), and the ARGO-based surface mean displacement (Ollitrault & Rannou 2013). Although similarities can be found between the different mean circulations, some disparities are observed in our region of interest. The structure of the SMACC is clearly defined in CLS 2009, Maximenko 2015 and the ARGO float displacement (ANDRO) datasets. Velocities derived from CLS 2009, Maximenko 2015 and ANDRO appear to be relatively similar. All products depict a poleward flow along the south-west coast of Madagascar. Velocities derived from RIO 2005 and CLS 2009 show a weak poleward current along the coast of Madagascar south of 25°S, but do not resolve any current north of 25°S.

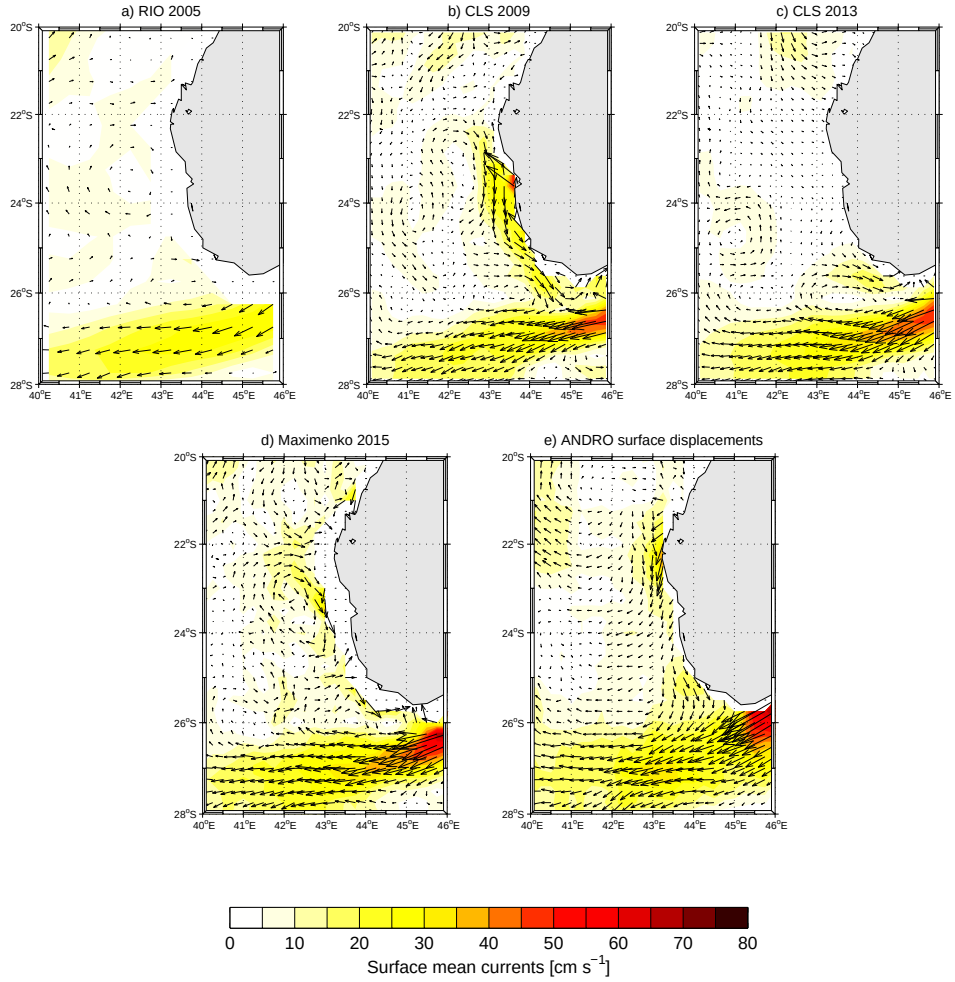

Figure 5.2: Mean geostrophic currents derived from different mean dynamic topographies: RIO-2005 a- (Rio & Hernandez 2004), CLS-2009 b- (Rio et al. 2011), CLS-2013 c- (Rio et al. 2014), d- (Maximenko et al. 2009), and from ARGO floats surface displacement f- (Ollitrault & Rannou 2013).

Mean geostrophic currents derived from different mean dynamic topography products also hint to the presence of the SMACC, albeit with differences in their representation of the current close to the coast.

The model highlights a contribution to the SMACC coming from the north (Figure 5.1c), which is less evident in observations. This difference can also be noticed in the model SSTs (Figure 5.1c) which are slightly higher than remotely sensed SSTs between 19°S and 22°S (Figure 5.1d). However, both model and satellite observations are in agreement from 22°S to 25°S and show an alongshore propagation of the SMACC. The SMACC has averaged surface speeds between 20 cm s^{-1} and 30 cm s^{-1}. Based on the warm tongue and currents vectors

plotted in Figure 5.1c, 5.1d, the SMACC is approximately 500 km long with a width less than 100 km.

The presence of the SMACC is confirmed by the near surface current measurements collected from SADCPs at 20 m depth (uppermost data measured) during different cruises (Figure 5.3). The first two SADCP transects *a*, *b* were made in 2007 and indicate a broad southward surface current. The sea surface height contours taken at the same time show that the strong southward currents visible offshore (more than 50 km from the shelf) at transects *a* and *b* are due to the presence of a cyclone on the west and an anticyclone on the south-east. A local jet-like signature corresponding to the SMACC can be seen off the shelf edge within 50 km from the coast (see red arrows in Figure 5.3). Geostrophic velocities derived from the sea surface height of Figure 5.3 do not show any current close to the coast (not shown). The SADCP transect *c* was collected in 2008 (Figure 5.3). Transect *c* also depicts a southward flow off the shelf edge. The velocity maximum about 80 km away from the shelf corresponds to the currents associated with a cyclonic eddy. The signature of the SMACC is visible as a weaker southward flow ($\approx$ 15 cm s^{-1}) over the shelf. The SADCP transects *d*, *e*, *f* and *g* were made in 2009. They show a southward flow within 50 km from the coast with an averaged velocity of 30 cm s^{1}. While these SADCP sections only provide a few snapshots of the circulation, which do not necessarily correspond to the mean circulation, they still provide growing evidence of the existence of the SMACC.

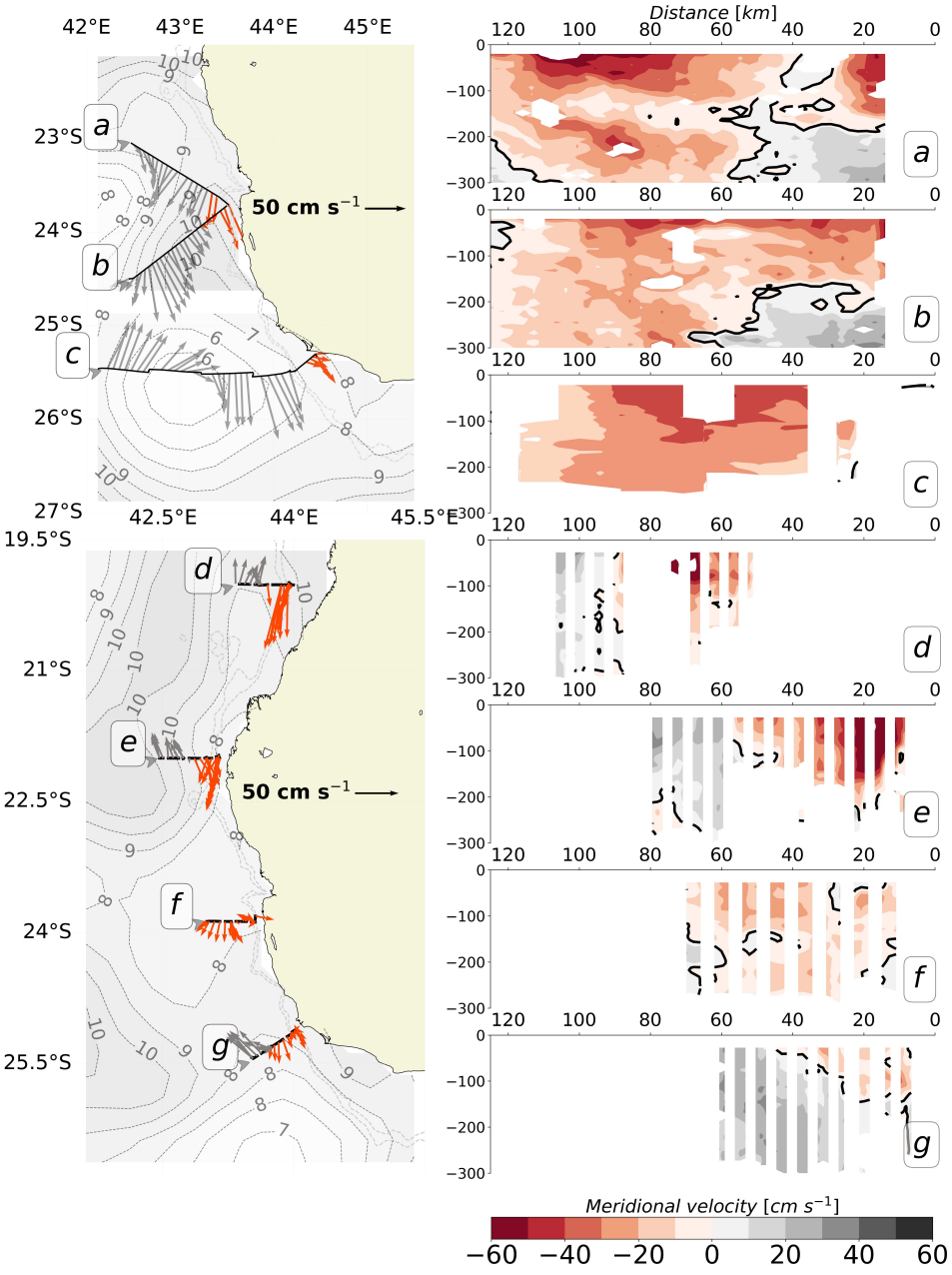

Figure 5.3: Top left column: Transects of Shipboard ADCP (SADCP) collected during ACEP 2007 oceanographic cruises (Table 5.1). Transects *a* and *b* were collected on 13 - 14/09/2007 on board the R.V. Algoa; *c* was collected on 26 - 28/09/2008 during ASCLME 2008 cruise on board the R.V. Fridtjof Nansen. Arrows show the direction and intensities of the measured near surface currents (20 m) for *a*, *b* while *c* is represented from the existing data closest to the surface. Red arrows represent the SMACC. Contours depict CLS AVISO sea surface height for the period of each cruise and at the same date. Bottom left column: Transect *d*, *e*, *f* and *g* show Shipboard ADCP (SADCP) collected during ASCLME 2009 cruise on board the R.V. Fridtjof Nansen from 26/09/2009 to 04/09/2009 (see Table 5.1). Right column: Vertical sections of meridional velocities (cm s^{-1}) across the transects. The 0 values are represented by the black contours and the missing values by blank patches. The x-axis refers to the offshore distance [km] from the coast.

5.3.2 Vertical structure of the SMACC

Modelled vertical cross-sections of the time-averaged flow across transects *d*, *e*, *f* and *g* are presented in Figure 5.4 (left) to characterise the vertical structure of the SMACC. At transect *d* (20.4°S), the SMACC consists in a weak poleward flow extending from the surface to 150 m depth and from the coast to 100 km offshore. Further south, along transects *e* (22°S) and *f* (23.7°S), the SMACC is deeper with larger velocities. The SMACC is most intense near transect *f*, with velocities reaching 25 cm s^{-1}. Between transects *f* and *g*, the SMACC decreases in strength and becomes shallower. Observed vertical structure at transect *e* and *f* (Figure 5.3) corroborates with the vertical cross-sections from the model. At transect *g* the observed flow is weaker and shallower in agreement with the modelled sections. Furthermore, an equator-ward undercurrent is visible below the SMACC in the model and observations along this transect (Figure 5.3g).

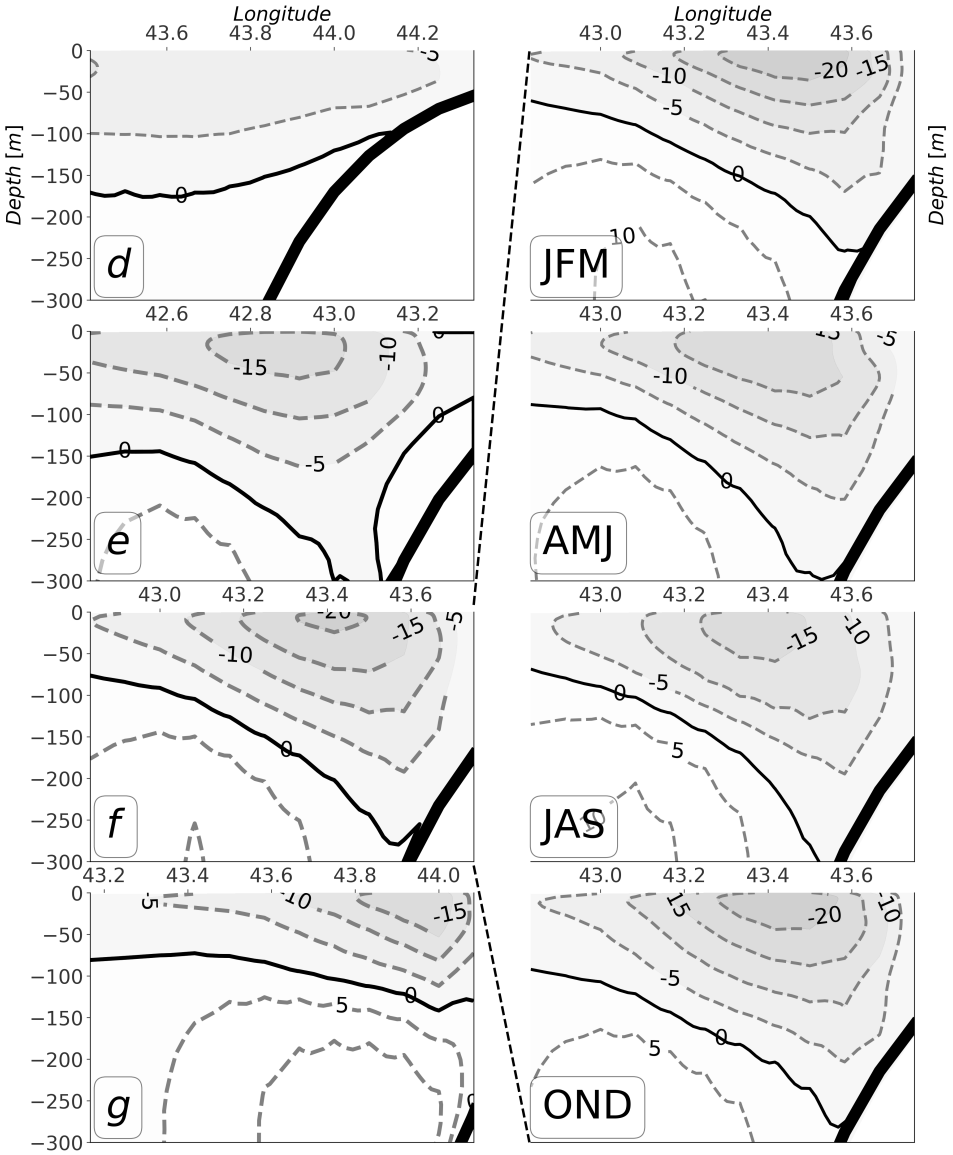

Figure 5.4: Left column: Vertical cross-sections of annual mean modelled northward velocities (cm s^{-1}) in the SMACC across transects *d* to *g* shown in Figure 2. Negative speeds indicate a southward flow associated with the SMACC. Right column: Seasonal variations of mean northward velocities (cm s^{-1}) accross transect *f*.

The location where the SMACC velocities are maximum, near transect *f*, is selected to illustrate seasonal variations in the SMACC meridional velocities (Figure 5.4). While the width and depth of the SMACC do not significantly change throughout the year, the SMACC is stronger in summer (OND-JFM) than in winter (AMJ-JAS). Maximum current velocities in the SMACC of about 20 cm s^{-1} and 25 cm s^{-1} in OND and JFM are reduced to 10 cm s^{-1} and 15 cm s^{-1} in AMJ and JAS. The annual volume transport across this transect is 1.3 Sv (10^6 m^3s^{-1}) with seasonal maxima of 1.6 Sv and 2.1 Sv during the warm season (OND and JFM) and minima of 0.9 Sv and 0.7 Sv during the cool season (AMJ and JAS). Transports were calculated across Transect *f* (Figure 5.3), integrated horizontally between 43°E and 43.7°E and down to 250 m depth. Frequent occurrences of eddies south of Madagascar result in a large variability of the SMACC (Figure 5.7 bottom), as seen also during the ASCLME 2008 cruise (Figure 5.3).

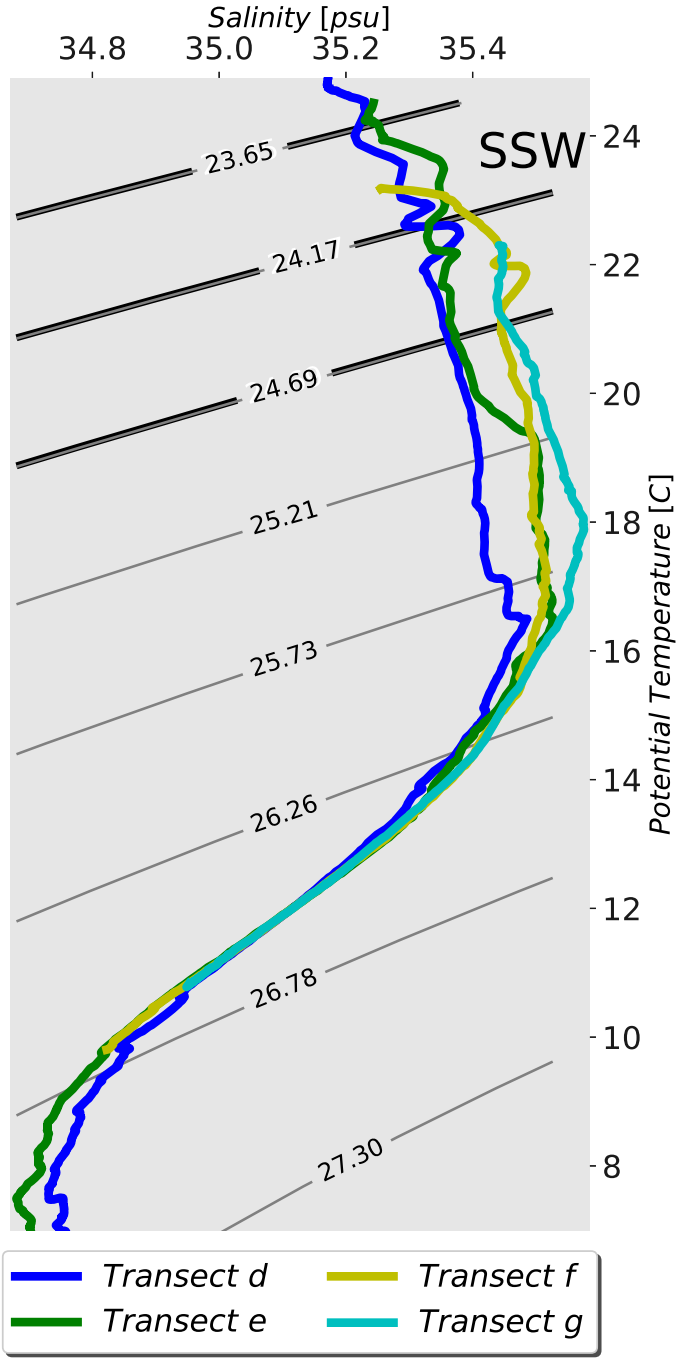

Figure 5.5: Temperature-Salinity (TS) diagram from conductivity, temperature, and depth measurements collected as part of the ASCLME cruise of 2009 (Table 5.1) and along the transects shown in Figure 5.3. Bold solid lines highlight the range of potential densities associated with the SMACC.

Temperature and salinity (TS) diagrams (Figure 5.5), from vertical profiles using CTD data collected during 4 transects in 2009 (Table 5.1), show that water properties of the SMACC correspond to Subtropical Surface Waters (SSW) (Donguy & Piton 1969, Wyrtki 1971, Sætre & Da Silva 1984).

5.3.3 Forcing of the SMACC

To address the physical process generating the SMACC, we compare mean meridional velocities from the model with predictions from the Sverdrup relation 5.1 in Figure 5.6. Both velocities have in common a region of poleward flow along the western Madagascan coastline with meridional velocities higher than 8 cm s^{-1}. The lack of QuikSCAT observations near the coast due to land contamination prevents us from computing the Sverdrup circulation there, but the patterns are fairly similar between the model solution and this simple relationship. The bending of the trade winds around the southern tip of Madagascar results in a large cyclonic wind stress curl (especially in January, see the Figure 6 by Risien & Chelton (2008)), forcing a poleward flowing surface current.

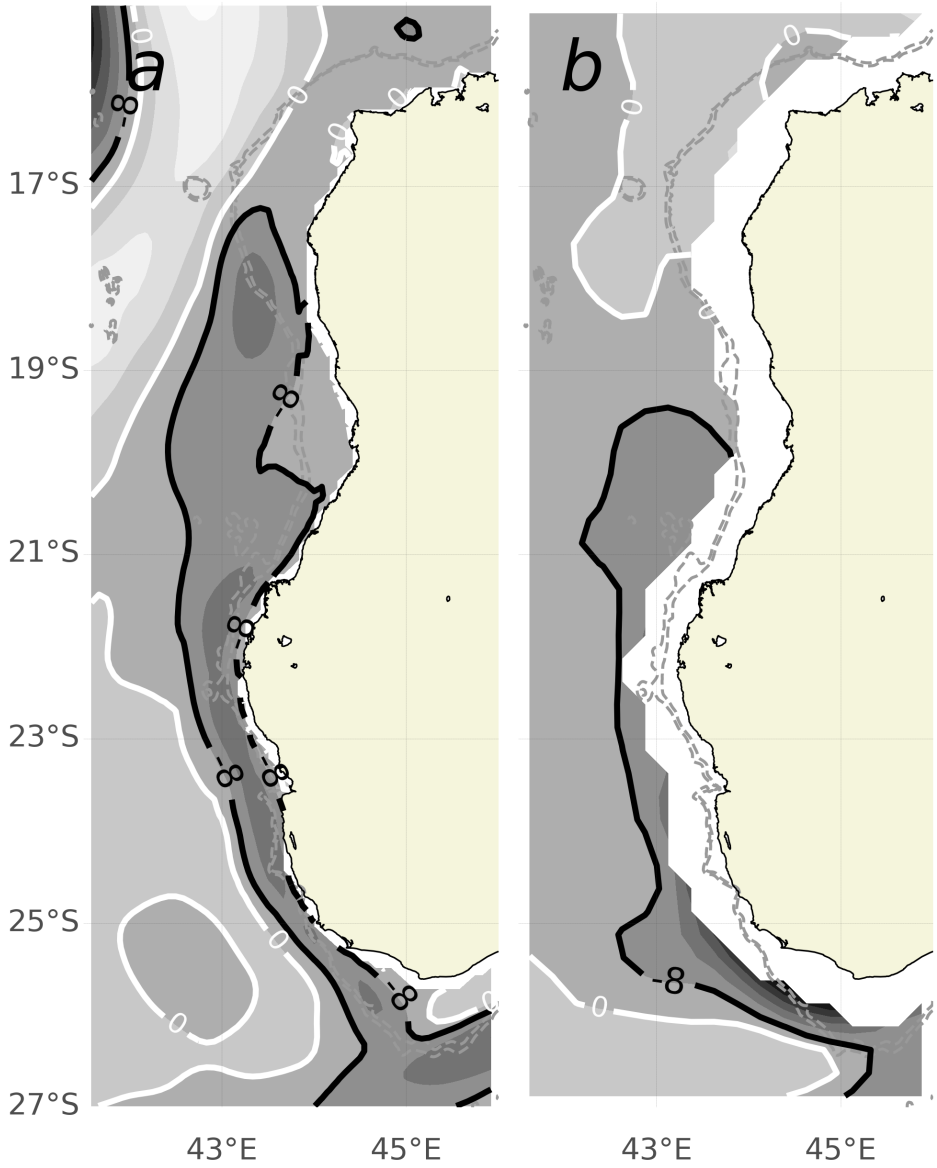

Figure 5.6: Forcing of the SMACC: (a) Contour plots of meridional velocities averaged over the upper 50 m of the CROCO model outputs and (b) meridional velocities calculated from the Sverdrup relation and using QuikSCAT winds. Labels on the contour line show the magnitude of the meridional velocities in (cm s^{-1}) with darker shades of grey marking regions of increasing meridional velocities.

5.4 Discussions and Conclusion

Cruise datasets, satellite observations and analyses of a model output are exploited to reveal the existence of a warm coastal current with a volume transport comparable to that of the Leeuwin current (Furue et al. 2017): the SMACC. The SMACC is a poleward current which flows along the south-western shores of Madagascar. It flows from 22°S to the southern-most part of the island near 26°S. The average length of the SMACC is about 500 km and its average width is between 50 and 100 km. The SMACC is a warm surface current, which extends over the upper 150 m of the water column upstream and becomes shallower (around 70 m) downstream. The water masses of the SMACC have high salinities characteristic of Subtropical Surface Waters. The average surface speed is around 20 cm s^{-1} with an enhancement in the vicinity of Toliara at around 23.5°S (transect f on Figure 5.4). The average volume transport is 1.3 Sv. The SMACC exhibits a seasonal variability with more intense velocities during the warm season (OND-JFM) and a weakening during the cool season (AMJ-JOS). The mechanism driving the SMACC can be explained by Sverdrup dynamics forced by cyclonic wind stress curl induced by the bending of the trade winds. The intensity of this surface current is highly related to the magnitude of the winds. The core of the SMACC is intensified at 24°S due to the enhancement of the wind stress curl south west of Madagascar. In addition, cyclonic eddies generated at the south of Madagascar (Halo et al. 2014) could also contribute to the intensification of the southern part of the SMACC (as seen during the ASCLME 2008 cruise, Figure 5.3).

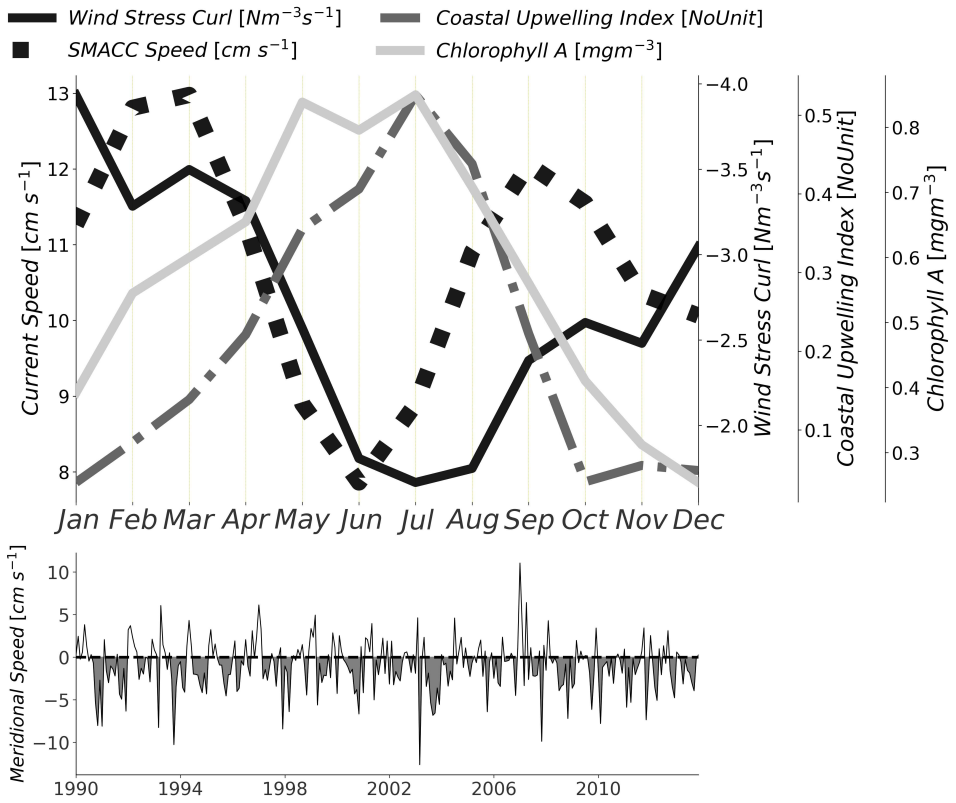

Figure 5.7: Top: Annual variations of wind stress curl (N m^{-3}s^{-1}) (black solid line), SMACC's surface speed (cm s^{-1}) (dashed black line), coastal upwelling index (dashed grey line) and Chlorophyll-*a* concentration (mg m^{-3}) for the upwelling cell. Bottom: time series of modelled meridional velocities averaged over the first 150 m, representing the SMACC across transect *f*.

The upwelling-related processes in the south of Madagascar are influenced by the SMACC, as highlighted by virtual particles Lagrangian simulations (Figure 5.1a). Intensification of wind stress curl could also favour the intrusion of the SMACC toward the upwelling system. Chapter 4 pointed out that the intrusion of warm waters from the Mozambique Channel could reduce the upwelling surface signature during summer. Figure 5.7 shows that the annual cycle of the upwelling index (CUI) defined in Chapter 4 is anticorrelated with the wind stress curl and the SMACC surface speed. This suggests that the intensification of the wind stress curl enhances the SMACC, which brings warm water, reduces the surface signature of the upwelling south of Madagascar, and influences the phytoplankton response associated with the upwelling.

SADCP observations also show the presence of a countercurrent (equatorward) below the SMACC (below 300 m depth) between 24.5°S and 25.5°S (Figure 5.8). Figure 5.3 and 5.4 provides evidence of this undercurrent, seen in observations and model solutions.

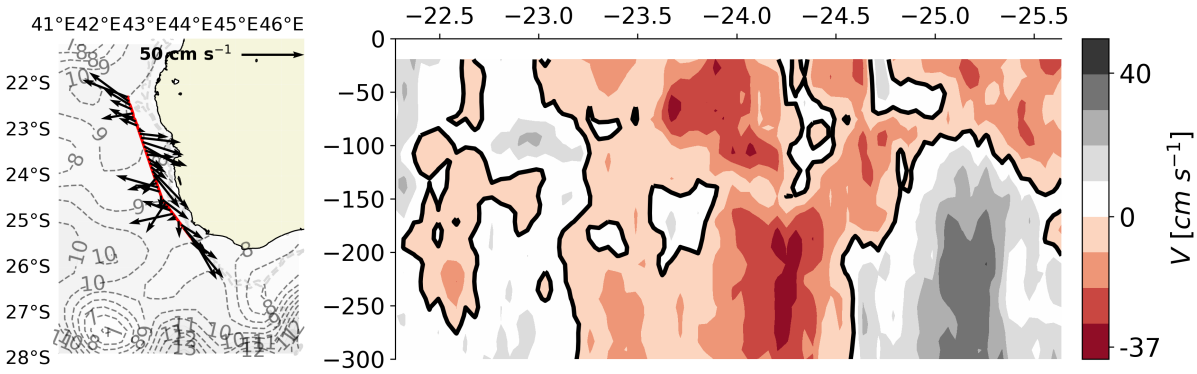

Figure 5.8: (left) Arrows are surface current directions and intensities measured using Ship-board mounted ADCP during the MESOP 2010 research cruise (Table 5.1). Contours are sea surface height from CLS AVISO averaged during the transect period from 05/05/2010 to 07/05/2010. (right) Vertical section of meridional velocity from the cruise transect shown in the left panel. Black lines represent the zero contour for the meridional velocities.

Uncovering the existence of the SMACC brings new understanding for biological and fisheries related management, which is an important socio-economic component (Pripp et al. 2014, Bemiasa 2009). Knowledge of the pathway of the SMACC will improve our understanding of the coastal connectivity and lead to better fisheries and ecosystem management. This introduces a prominent process affecting the diffusion and distribution of biological species (Shrimp, lobster, small pelagic fish, mangrove, etc.) that will need to be taken into account for the management and emplacement of an eventual marine protected zone.

? have also addressed the contribution of the south-west of Madagascar waters to the regional circulation. They highlighted a long-term exchange between the southern Mozambique Channel off Toliara (Figure 5.1), and the Agulhas Current core. They found a correlation between coral records and the Agulhas SST reconstruction for the past 334 years, showing a link between the transport of warm water from south-west of Madagascar and the Agulhas current. The SMACC could be instrumental in explaining this link.

Chapter 6

Linking inter-annual upwelling variability and currents

6.1 Introduction

Previous Chapters of this study (Chapter 4, 5) have explained that the coastal upwelling south of Madagascar is subjected to multiple forcing affecting the strength of the upwelling cells defined as Core 1 and Core 2. Based on a seasonal variability study (Chapter 4), Core 1 is primarily forced by the East Madagascar Current (EMC) but reinforced by wind-driven upwelling, while the Core 2 is predominantly forced by the along-shelf wind stress but also influenced by the South-west Madagascar Coastal Current (SMACC) (Chapter 5). Although the ocean currents influence predominantly the upwelling, seasonality of the upwelling is forced predominantly the upwelling by the winds. We expect that inter-annual variations in the upwelling will be driven mostly by the ocean currents with a remaining influence of the wind stress. The understanding of the upwelling inter-annual variability will require a thorough knowledge of the origins and mechanisms regulating the EMC and SMACC. In addition,the EMC and the SMACC are connected to the large scale circulation in the south-west Indian Ocean (Wyrtki 1973, Nauw et al. 2008, Palastanga et al. 2006) and there is a possibility that they are impacted by climate mode oscillations (Yamagata et al. 2004), such as El-Niño Southern Oscillation (ENSO), Indian Ocean Dipole (IOD), and Subtropical Indian Ocean Dipole (SIOD).

While we have established in Chapter 4 and 5 that EMC and the SMACC are strong drivers

influencing the coastal upwelling, little is known about their inter-annual variability. Characterising the variability of the EMC and SMACC, including their respective forcing, should explain the inter-annual variability of the upwelling in Core 1 and Core 2.

Very limited literature addressed the inter-annual occurrence of the upwelling and ocean currents south of Madagascar. Ho et al. (2004) investigated inter-annual variations of the Chlorophyll-a concentration using Ocean Colour satellite product. Ho et al. (2004) found that winter 1999 and summer 2001 were associated with abnormally low levels of Chlorophyll-a concentration. This contribution is important but we don't know yet if it was applicable for upwelling cells, Core 1 and Core 2. The analysis of Ho et al. (2004) only looked at Chlorophyll-a concentration and might not reflect all of the processes linked to the upwelling variability. Inter-annual variability of the upwelling still remains unclear and the global climate oscillation effects upon the upwelling are still unknown.

This chapter seeks to provide understanding of the inter-annual variability of the coastal upwelling south of Madagascar and to identify the possible causes of changes at inter-annually time scale. For that purpose, we will use satellite observations and ocean numerical model. Based on Chapter 4 and Chapter 5, the upwelling is strongly influenced by EMC and SMACC. Identifying the inter-annual variability of the EMC and SMACC could be a clue to understand the inter-annual variability of the coastal upwelling. Possible teleconnection with regional and/or global climate oscillation could also explain the inter-annual upwelling-related changes over the last 35 years.

This work is outlined as follows: section 2 describes the data, ocean model and methods used, section 3 describes the results and section 4 discusses and summarises the main findings of this study.

6.2 Data, model and methods

The study used the model output described in Chapter 4. The model is a two way nested configuration of the Coastal and Regional Ocean Community model (CROCO) (Debreu et al. 2012, Shchepetkin & McWilliams 2005). The model output has a $\frac{1}{12}$ degree horizontal resolution and covers the period from 1993 to 2013. A complete description and evaluation of the configuration is provided in Chapter 3 and 4 (Figure 3.8, 3.7, 5.2, A.6).

In this study, we use the upwelling index computed in Chapter 4 (Equation 4.2) which

measures the surface temperature signature induced by the upwelling. This upwelling index is used to investigate the inter-annual variability of upwelling intensity. A 35 year long time-series of the upwelling index is built by combining the 4km AVHRR-Pathfinder SST (Version 5.0) available over the 1981-2009 period (Casey et al. 2010) to the MUR SST which is available on a 1km resolution grid and over the 2003-2017 period (Figure 3.4, A.1). The purpose of extending the SST upwelling index was to better resolve inter-annual variability in the upwelling cells of Core 1 and Core 2.

The upwelling index is compared with the El Niño-Southern Oscillation (ENSO), the Indian Ocean Dipole (IOD) and the Subtropical Indian Ocean Dipole (SIOD) indices. The monthly means of the NINO3.4, Indian Ocean Dipole index (Dipole Mode Index) and Subtropical Indian Ocean Dipole index time series are collected from KNMI Climate Explorer (`http://climexp.knmi.nl/data/`). The IOD index is calculated from SST anomaly difference between the west (50°E to 70°E and 10°S to 10°N) and eastern (90°E to 110°E and 10°S to 0°N) of the Indian ocean (Ashok, Chan, Motoi & Yamagata 2004). The SIOD Index is the difference in SST anomaly between a western region located south of Madagascar (55°E to 65°E, 37°S to 27°S) and an eastern region in the vicinity of Australia (90°E to 100°E,28°S to 18°S) at the tropical level (Behera & Yamagata 2001). The ENSO index (NINO3.4) is based on SST anomalies captured from the Niño Region 3.4, bounded by 120°W to 170°W and 5°S to 5°N (Trenberth 1997).

Figure 6.1a shows the mean ocean circulation east of Madagascar where the South Equatorial Current (SEC) bifurcates and its southern branch, the EMC, propagates southward along the Madagascan coast (Chapman et al. 2003, Ponsoni et al. 2016). Based on Chen et al. (2014), we consider that changes in the SEC strength and bifurcation location could impact the EMC. Therefore, we conduct an analysis to measure the SEC bifurcation position. The SEC bifurcation position is the latitudinal position of the meridional velocity equal to zero during separation between the northward and southward branches, integrated over the first 1000 m depth (Figure 6.1b), along the coast between 13°S and 20°S (Figure 6.1a) at the 51°E.

The mean offshore extent of the EMC is also considered to characterise the width of the current. We measure the position of the border limit of the EMC at 22°S represented by the bold line in Figure 6.1c. The longitudinal mean offshore extent is integrated over the 1000 m and averaged yearly during the period of 1993 to 2013.

The integrated volume transport is also calculated at 22°S over the first 1000 m depth.

With the view to measure the bottom Ekman transport which can lead the upwelling in Core 1, the cross-shore transport in the near bottom layer is estimated using the along-shore bottom stress according to Ekman et al. (1905).

$$\tau_b = \rho_o C_d \sqrt{u_b^2 + v_b^2} \tag{6.1}$$

$$Ek_b = -\frac{\tau_b}{f} \tag{6.2}$$

Equation 6.1 is the linear bottom stress (τ_b) formula. Where, u_b, v_b are current velocity near bottom floor, C_d is the drag coefficient with $C_d = 0.001$ based on Perlin et al. (2005), with the similar study in Schaeffer et al. (2014). In equation 6.2, Ek_b is the approximation of the Ekman dynamic associated with the along-shore bottom stress τ_b, divided by the Coriolis term f.

The bottom Ekman transport is averaged over the polygon surrounding the high bottom stress in vicinity of 24.5°S (Figure 6.1c). The bottom Ekman transport is computed using the model solution velocity component.

The study also investigates the inter-annual variations of the SMACC characteristics and link with the upwelling cell Core 2. The volume transport of the SMACC at 25°S (Figure 6.2a in green), integrated over the 100 m depth, is computed for measuring the inter-annual connection between the SMACC southern extension flux and the upwelling index in Core 2. Figure 6.2b shows the vertical section of the meridional velocity representing the southern extension of the SMACC at the 25°S transect. The mean depth of the SMACC is measured from the mean depth zero meridional velocity contour (0 cm s^{-1}), between 43.4°S and 43.75°S represented in bold line at the Figure 6.2b. The inter-annual oscillation of the mean depth of the SMACC is used to characterise its vertical position over years.

The eastward (u) and northward (v) components of the 10 m winds from the reanalysis Drakkar Forcing Set 5.2 (DFS5.2) (Dussin et al. 2016), are used to compute the wind stress over the 1985-2015 period which has a 0.7° grid spatial resolution. The reanalysis DFS5.2 wind data is chosen because of the long period of recorded data suitable for investigating inter-annual variability, and DFS5.2 is the most recent atmospheric reanalysis which improves on ERA-interim (Dussin et al. 2016). The wind data is used to calculate the curl of the surface wind stress, $\tau_{curl} = \delta\tau_v/\delta x - \delta\tau_u/\delta y$ (with eastward surface stress (τ_u) and northward surface stress

(τ_v), in the rectangle area selected in Figure 6.2.

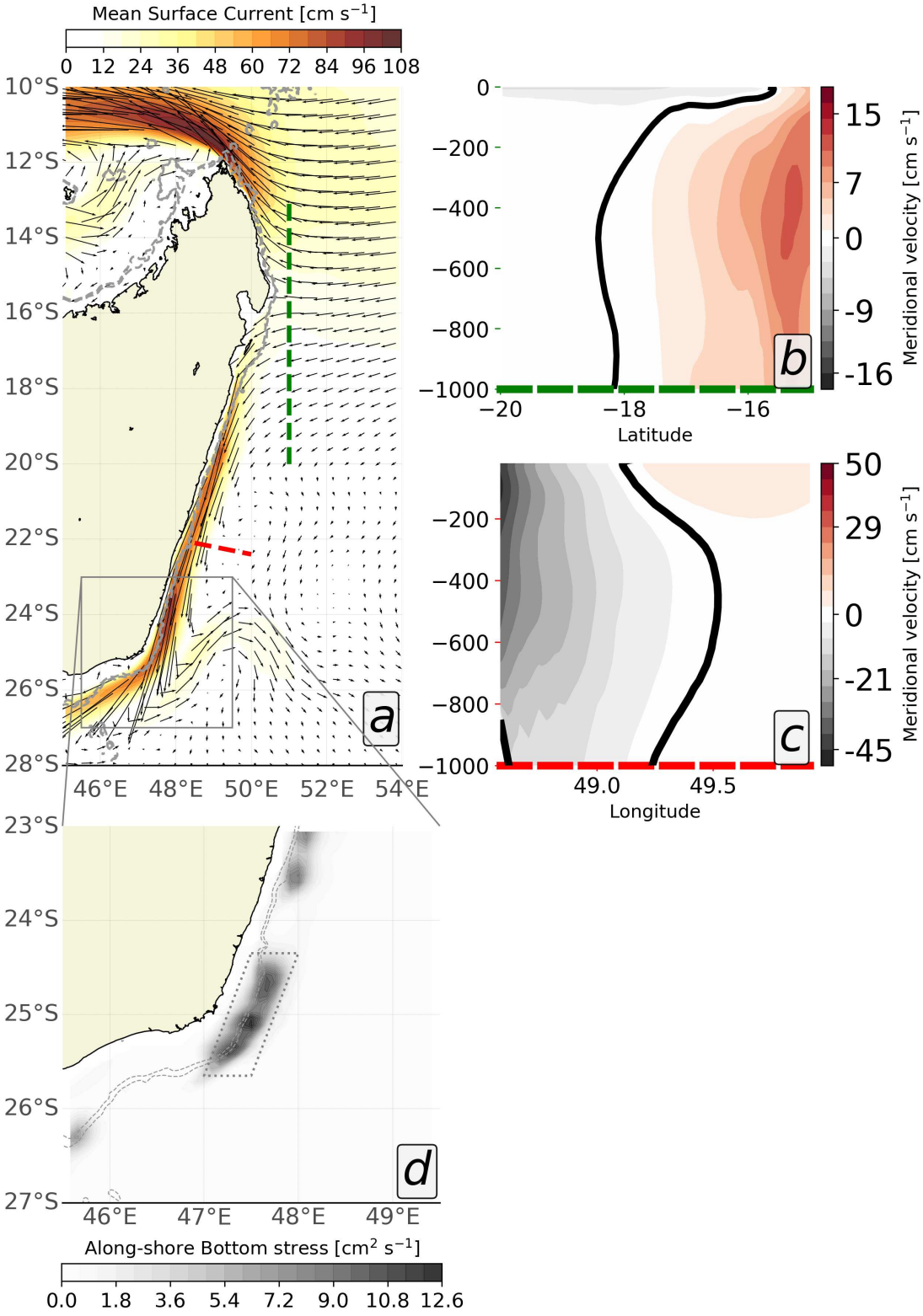

Figure 6.1: a- Mean geostrophic surface current (cm s^{-1}) derived from the model solution showing the SEC and EMC. b- Vertical section of the mean meridional velocity (cm s^{-1}) taken at the green transect in (a). Bold line is the South Equatorial Current bifurcation. c- Vertical section of the mean meridional velocity (cm s^{-1}) taken at the red transect in (a). Bold line indicates the limit position of the EMC at latitude 22°S. d- Near bottom stress of the velocity (cm^2 s^{-1}) using the model solution. Polygon in dotted-line contours the potential shelf-edge upwelling.

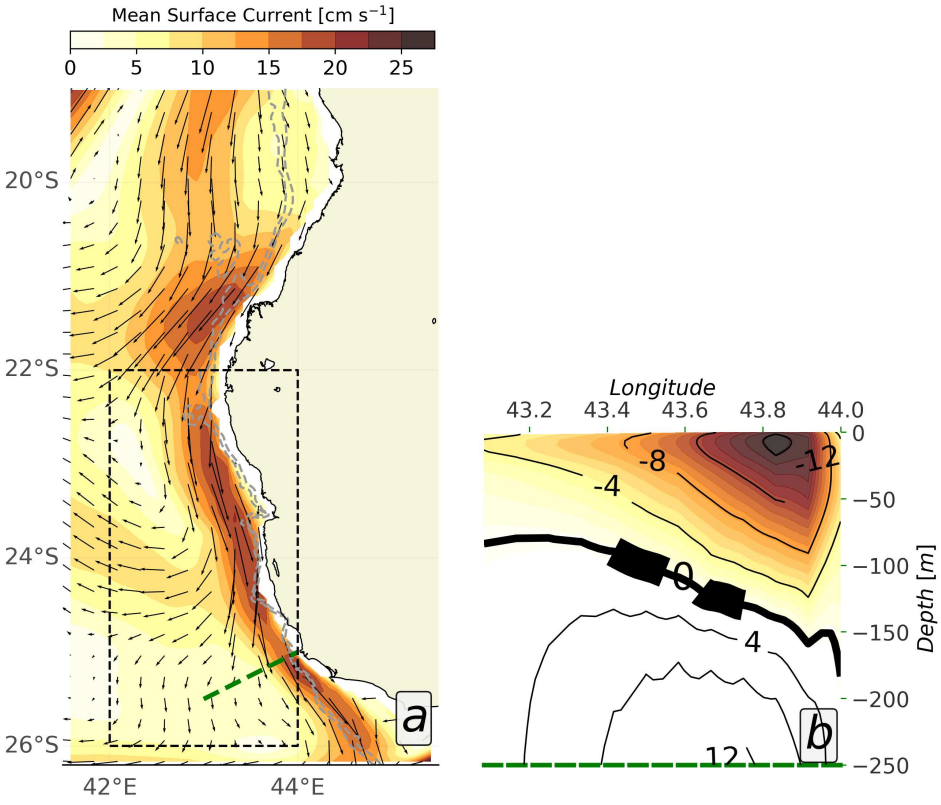

Figure 6.2: a- Mean geostrophic surface current (cm s^{-1}) derived from the model solution showing the SMACC. The rectangle is the area selected to calculate the wind stress curl. b-Vertical section of the meridional velocity (cm s^{-1}) at the southern extension of the SMACC at 25°S (Dotted line coloured in green). Contours are every 2 cm s^{-1}. Black bold line at zero isoline indicates the section measured for representing the depth (m) of SMACC between 43.4°E and 43.7°E.

6.3 Results

6.3.1 Inter-annual variation of the upwelling

The yearly average of the upwelling index is computed over the 1982 to 2016 period. Figure 6.3 illustrates the inter-annual variation of the anomalous upwelling index in Core 1 and Core 2. The seasonality dominating the upwelling (seen in Chapter 4) was removed to detect the exceptional occurrence of the upwelling at inter-annual time-scale.

In Figure 6.3a, the standard deviation of upwelling index anomaly in Core 1 reaches 0.06 which is represented by the dotted-lines. The upwelling inter-annual intensities are categorised into three different occurrences. The values below the negative standard deviation (-0.06), coloured in red, depict weak upwelling. Grey bars show regular upwelling. The values above the positive standard deviation (0.06), coloured in green, are qualified as strong upwellings at inter-annual time scale.

Figure 6.3a reveals that the periods from 1986 to 1988, from 1995 to 1996, in 2007 and in 2011 were periods of weak upwelling, while the upwelling was strong during the following years: 1990, 1993, 1994, 2000 and 2001. The rest of years in the time series, the upwelling has a regular strength (between the positive and negative standard deviation).

The highest upwelling intensity was found in the year 2000 with an anomaly of 0.14, while the lowest upwelling was recorded in 1998 and 2007, when both anomalies reached the -0.1 of intensity.

Core 2 anomalous upwelling index is shown in Figure 6.3b. The standard deviation of the anomaly is 0.057. Results reveal that the upwelling index anomaly exceeded the standard deviation in 1982, 1990, 1991, 1994, 2008, 2009 and 2013. And Core 2 appears weaker in 1989, 1992, 2004, 2006 and 2007.

It is noticed that the upwelling intensities from 1995 to 2007 were below the average (average from the signal before the anomaly: 0.22), while the upwelling intensities remain intermittently above the average from 2008 to 2014.

Figure 6.3 also shows the inter-annual variability of the wind stress anomaly in each Core (in 10^1 m^2 s^{-1}) overlaid on the upwelling index. The winds stresses vary similarly but the wind stress in Core 2 is more intense. The linear relationship between upwelling index and wind stress is tested to highlight the inter-annual contribution of the wind stress anomaly inducing inter-annual variability in the upwelling. Correlation factor between wind stress and anomalous

upwelling index for Core 1 is 0.21 and for Core 2 is 0.34, both are statistically significant at 95%. This result is aligned with the findings of Chapter 4, where Core 2 was shown to be more strongly influenced by the winds than Core 1.

Despite the correlation found here above, it is noticed for Core 2, high wind stress in some years (1984, 1987, 1988, 1999, 2003) does not imply an intense upwelling. This can be attributed to the ocean currents' influence on the upwelling.

Figure 6.3 reveals that abnormal upwelling index anomalies are not explained by the changes induced by the anomalous wind stress in each Core at inter-annual time scale. In other words, the inter-annual variability of the wind stress contributes less to the inter-annual variability of the upwelling. Hence, linking the inter-annual variability of the ocean currents with the upwelling indices should explain the major inter-annual variability of the upwelling.

Based on these results, there is a need to further investigate the inter-annual variability of the ocean circulation which seems to contribute significantly to the upwelling inter-annual variability.

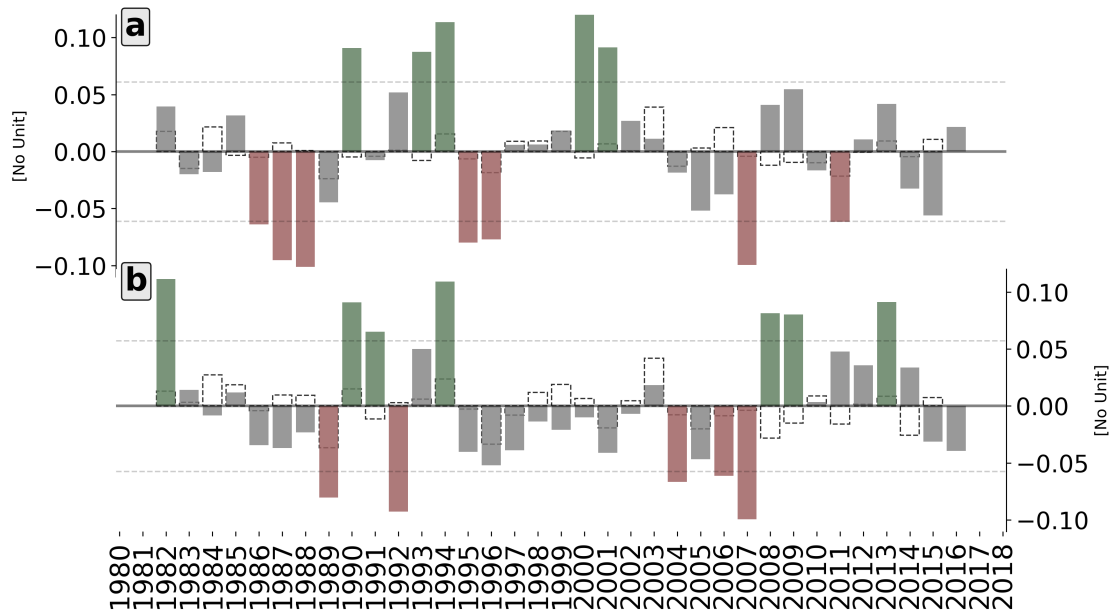

Figure 6.3: Inter-annual variability of upwelling index based on SST. a- Inter-annual anomaly de-trended of the upwelling index in Core 1. b- Inter-annual anomaly de-trended of the upwelling index in Core 2. For each subplot, dotted-lines are the positive and negative standard deviations of the anomaly. Green bars are the value of upwelling index reaching beyond the positive standard deviation. Red bars are the value of upwelling index reaching beyond the negative standard deviation. Grey bars belong to the normal upwelling intensities. Bar plots in black dotted line (a and b) are the inter-annual variability of the wind stress anomaly in each Core using DFS5.2 reanalysis wind product. The unit of the wind stress anomaly applied here is 10^1 m^2 s^{-1} with the aim to overlap the wind stress on top of the upwelling index.

6.3.2 Linking inter-annual variation of EMC and SMACC with the upwelling

6.3.2.1 EMC contribution to inter-annual variation of Core 1

With the view to characterise the inter-annual variability of the EMC and its interaction with the continental shelf, we analyse the inter-annual variability of the EMC southern extension. Figure 6.4 shows the results of inter-annual characteristics of EMC using the model solution. In Figure 6.4a, the SEC bifurcation position integrated over the first 1000 m is located between 19.97°S and 17.31°S. The mean position is 18.38°S, which is coherent with Chen et al. (2014) during the seasonal shifts in the location of the SEC bifurcation, estimated from the World Ocean Database and satellite altimeter observations. The inter-annual variation of SEC bifurcation is located abnormally far north, near 17.35°S, reaching beyond the standard deviation (0.6 degree grid) in 1994, 1999 and 2004. In 2000, we notice a location of the bifurcation, with

a mean position near 19.9°S.

Figure 6.4b shows the southward volume transport of the EMC integrated over the first 1000 m of depth. The mean volume transport of the EMC at 22°S is 18.3 Sv (1 Sv = 10^6 m^3 s^{-1}) with a standard deviation of 7.1 Sv which is consistent with the results of Ponsoni et al. (2016). The exceptional years with maximum values seen in Figure 6.4a also appear clearly in Figure 6.4b.

The inter-annual pattern explained in SEC bifurcation and EMC transport variations corresponds to the EMC mean offshore extent variations shown by the Figure 6.4c.

The EMC hits an irregular topography structure and appears to detach from the coast south-east of Madagascar at 24°S (Figure 6.1a). At this latitude, the EMC detachment appears to be associated with a cold water signature and high concentration of Chlorophyll-a (Chapter 4, Appendix A.4). This suggests that the interaction between EMC and bottom topography structure increased bottom friction against a widening shelf and associated with an increased Ekman veering near the sea bed which intensifies upwelling. Chapter 4 has identified potential section of coastline favourable for wind-driven upwelling south of Madagascar where the upstream detachment of EMC did not figure as a favourable coastline orientation. On the other hand, alongshore bottom stress calculated from model solution (Figure 6.1d) indicates an important stress which could favour an Ekman bottom transport. Hence, shelf-edge inducing upwelling and bottom Ekman transport should be the main mechanisms forcing vertical motion at 24°S. Figure 6.4d shows the inter-annual variability of the bottom Ekman transport induced by the near bottom stress velocity. Interestingly, the variation of the bottom Ekman transport is also linearly related with the SEC bifurcation and the EMC volume transport, respectively with a correlation factor -0.74 and 0.84, statistically significant at the 95% level of confidence.

Results reveal that SEC variations significantly influences the inter-annual variation of the EMC volume transport. It seems that more southward SEC bifurcation position associated with increase of the EMC volume transport (Figure 6.4 a-b). The inter-annual variation of the EMC position, represented by the mean offshore extent, seems also to be influenced by the inter-annual variation of the SEC bifurcation. Related to that, the SEC bifurcation also appear to regulate the inter-annual variation of the Ekman drift, calculated from the along-shelf bottom stress, inducing uplift of bottom water over the topography in vicinity of 24.5°S (Figure 6.4d).

The inter-annual variation of the upwelling index based on SST appears to have a linear agreement with the inter-annual variation of the Ekman drift, and to the SEC bifurcation calculated from the model, respectively with correlation factor 0.53 and -0.34, statistically significant at the 95% level of confidence.

This explains that the inter-annual variation of the upwelling cell in Core 1 is highly related with the large-scale circulation inducing the variation of the SEC in the Indian Ocean.

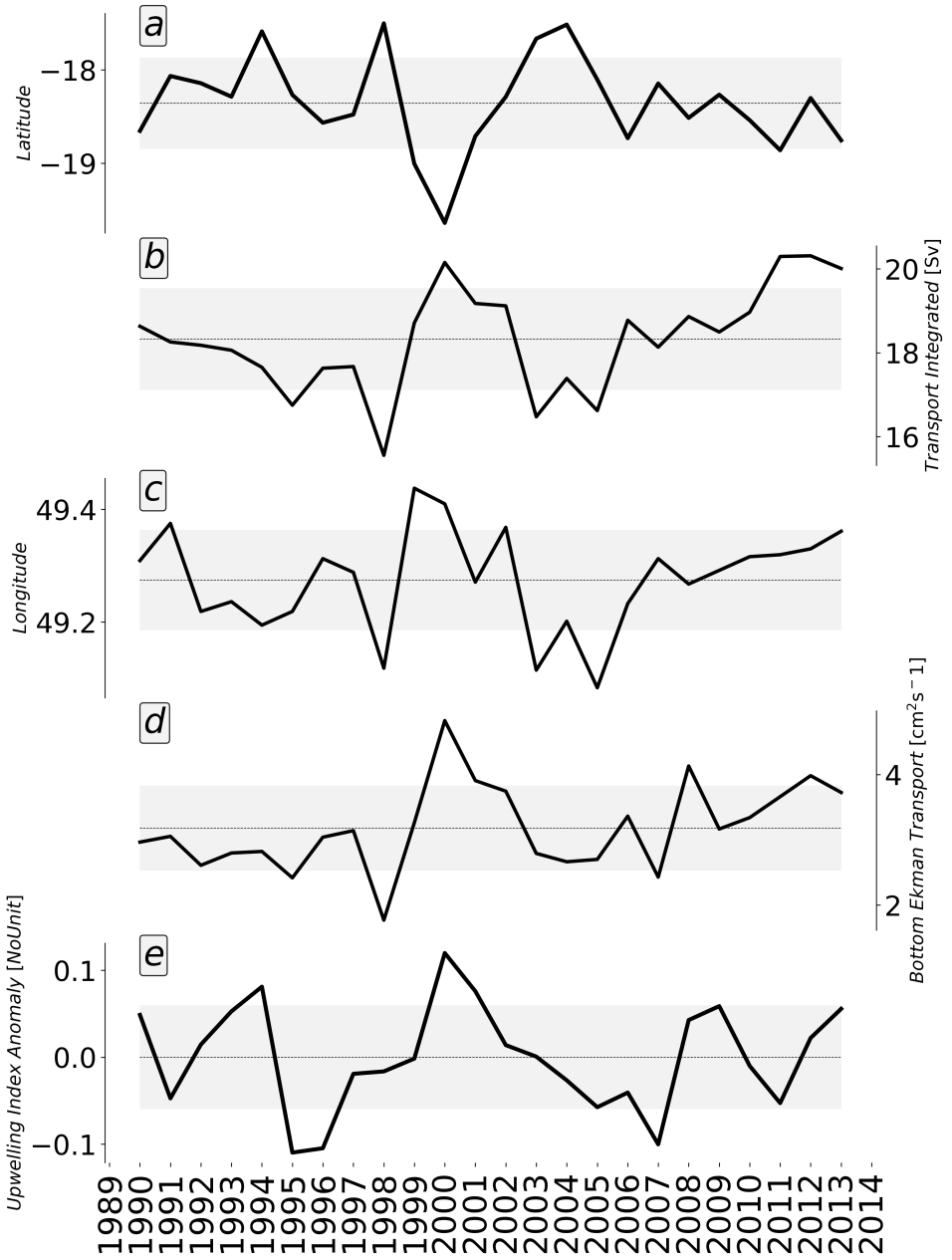

Figure 6.4: a- Inter-annual variation of SEC bifurcation integrated over the 1000 m depth using the model solution. b- Poleward volume transport (Sverdrup) integrated over 1000 m depth at the transect 22°S (Red transect Figure 6.1) using the model solution. c- EMC position at the transect 22°S (Red transect Figure 6.1) using the model solution. d- Ekman drift associated with the near botton stress of the velocity using the model solution. e- Upwelling index anomaly based of SST from satellite observation. For all subplots, dotted-lines indicate the mean and grey shade cover the standard deviation of time series.

6.3.2.2 SMACC contribution to inter-annual variation in Core 2

Inter-annual variations of the SMACC are investigated to test the inter-annual interaction between the SMACC and the inter-annual variation of the upwelling cell in Core 2.

The volume transport integrated over the first 100 m at the southern extension (mean depth of SMACC at 25°S the transect (Chapter 5)) is computed to characterise the inter-annual variability of the southern extension of the SMACC which is more connected with Core 2 (Chapter 5).

Figure 6.5a shows the inter-annual variation of the poleward volume transport of the SMACC. The inter-annual variation of wind stress curl, inside the SMACC area (42°E; 44°E and 22°S; 26°S) (Figure 6.2), is calculated and illustrated in Figure 6.5b. The analyses suggest that the observed cyclonic wind stress curl can lead to an intensification of the SMACC volume transport at inter-annual time scale. The linear relationship between the volume transport and the wind stress curl reveals a statistically significant correlation factor of up to -0.46. The result is aligned and reinforces the finding of Chapter 5 which pointed out that the surface speed of the SMACC is influenced by enhancement of the cyclonic wind stress curl during an annual cycle study.

The highest and the lowest upwelling (Figure 6.5b) are associated with the wind stress curl (Figure 6.3b). Increases in the SMACC volume transport, induced by wind stress curl intensification, tend to reduce the upwelling index in Core 2. The linear relationship between the SMACC volume transport and the upwelling index anomaly in Core 2 reveals a significant anti-correlation equal to -0.29. There is a connection between the SMACC and the upwelling intensity at inter-annual time scales, despite the weak correlation. Series of years highlighted in red (Figure 6.5) characterise period when the intensification of cyclonic wind stress curl (Figure 6.5b) enhances the SMACC volume transport (Figure 6.5a) and induces a weak upwelling surface signature (Figure 6.5c). On the other hand, the whole physical processes are not applicable for certain years highlighted in green colour (Figure 6.5b). This is probably due to the presence of cyclonic eddies, which being associated with the southern extension of SMACC explained in Chapter 5 (Figure 5.2 in transect *c*), which may generate changes at inter-annual time scale. As still little is known about the hydrography and water movements on the west coast of Madagascar at inter-annually time scale, further observations and in-situ measurements are needed to bright clarity to the inter-annual stability of the coastal current.

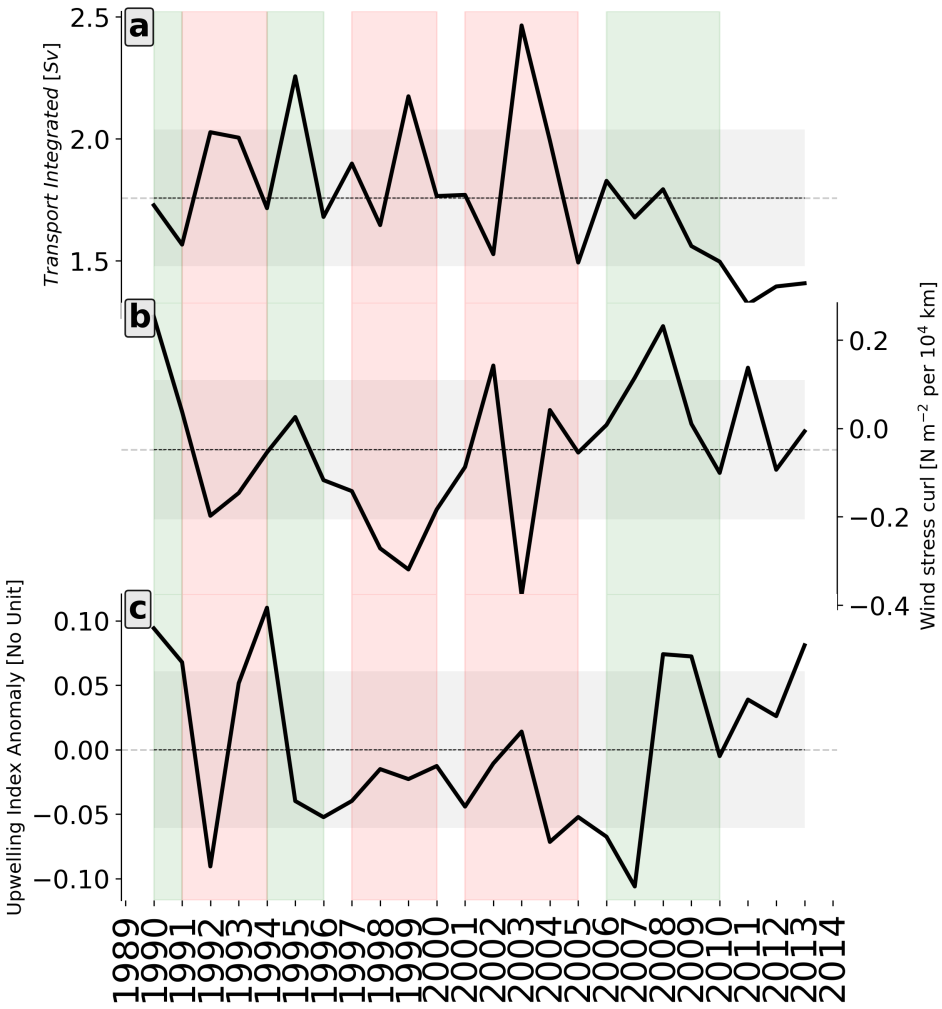

Figure 6.5: a- Inter-annual variability of the southward integrated volume transport (Sverdrup) of the SMACC over the first 100 m depth using the model solution. b- Inter-annual variability of wind stress curl anomaly (N m^{-2} per 10^4 km) taken in the area 42°E; 44° and 22°S; 26°S using DFS5.2 reanalysis wind product. c- Inter-annual variability of upwelling index anomaly based on SST from satellite observation. Red colour bands select periods where the SMACC volume transport is enhanced by the cyclonic wind curl and has a downstream impact on the upwelling cell Core 2 at inter-annually time scale. Green colour bands highlight series of years where the intensification of SMACC is not related with the cyclonic wind curl enhancement.

6.3.3 Remote connection with climatic modes

The aim of this section is to investigate the link between upwelling inter-annual variations and global/regional climate mode oscillations such as the SIOD, IOD and ENSO.

Figure 6.6 shows a linear lag-correlation between monthly anomalies of the upwelling index and the monthly climate mode oscillation indexes dominating the Indian Ocean variability which are the SIOD, IOD and ENSO. The black time series is the lag correlation between the upwelling index and the SIOD index, while the red time series is the lag correlation with the IOD index. The blue time series is the lag correlation between the upwelling index and the ENSO index.

Both Core 1 and Core 2 are significantly related to the SIOD with a maximum correlation found at less than one month lag (Figure 6.6). The upwelling is anti-correlated with the SIOD. The correlation factor is more important in Core 2 (coefficient of correlation = -0.28) than in Core 1 (coefficient of correlation = -0.16). This result explains that Core 2 is more exposed to the SIOD than the Core 1.

The upwelling is favorable during negative phase of SIOD which is characterised by the cold SST in the south-western part of Indian Ocean, in the vicinity of south Madagascar, and warm SST in the vicinity of Australia, while the opposite occurs during the positive phase (Behera & Yamagata 2001). During the negative phase, wind-evaporation-SST interactions explained by (Feng et al. 2014) occur in the vicinity of south Madagascar. The enhancement of evaporation to the south-west is followed by a cooling of SST which is associated with stronger winds in the south-eastern edge of Indian Ocean (Behera & Yamagata 2001). As Core 2 is mainly wind-driven upwelling, the anti-correlation highlighted in Figure 6.6 is linked with the variation of the winds during the SIOD events.

Figure 6.6 also reveals that the IOD is positively correlated with the upwelling index in Core 2 with a positive lag equal at three months (coefficient of correlation = 0.2). Core 2 is linearly linked with the positive IOD, where the tropical eastern Indian Ocean, in vicinity of Australia, is cooler but the tropical western Indian Ocean is warmer, in vicinity of northern tip of Madagascar (Marchant et al. 2007). On the other hand, Core 1 is not significantly affected by the IOD at the same period.

The lag correlation with the ENSO seems to be weak in both Core (coefficient of correlation = -0.15) but statistically significant. Both Cores appear to be influenced by the ENSO 12 months after the ENSO event. At the same time lag, the IOD also seems to affect both Cores.

The ENSO effect induces high anomalous SSTs in the entire Indian Ocean (Chambers et al. 1999). A rapid warming in the southern Indian Ocean caused variations of wind speed and enhanced the latent heat flux (Yu & Rienecker 1999). This reduces the total wind speed and diminishes the intensity of upwelling favorable winds. The variations in tropical SST and surface wind fields associated with the ENSO event is the mechanism which affects the upwelling at the south of Madagascar during the ENSO event.

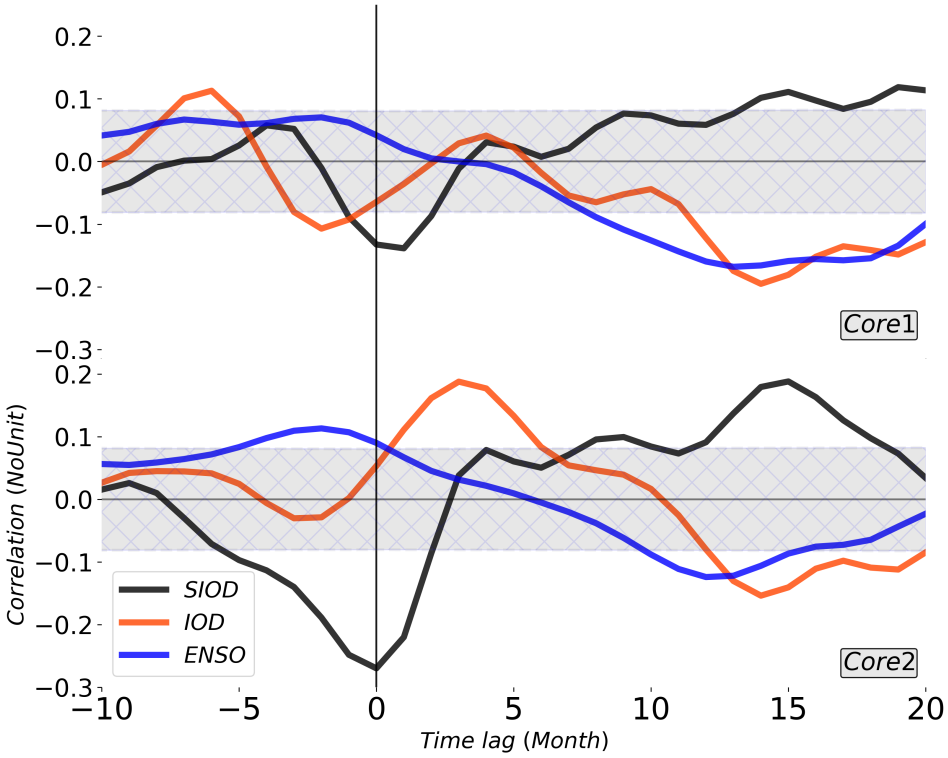

Figure 6.6: Lag correlation of upwelling index anomaly for each Core with ENSO index (blue), IOD index (red) and SIOD index (black). Cross-hatched and shaded area indicates non significant correlation, below the 95% significance level. We note that signals are filtered in two months running mean.

6.4 Discussions and conclusion

This work reveals that coastal upwelling south of Madagascar exhibits inter-annual variability associated with ocean currents and large-scale Indian Ocean climate modes.

Inter-annual variations in Core 1 and Core 2 are different and independent from each other. The anomalous upwelling index (Figure 6.3) varies differently in Core 1 and Core 2. Based on

the upwelling index, upwelling in both Cores was strong in 1990 and 1994 and weak only in 2007. Figure 6.3 shows that both upwelling indexes varies differently between 1997 and 2002. However, correlation factor between anomalous upwelling indexes reach 0.504 with a significant level of 0.001.

Core 1 and Core 2 exhibit a different inter-annual variability which is probably due to the inter-annual variation of the mechanisms.

Findings demonstrate that inter-annual variability of Core 1 and Core 2 is linked with the inter-annual variation of EMC and SMACC.

Results show changes in the location of the SEC bifurcation at inter-annual time scales impacting on the EMC strength and width. The inter-annual variations in the Ekman veering, associated with the EMC along-shore bottom stress velocity at 24.5°S, is also associated with variations in the SEC bifurcation. From these findings we conclude that the inter-annual variability of upwelling index Core 1 is linked with the variations of bottom Ekman transport, EMC transport and SEC bifurcation.

The relationship between SEC and EMC was mentioned by Chapman et al. (2003), de Ruijter et al. (2004), Nauw et al. (2008) who reported that the South Equatorial Current (SEC) is the main contributor to the EMC. Ponsoni et al. (2016) have reinforced that the major origin of the EMC is linked to the South Equatorial Current (SEC). However, Swallow et al. (1988), Schott & McCreary (2001) reported that the majority of the SEC fed more the equatorward branch than the poleward branch after hitting the east coast of Madagascar but the SEC remains the main contributor which influences the southern and the northern extension of each branches. Chen et al. (2014) investigated the SEC bifurcation off east Madagascar and found that the oscillation of volume transport of each branch (Northward and Southern) exhibits a seasonal variability. Chen et al. (2014) also demonstrated that the mean SEC bifurcation should favour more volume transport towards to south based on the Godfrey's island rule (Godfrey 1989). This means that the SEC may feed more the southern branch than the northern branch and could influence more the EMC.

This study clarifies the influence of the SEC to the EMC and its southern extension.

Masumoto & Meyers (1998), Palastanga et al. (2006) explained that it is the variability of the local wind field and the wind curl, in the central Indian Ocean, which modulates the SEC variability arriving at the east coast of Madagascar. This implies that the large scale gyre in Indian Ocean has an impact on the SEC which regulates the EMC volume transport and influence the

incidence of upwelling cell in Core 1.

Lutjeharms & Machu (2000), DiMarco et al. (2000) suggested that the upwelling is induced by the interaction between the EMC and the topography. This study confirmed and provided new insight on the interactions between the EMC and the coastal upwelling. Moreover, we have established that the dynamics of large-scale Indian Ocean gyre have an important impact on the upwelling system.

Our findings also highlight that inter-annual variability of Core 2 is influenced by the variability of SMACC. The inter-annual variability of the SMACC volume transport is linked with the inter-annual variability of the upwelling index. Intensification of the SMACC induces reduction in the upwelling index. The results suggest that the observed cyclonic wind stress curl can lead the intensification of the SMACC volume transport with a downstream impact on the upwelling. The intensity of the wind stress curl, by enhancing the SMACC, is the main forcing regulating the inter-annual variability of the upwelling cell in Core 2.

It was also found that it is not only the cyclonic wind stress curl which regulates the intensification of the SMACC at inter-annually time scale. In certain years (Figure 6.5), the intensification of the SMACC is not explained by the enhancement of the negative wind curl. This could be the contribution of the cyclonic mesoscale eddies to enhance the SMACC volume transport at the southern extension briefly explained in Chapter 5. Separating the contribution of dual forcing which intensifies the SMACC should be a further work to fully understand the implication of the southern extension of SMACC upon the intensity of the upwelling at inter-annually timescale.

Although there is limited number of years in the reconstructed upwelling index, linear relationships are consistent in concluding that both upwelling cells, Core 1 and Core 2, are locally influenced by the Subtropical Indian Ocean Dipole, where Core 2 is more impacted. The Core 2 is also more influenced by the positive Indian Ocean Dipole than Core 1 is. Moreover, effects of El-Niño Southern Oscillation have impacted both upwelling cells after a one year period.

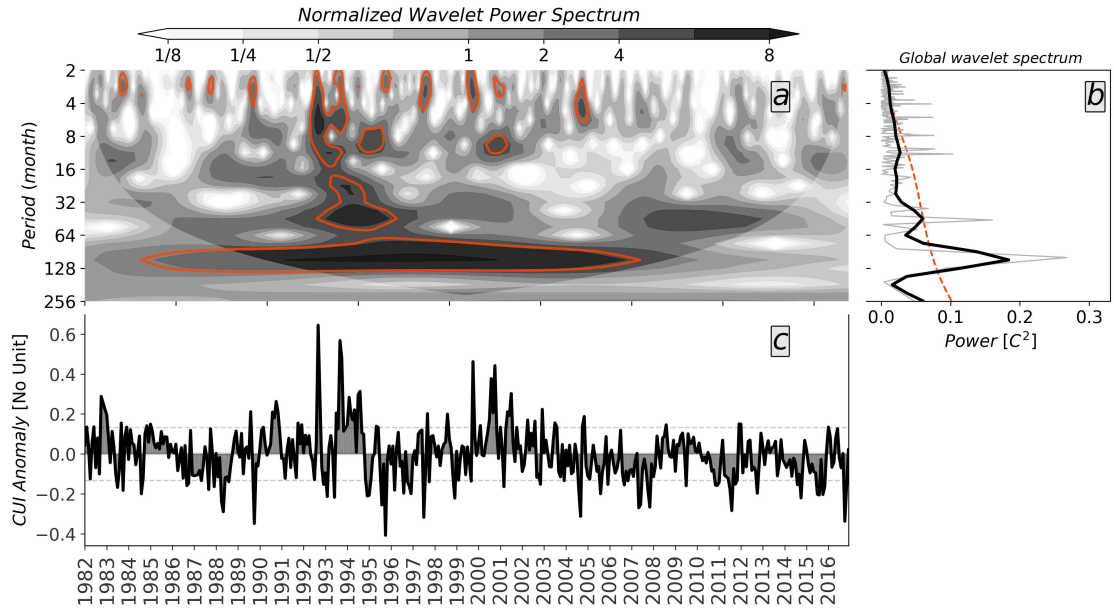

Figure 6.7: Periodicity of upwelling index anomaly for Core 1 using wavelet analysis. a- Wavelet power spectrum of the monthly upwelling index anomaly. Red contours denote the 95% of significance levels above a red noise background spectrum. Grey shaded area indicates the "Cone Of Influence" where the edge effects become important. b- The global wavelet power spectrum assuming the same significance level and background spectrum as in the wavelet power spectrum of the signal. The grey thin plots are the power spectrum of the signal. The black bold line is the power spectrum low-pass filtered. Above dashed lines correspond to the 95% significance level. c- Time series of the upwelling index anomaly at monthly time scale.

According to the Sverdrup theory, the subtropical gyres are driven by the wind curl due to the transition from the trade winds at the tropic level to the high latitude westerlies (Pedlosky et al. 1997). The dynamics of the wind stress anomalies is the potential mechanism associated with the flux of western boundary currents in the region (Palastanga et al. 2006, Chen et al. 2014). Changes in trade winds in the Indian Ocean during Indian Ocean Dipole and El-Niño Southern Oscillation event (Saji & Yamagata 2003, Wu & Kirtman 2004) can generate change in the ocean dynamics which can impact the upwelling processes induced and influenced by ocean currents. Palastanga et al. (2006) also mentioned that the South Equatorial Current (SEC), and its branches, along the east coast of Madagascar are weakened during the positive Indian Ocean Dipole event, but intensified during negative Indian Ocean Dipole. This highlights the possible contribution of climate teleconnection events in impacting coastal upwellings at Indian Ocean rim, including the upwelling south of Madagascar. For instance, the El-Niño Southern Oscillation events also reduce shelf-edge currents generating upwelling off south Australia during

the winter time (Middleton et al. 2007).

Allan et al. (1995) and Reason (2000) have revealed that the Indian Ocean exhibits a decadal variability. Core 1 seems to be more exposed to the Indian Ocean variability. Figure 6.7 provides explanatory analyses of the periodicity of the upwelling index in Core 1. Although the limited number of years in the data sets, Figure 6.7 shows a significant ten years period in the wavelet map (Figure 6.7a) and in spectral analysis (Figure 6.7b). This shows the evidence of a decadal variability affecting the upwelling. The decadal variability occurring in the Indian Ocean may also impact the SEC and induces a cascade effect toward the Core 1 variability. Han et al. (2014) have explained that the physical mechanism inducing the decadal variability is more attributed to the decadal variability of the El-Niño Southern Oscillation. Adding to that, Ashok, Chan, Motoi & Yamagata (2004) also revealed the existence of a high correlation between the decadal Indian Ocean Dipole events and the decadal variability of El-Niño Southern Oscillation occurring at the Indian Ocean. This study found that the Core 1 is more influenced by the El-Niño Southern Oscillation which can explain its exposure to the decadal variability.

In this study, it is found that the upwelling south of Madagascar inter-annual variation is dynamically complex and highly variable under the influence of the Eastern and Western boundary currents surrounding the upwelling in both sides. Undoubtedly, Indian Ocean climate oscillation remains the major influence which generates change in the ocean dynamics features. This clearly links upwelling with large scale Indian Ocean variation through teleconnections.

The inter-annual variability of the upwelling is important to further understand the variations in ocean circulation pattern in the region involving the upwelled water which remain unclear such as the formation of the dipole of mesoscale eddies at south of Madagascar and the system of the retroflection of the southern extension of EMC bringing nutrient to favour the phytoplankton bloom at Madagascar basin.

The inter-annual variability in this study is also important for anticipating changes in the upwelling productions for the socio-economic matters and fisheries related management. This could help to implement an eventual contingency and mitigation plan against the Indian Ocean climate variabilities influencing the upwelling occurrences.

Chapter 7

Conclusion and Perspectives

Satellite observations from multiple sensors, in-situ data sets and ocean model simulations were used to investigate the variability and the forcing mechanisms of the coastal upwelling south of Madagascar.

7.1 Variability of the upwelling cells

Satellite SST products were carefully selected to identify upwelling cells around the south Madagascar coast. A new algorithm based on the detection of colder waters from the SST imagery was proposed and combined to the Canny Edge detection algorithm to determine the offshore extent of the upwelling cells. Our analysis conducted over a period extending from 2003 to 2015 showed that two well defined upwelling cells exist: Core 1 to the south-east and Core 2 to the south-west. The colder waters observed in the SST imagery are associated with increased Chlorophyll-a concentration, confirming the occurrence of upwelling.

Core 1 and Core 2 are different. But the Core 1 appears to be more perennial, occurring 70 % of the time, while Core 2 occurs approximately 50 % of the time during the period of 2003 to 2015. This difference is attributed to the different variabilities regulating incidence of the coastal upwelling.

Both upwelling cells have a strong seasonal cycle, with a pronounced upwelling in austral winter and moderate in austral summer. Their seasonal cycles are in agreement with the Chlorophyll-a concentration response.

Core 1 and Core 2 exhibit different inter-annual variability which is linked to the ocean currents.

SST long term trend analyses revealed that both Cores are subjected of a slight warming where Core 1 is more exposed.

Inter-annual variability in both cores is influenced by the Subtropical Indian Ocean Dipole (SIOD) with a lesser influence of the Indian Ocean Dipole (IOD), particularly for Core 1. Inter annual variation in Core 1 and Core 2 also show a correlation with El-Niño Southern Oscillation (ENSO) with a 12 months lag.

The presence of two separated upwelling cells characterised by different spatial and temporal variability is attributed to the multiple and different physical forcing mechanisms which drive upwelling in Core 1 and Core 2.

7.2 Multiple forcing mechanisms of the upwelling cells

Chapter 4 revealed that the predominant easterly winds around Madagascar drive an offshore transport along the south coast and promote coastal upwelling. Winds vary seasonally and are more upwelling favourable during the austral winter season. While winds drive upwelling in both cores, the east/west orientation of the coastline near Core 2 implies a stronger response to upwelling favourable winds. The coastline of the eastern extension of Core 1, between 24.5°S and 25°S, appears to be not favorable for a wind-driven upwelling. An idealised simulation has been applied to test the sensitivity of the wind stress over the upwelling region. Result highlighted that a small part, especially the eastern extension, of Core 1 persisted after the test, while upwelling in Core 2 vanished.

The upwelling cell in Core 1 is primarily forced by the EMC. Based on our analysis of a two year time-series of the EMC volume transport derived from in-situ measurements (Ponsoni et al. 2015), we find that 61% of variability in Core 1 occurs as a result of changes in the EMC volume transport, with a stronger EMC favouring a more intense upwelling. The role of the EMC as a main driver of variability for Core 1 is confirmed through an analysis of model outputs from a high resolution simulation of the region. The pattern of inter-annual variability of the upwelling index in Core 1 appears to be linked with the EMC volume transport integrated over the 1000 m depth calculated from the model solution over a period of 24 years. The result confirmed a stronger EMC volume transport will drive intensified upwelling in Core 1.

The Ekman bottom transport at the southern extension of the EMC, calculated using the linear bottom stress theory (Schaeffer et al. 2014) reveal that the along-shelf advection of the EMC

generates uplift of bottom water due to high bottom stress in the vicinity of 24.5°S. The inter-annual variability of an Ekman bottom transport co-vary with the upwelling index inter-annual variation in Core 1. This result strengthens the hypothesis that interactions of the EMC with the topography drive a dynamic upwelling for Core 1 (Figure 4.12).
Another finding of this study was to show the impact of SEC variability on the EMC and in upwelling on Core 1, thus revealing the link between the SEC and upwelling south of Madagascar.

The Lagrangian experiments revealed that 81 % of upwelled water Core 2 arrived from the south-west of Madagascar, while a small portion of particles about 18.5% come from the EMC. This result reveals a presence of a flow coming from the Mozambique Channel. Satellite observations, Ship-board ADCP, Global drifters data and model solutions confirmed the presence of a previously unknown coastal current: the South-west MAdagascar Coastal Current (SMACC). Chapter 5 describes for the first time the physical characteristics of the SMACC. We showed that the SMACC is a surface warm coastal current situated at the south west of Madagascar, flowing from the Mozambique Channel toward the southern tip of Madagascar. The mechanism driving the SMACC is the intensification of the cyclonic wind stress curl due to the bending of the trade winds south of Madagascar.
Chapter 5 found an anti-correlation between the SMACC and the upwelling index associated with the Chlorophyll-a concentration in Core 2 at seasonal time scales. The SMACC has a downstream impact in Core 2. The warm water carried by SMACC appears to reduce the surface signature of the upwelling cell in Core 2. A deeper and stronger SMACC may lead to warm SMACC water being upwelled into Core 2. Chapter 6 also highlighted that the inter-annual variability of the upwelling index in Core 2 is linked with the inter-annual variability of the SMACC. Inter-annual variability of the cyclonic curl of the wind leads to a stronger SMACC and promotes decrease in Core 2. It is also suggested that the variation of the SMACC volume transport may interact with variations of the SMACC undercurrent which could further impact the upwelling.
Although Core 2 is primarily a wind-driven upwelling, the SMACC is another driver of its variability.

This study followed up on the research gaps and the recommendations identified in Lutjeharms & Machu (2000), DiMarco et al. (2000), Machu et al. (2002) and Ho et al. (2004) to

combine satellite observations from multiple sensors with numerical model simulation to improve understanding of the spatial extent and to elucidate mechanisms of the coastal upwelling south of Madagascar.

The highlights of the study are recapitulated in the Figure 7.1 which shows the presence of two separated upwelling cells (Figure 7.1), the existence of the new coastal current flowing south-west of Madagascar: the SMACC, and contribution of the coastal upwelling to the ocean circulation south of Madagascar which have important regional repercussions.

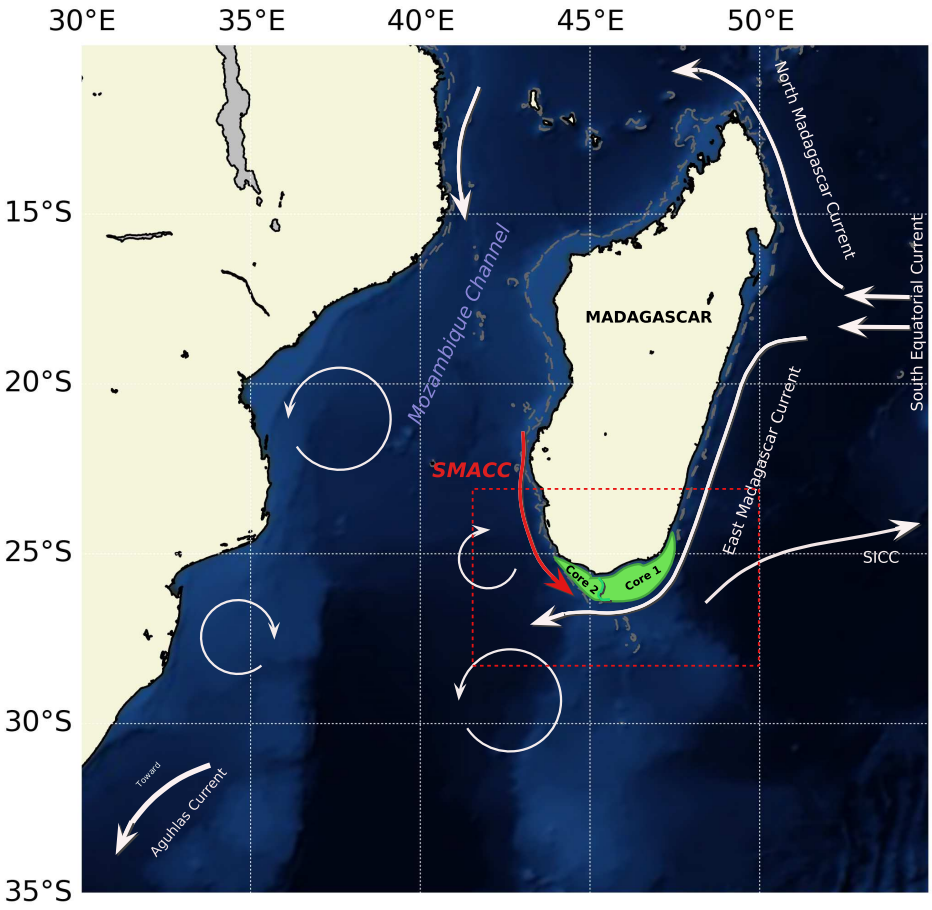

Figure 7.1: Schematic illustration of the local ocean circulation adapted from (DiMarco et al. 2000, Schott & McCreary 2001, DiMarco et al. 2002, Lutjeharms 2006). The green polygon illustrates the upwelling area. The red arrow is the illustration of the new coastal current: the SMACC.

7.3 Research outlook

The study provided understanding of upwelling variability and its mechanisms. Further investigations should be oriented to the study of the importance of the upwelled water contributing to the variability of the local and regional ocean circulation patterns. Literature mentioned the contribution of the upwelled water to influence the formation of mesoscale eddies dipole at the south of Madagascar (Ridderinkhof et al. 2013), and to favour the large phytoplankton bloom at the Madagascar basin (Longhurst 2001). Based on these connections, the variability of upwelling may explain the variability of the mesoscale eddies dipole occurrences, large phytoplankton bloom at the Madagascar basin, and the variability of Agulhas Current which needs to be investigated for a further work.

Bibliography

Allan, R. J., Lindesay, J. A. & Reason, C. J. (1995), 'Multidecadal variability in the climate system over the Indian Ocean region during the austral summer', *Journal of Climate* **8**(7), 1853–1873.
URL: *https://doi.org/10.1175/1520-0442(1995)008¡1853:MVITCS¿2.0.CO;2*

Allison, E. H., Perry, A. L., Badjeck, M.-C., Neil Adger, W., Brown, K., Conway, D., Halls, A. S., Pilling, G. M., Reynolds, J. D., Andrew, N. L. et al. (2009), 'Vulnerability of national economies to the impacts of climate change on fisheries', *Fish and fisheries* **10**(2), 173–196.
URL: *https://doi.org/10.1016/10.1111/j.1467-2979.2008.00310.x*

Alvarez, I., Gomez-Gesteira, M., Lorenzo, M., Crespo, A., Dias, J. et al. (2011), 'Comparative analysis of upwelling influence between the western and northern coast of the Iberian Peninsula', *Continental Shelf Research* **31**(5), 388–399.
URL: *https://doi.org/10.1016/j.csr.2010.07.009*

Ashok, K., Chan, W.-L., Motoi, T. & Yamagata, T. (2004), 'Decadal variability of the Indian Ocean Dipole', *Geophysical Research Letters* **31**(24).
URL: *https://doi.org/10.1029/2004GL021345*

Ashok, K., Guan, Z., Saji, N. & Yamagata, T. (2004), 'Individual and combined influences of enso and the Indian Ocean dipole on the Indian summer monsoon', *Journal of Climate* **17**(16), 3141–3155.
URL: *https://doi.org/10.1175/1520-0442(2004)017¡3141:IACIOE¿2.0.CO;2*

Ashok, K., Guan, Z. & Yamagata, T. (2001), 'Impact of the Indian Ocean dipole on the relationship between the Indian monsoon rainfall and enso', *Geophysical Research Letters*

28(23), 4499–4502.

URL: *https://doi-org.ezproxy.uct.ac.za/10.1029/2001GL013294*

Atlas, R., Hoffman, R. N., Ardizzone, J., Leidner, S. M., Jusem, J. C., Smith, D. K. & Gombos, D. (2011), 'A cross-calibrated, multiplatform ocean surface wind velocity product for meteorological and oceanographic applications', *Bulletin of the American Meteorological Society* **92**(2), 157–174.

URL: *https://doi.org/10.1175/2010BAMS2946.1*

Bakun, A. (1975), 'Daily and weekly upwelling indices, west coast of North America', *NOAA Tech. Rpt* **16**.

URL: *https://books.google.fr/books?id=D761PQAACAAJ*

Barber, R. & Smith, R. L. (1981), 'Coastal upwelling ecosystems', *Analysis of marine ecosystems/AR Longhurst* .

Behera, S. K. & Yamagata, T. (2001), 'Subtropical sst dipole events in the southern Indian Ocean', *Geophysical Research Letters* **28**(2), 327–330.

URL: *https://doi-org.ezproxy.uct.ac.za/10.1029/2000GL011451*

Bemiasa, J. (2009), Dynamique des pêcheries traditionnelles d'anchois, de calmars et de poulpes du Sud-Ouest de Madagascar: utilisation d'outils océanographiques pour la gestion des ressources., PhD thesis, Universite de Toliara, Madagascar.

URL: *http://archimer.ifremer.fr/doc/2009/these-6847.pdf*

Benazzouz, A., Mordane, S., Orbi, A., Chagdali, M., Hilmi, K., Atillah, A., Pelegrí, J. L. & Hervé, D. (2014), 'An improved coastal upwelling index from sea surface temperature using satellite-based approach–the case of the Canary Current upwelling system', *Continental Shelf Research* **81**, 38–54.

URL: *https://doi.org/10.1016/j.csr.2014.03.012*

Boo, G. H., Le Gall, L., Hwang, I. K. & Boo, S. M. (2016), 'Pterocladiella feldmannii sp. nov. and p. hamelii sp. nov.(gelidiales, rhodophyta), two new species uncovered in Madagascar during the atimo vatae expedition', *Cryptogamie, Algologie* .

URL: *https://doi.org/10.7872/crya/v37.iss3.2016.179*

Breuil, C. & Grima, D. (2014), 'Baseline report Madagascar. smartfish programme of the Indian Ocean commission', *Fisheries Management FAO component* **1**(35), 36.
URL: *www.fao.org/publications)*

Campos, E. J., Velhote, D. & da Silveira, I. C. (2000), 'Shelf break upwelling driven by Brazil Current cyclonic meanders', *Geophysical Research Letters* **27**(6), 751–754.
URL: *https://doi.org/10.1029/1999GL010502*

Canny, J. (1986), 'A computational approach to edge detection', *IEEE Transactions on pattern analysis and machine intelligence* (6), 679–698.
URL: *https://doi.org/10.1109/TPAMI.1986.4767851*

Casey, K. S., Brandon, T. B., Cornillon, P. & Evans, R. (2010), The past, present, and future of the AVHRR Pathfinder sst program, *in* 'Oceanography from space', Springer, pp. 273–287.

Chambers, D., Tapley, B. & Stewart, R. (1999), 'Anomalous warming in the Indian Ocean coincident with El-Nino', *Journal of Geophysical Research: Oceans* **104**(C2), 3035–3047.
URL: *https://doi-org.ezproxy.uct.ac.za/10.1029/1998JC900085*

Chapman, P., Di Marco, S., Davis, R. & Coward, A. (2003), 'Flow at intermediate depths around Madagascar based on ALACE float trajectories', *Deep Sea Research Part II: Topical Studies in Oceanography* **50**(12), 1957–1986.
URL: *https://doi.org/10.1016/S0967-0645(03)00040-7*

Chavez, F. P. & Messié, M. (2009), 'A comparison of eastern boundary upwelling ecosystems', *Progress in Oceanography* **83**(1-4), 80–96.
URL: *https://doi.org/10.1016/j.pocean.2009.07.032*

Chen, Z., Wu, L., Qiu, B., Sun, S. & Jia, F. (2014), 'Seasonal variation of the South Equatorial Current bifurcation off Madagascar', *Journal of Physical Oceanography* **44**(2), 618–631.
URL: *https://doi.org/10.1175/JPO-D-13-0147.1*

Chia, F., Griffiths, R. & Linden, P. (1982), 'Laboratory experiments on fronts: Part ii: The formation of cyclonic eddies at upwelling fronts', *Geophysical & Astrophysical Fluid Dynamics* **19**(3-4), 189–206.
URL: *https://doi.org/10.1080/03091928208208955*

Chorin, A. J. (1968), 'Numerical solution of the Navier-Stokes equations', *Mathematics of computation* **22**(104), 745–762.
URL: *https://doi.org/10.1090/S0025-5718-1968-0242392-2*

Conkright, M. E., Locarnini, R. A., Garcia, H. E., O'Brien, T. D., Boyer, T. P., Stephens, C. & Antonov, J. I. (2002), *World Ocean Atlas 2001: Objective analyses, data statistics, and figures: CD-ROM documentation*, US Department of Commerce, National Oceanic and Atmospheric Administration, National Oceanographic Data Center, Ocean Climate Laboratory.

Cresswell, G. R. & Golding, T. (1980), 'Observations of a south-flowing current in the southeastern Indian Ocean', *Deep Sea Research Part A. Oceanographic Research Papers* **27**(6), 449–466.
URL: *https://doi.org/10.1016/0198-0149(80)90055-2*

Croquette, M., Eldin, G., Grados, C. & Tamayo, M. (2007), 'On differences in satellite wind products and their effects in estimating coastal upwelling processes in the south-east Pacific', *Geophysical research letters* **34**(11).
URL: *https://doi.org/10.1029/2006GL027538*

Davies, T., Beanjara, N. & Tregenza, T. (2009), 'A socio-economic perspective on gear-based management in an artisanal fishery in south-west Madagascar', *Fisheries Management and Ecology* **16**(4), 279–289.
URL: *https://doi.org/10.1111/j.1365-2400.2009.00665.x*

de Boyer Montégut, C., Madec, G., Fischer, A. S., Lazar, A. & Iudicone, D. (2004), 'Mixed layer depth over the global ocean: An examination of profile data and a profile-based climatology', *Journal of Geophysical Research: Oceans* **109**(C12).
URL: *https://doi.org/10.1029/2004JC002378*

de Ruijter, W. P., Ridderinkhof, H., Lutjeharms, J. R., Schouten, M. W. & Veth, C. (2002), 'Observations of the flow in the Mozambique Channel', *Geophysical Research Letters* **29**(10).
URL: *https://doi.org/10.1029/2001GL013714*

De Ruijter, W. P., Ridderinkhof, H. & Schouten, M. W. (2005), 'Variability of the southwest Indian Ocean', *Philosophical Transactions of the Royal Society of London A: Mathematical, Physical and Engineering Sciences* **363**(1826), 63–76.
URL: *https://doi.org/10.1098/rsta.2004.1478*

de Ruijter, W. P., van Aken, H. M., Beier, E. J., Lutjeharms, J. R., Matano, R. P. & Schouten, M. W. (2004), 'Eddies and dipoles around South Madagascar: formation, pathways and large-scale impact', *Deep Sea Research Part I: Oceanographic Research Papers* **51**(3), 383–400.
URL: *https://doi.org/10.1016/j.dsr.2003.10.011*

Debreu, L., Marchesiello, P., Penven, P. & Cambon, G. (2012), 'Two-way nesting in split-explicit ocean models: algorithms, implementation and validation', *Ocean Modelling* **49**, 1–21.
URL: *https://doi.org/10.1016/j.ocemod.2012.03.003*

Dee, D., Uppala, S., Simmons, A., Berrisford, P., Poli, P., Kobayashi, S., Andrae, U., Balmaseda, M., Balsamo, G., Bauer, P. et al. (2011), 'The ERA-Interim reanalysis: Configuration and performance of the data assimilation system', *Quarterly Journal of the royal meteorological society* **137**(656), 553–597.
URL: *https://doi.org/10.1002/qj.828*

Demarq, H. & Faure, V. (2000), 'Coastal upwelling and associated retention indices derived from satellite sst. application to octopus vulgaris recruitment', *Oceanologica Acta* **23**(4), 391–408.
URL: *https://doi.org/10.1016/S0399-1784(00)01113-0*

DiMarco, S. F., Chapman, P. & Nowlin, W. D. (2000), 'Satellite observations of upwelling on the continental shelf south of Madagascar', *Geophysical Research Letters* **27**(24), 3965–3968.
URL: *https://doi.org/10.1029/2000GL012012*

DiMarco, S. F., Chapman, P., Nowlin, W. D., Hacker, P., Donohue, K., Luther, M., Johnson, G. C. & Toole, J. (2002), 'Volume transport and property distributions of the Mozambique Channel', *Deep Sea Research Part II: Topical Studies in Oceanography* **49**(7), 1481–1511.
URL: *https://doi.org/10.1016/S0967-0645(01)00159-X*

Donguy, J.-R. & Piton, B. (1969), 'Aperçu des conditions hydrologiques de la partie nord du canal de Mozambique', *Cahier ORSTOM* **7**(2), 3–26.
URL: *https://agris.fao.org*

Dufois, F. & Rouault, M. (2012), 'Sea surface temperature in false bay (south africa): Towards a better understanding of its seasonal and inter-annual variability', *Continental Shelf Research* **43**, 24–35.
URL: *https://doi.org/10.1016/j.csr.2012.04.009*

Dussin, R., Barnier, B., Brodeau, L. & Molines, J. M. (2016), 'Drakkar forcing set dfs5', *Repport* **1**, 34.

Ekman, V. W. et al. (1905), 'On the influence of the earth's rotation on ocean-currents.'.
URL: *https://jscholarship.library.jhu.edu/bitstream/handle/1774.2/33989/31151027498728.pdf*

Emery, W., Baldwin, D., Schlüssel, P. & Reynolds, R. (2001), 'Accuracy of in situ sea surface temperatures used to calibrate infrared satellite measurements', *Journal of Geophysical Research: Oceans* **106**(C2), 2387–2405.
URL: *https://doi.org/10.1029/2000JC000246*

Fairall, C. W., Bradley, E. F., Rogers, D. P., Edson, J. B. & Young, G. S. (1996), 'Bulk parameterization of air-sea fluxes for tropical ocean-global atmosphere coupled-ocean atmosphere response experiment', *Journal of Geophysical Research: Oceans* **101**(C2), 3747–3764.
URL: *https://doi.org/10.1029/95JC03205*

Feng, J., Hu, D. & Yu, L. (2014), 'How does the Indian Ocean subtropical dipole trigger the tropical Indian Ocean dipole via the mascarene high?', *Acta Oceanologica Sinica* **33**(1), 64–76.
URL: *https://doi.org/10.1007/s13131-014-0425-6*

Feng, M., Meyers, G., Pearce, A. & Wijffels, S. (2003), 'Annual and interannual variations of the Leeuwin Current at 32 s', *Journal of Geophysical Research: Oceans* **108**(C11).
URL: *https://doi.org/10.1029/2002JC001763*

Ferry, N., Parent, L., Garric, G., Bricaud, C., Testut, C., Le Galloudec, O., Lellouche, J., Drévillon, M., Greiner, E., Barnier, B. et al. (2012), 'GLORYS2V1 global ocean reanalysis of the altimetric era (1992-2009) at meso-scale. Mercator quarterly newsletter 44, january 2012, 29-39'.

Figueiras, F., Labarta, U. & Reiriz, M. F. (2002), Coastal upwelling, primary production and mussel growth in the rías baixas of Galicia, *in* 'Sustainable Increase of Marine Harvesting: Fundamental Mechanisms and New Concepts', Springer,Dordrecht, 2002., pp. 121–131.

Furue, R., Guerreiro, K., Phillips, H. E., McCreary Jr, J. P. & Bindoff, N. L. (2017), 'On the Leeuwin current system and its linkage to zonal flows in the south Indian Ocean as inferred

from a gridded hydrography', *Journal of Physical Oceanography* **47**(3), 583–602.
URL: *https://doi.org/10.1175/JPO-D-16-0170.1*

Gentemann, C. L., Fewings, M. R. & García-Reyes, M. (2017), 'Satellite sea surface temperatures along the west coast of the United States during the 2014–2016 northeast Pacific marine heat wave', *Geophysical Research Letters* **44**(1), 312–319.
URL: *https://doi.org/10.1002/2016GL071039.*

Global, O. (2013), 'ASCAT Wind Product User Manual'.

Godfrey, J. (1989), 'A Sverdrup model of the depth-integrated flow for the world ocean allowing for island circulations', *Geophysical & Astrophysical Fluid Dynamics* **45**(1-2), 89–112.
URL: *https://doi.org/10.1080/03091928908208894*

Gonzalez-Nuevo, G., Gago, J. & Cabanas, J. (2014), 'Upwelling index: a powerful tool for marine research in the NW Iberian upwelling system', *Journal of Operational Oceanography* **7**(1), 47–57.
URL: *http://dx.doi.org/10.1080/1755876X.2014.11020152*

Gordon, A. L. & Fine, R. A. (1996), 'Pathways of water between the Pacific and Indian Oceans in the Indonesian seas', *Nature* **379**(6561), 146.
URL: *https://search.proquest.com/docview/204479301?accountid=14500*

Guan, L. & Kawamura, H. (2004), 'Merging satellite infrared and microwave ssts: Methodology and evaluation of the new sst', *Journal of Oceanography* **60**(5), 905–912.
URL: *http://dx.doi.org/10.1007/s10872-004-5782-x*

Gula, J., Molemaker, M. J. & McWilliams, J. C. (2014), 'Submesoscale cold filaments in the Gulf Stream', *Journal of Physical Oceanography* **44**(10), 2617–2643.
URL: *http://dx.doi.org/10.1175/JPO-D-14-0029.1*

Gunther, E. (1936), 'A report on oceanographic investigations in the Peru Coastal Current, discovery reports, 13, 107-276'.

Haidvogel, D. B. & Beckmann, A. (1999), *Numerical ocean circulation modeling*, World Scientific.

Halo, I., Backeberg, B., Penven, P., Ansorge, I., Reason, C. & Ullgren, J. (2014), 'Eddy properties in the Mozambique Channel: A comparison between observations and two numerical ocean circulation models', *Deep Sea Research Part II: Topical Studies in Oceanography* **100**, 38–53.
URL: *https://doi.org/10.1016/j.dsr2.2013.10.015*

Han, W., Vialard, J., McPhaden, M. J., Lee, T., Masumoto, Y., Feng, M. & De Ruijter, W. P. (2014), 'Indian Ocean decadal variability: A review', *Bulletin of the American Meteorological Society* **95**(11), 1679–1703.
URL: *https://doi.org/10.1175/BAMS-D-13-00028.1*

Hasager, C. B., Mouche, A., Badger, M., Bingöl, F., Karagali, I., Driesenaar, T., Stoffelen, A., Peña, A. & Longépé, N. (2015), 'Offshore wind climatology based on synergetic use of Envisat ASAR, ASCAT and QuikSCAT', *Remote Sensing of Environment* **156**, 247–263.
URL: *https://doi.org/10.1016/j.rse.2014.09.030*

Higdon, D. (1998), 'A process-convolution approach to modelling temperatures in the North Atlantic Ocean', *Environmental and Ecological Statistics* **5**(2), 173–190.
URL: *https://doi.org/10.1023/A:1009666805688*

Hilburn, K., Wentz, F., Smith, D. & Ashcroft, P. (2006), 'Correcting active scatterometer data for the effects of rain using passive radiometer data', *Journal of applied meteorology and climatology* **45**(3), 382–398.
URL: *http://dx.doi.org/10.1175/JAM2357.1*

Ho, C.-R., Zheng, Q. & Kuo, N.-J. (2004), 'SeaWiFs observations of upwelling south of Madagascar: long-term variability and interaction with East Madagascar Current', *Deep Sea Research Part II: Topical Studies in Oceanography* **51**(1), 59–67.
URL: *https://doi.org/10.1016/j.dsr2.2003.05.001*

Hoerling, M. P., Hurrell, J. W., Xu, T., Bates, G. T. & Phillips, A. (2004), 'Twentieth century north Atlantic climate change. part ii: Understanding the effect of Indian Ocean warming', *Climate Dynamics* **23**(3-4), 391–405.
URL: *https://doi.org/0.1007/s00382-004-0433-x*

Hood, R. R., Beckley, L. E. & Wiggert, J. D. (2017), 'Biogeochemical and ecological impacts

of boundary currents in the Indian Ocean', *Progress in Oceanography* **156**, 290–325.
URL: *https://doi.org/10.1016/j.pocean.2017.04.011*

Houart, R. & Héros, V. (2013), 'Description of new Muricidae (Mollusca: Gastropoda) collected during the ATIMO VATAE expedition to Madagascar "Deep South"', *Zoosystema* **35**(4), 503–523.
URL: *http://dx.doi.org/10.5252/z2013n4a5*

Houart, R. & Héros, V. (2015), 'New species of Muricidae Rafinesque, 1815 (mollusca: Gastropoda) from the western Indian Ocean', *Zoosystema* **37**(3), 481–503.
URL: *https://doi.org/10.5252/z2015n3a4*

Huhn, F., Kameke, A., Pérez-Muñuzuri, V., Olascoaga, M. & Beron-Vera, F. (2012), 'The impact of advective transport by the south Indian Ocean countercurrent on the Madagascar plankton bloom', *Geophysical Research Letters* **39**(6).
URL: *https://doi.org/10.1029/2012GL051246*

Huyer, A. & Smith, R. L. (1985), 'The signature of El-Nino off Oregon, 1982–1983', *Journal of Geophysical Research: Oceans* **90**(C4), 7133–7142.
URL: *https://doi.org/10.1029/JC090iC04p07133*

Johannessen, J., Chapron, B., Collard, F., Rio, M., Piollé, J., Quartly, G., Shutler, J., Donlon, C., Danielson, R., Korosov, A. et al. (2015), Globcurrent: Sentinel-3 synergy in action, *in* 'Proceedings of Sentinel-3 for Science Workshop (2-5 June 2015, Venice, Italy)', ESA.
URL: *http://adsabs.harvard.edu/abs/2015ESASP.734....2J*

Jose, Y. S., Penven, P., Aumont, O., Machu, E., Moloney, C., Shillington, F. & Maury, O. (2016), 'Suppressing and enhancing effects of mesoscale dynamics on biological production in the Mozambique Channel', *Journal of Marine Systems* **158**, 129–139.
URL: *https://doi.org/10.1016/j.jmarsys.2016.02.003*

Kai, E. T., Rossi, V., Sudre, J., Weimerskirch, H., Lopez, C., Hernandez-Garcia, E., Marsac, F. & Garçon, V. (2009), 'Top marine predators track Lagrangian coherent structures', *Proceedings of the National Academy of Sciences* **106**(20), 8245–8250.
URL: *https://doi.org/10.1073/pnas.0811034106*

Kämpf, J. & Chapman, P. (2016), *Upwelling Systems of the World: A Scientific Journey to the Most Productive Marine Ecosystems*, Springer international publishing, Switzerland, 2016.
URL: *https://doi.org/10.1007/978-3-319-42524-5*

Kug, J.-S., Li, T., An, S.-I., Kang, I.-S., Luo, J.-J., Masson, S. & Yamagata, T. (2006), 'Role of the enso–Indian Ocean coupling on enso variability in a coupled gcm', *Geophysical research letters* **33**(9).
URL: *https://doi.org/10.1029/2005GL024916*

Kumar, K. K., Rajagopalan, B. & Cane, M. A. (1999), 'On the weakening relationship between the Indian monsoon and ENSO', *Science* **284**(5423), 2156–2159.
URL: *https://doi.org/10.1126/science.284.5423.2156*

Large, W. & Pond, S. (1981), 'Open ocean momentum flux measurements in moderate to strong winds', *Journal of physical oceanography* **11**(3), 324–336.
URL: *https://doi.org/10.1175/1520-0485(1981)011¡0324:OOMFMI¿2.0.CO;2*

Le Hénaff, M., Roblou, L. & Bouffard, J. (2011), 'Characterizing the Navidad current interannual variability using coastal altimetry', *Ocean Dynamics* **61**(4), 425–437.
URL: *https://doi.org/10.1007/s10236-010-0360-9*

Le Manach, F., Gough, C., Harris, A., Humber, F., Harper, S. & Zeller, D. (2012), 'Unreported fishing, hungry people and political turmoil: the recipe for a food security crisis in Madagascar?', *Marine policy* **36**(1), 218–225.
URL: *https://doi.org/10.1016/j.marpol.2011.05.007*

Lee, T. N., Yoder, J. A. & Atkinson, L. P. (1991), 'Gulf Stream frontal eddy influence on productivity of the southeast us continental shelf', *Journal of Geophysical Research: Oceans* **96**(C12), 22191–22205.
URL: *https://doi.org/10.1029/91JC02450*

Lett, C., Verley, P., Mullon, C., Parada, C., Brochier, T., Penven, P. & Blanke, B. (2008), 'A Lagrangian tool for modelling ichthyoplankton dynamics', *Environmental Modelling & Software* **23**(9), 1210–1214.
URL: *https://doi.org/10.1016/j.envsoft.2008.02.005*

Liu, Y. & Minnett, P. J. (2016), 'Sampling errors in satellite-derived infrared sea-surface temperatures. part i: Global and regional modis fields', *Remote sensing of environment* **177**, 48–64.
URL: *https://doi.org/10.1016/j.rse.2016.02.026*

Longhurst, A. (2001), 'A major seasonal phytoplankton bloom in the Madagascar basin', *Deep Sea Research Part I: Oceanographic Research Papers* **48**(11), 2413–2422.
URL: *https://doi.org/10.1016/S0967-0637(01)00024-3*

Lumpkin, R. & Pazos, M. (2007), 'Measuring surface currents with surface velocity program drifters: the instrument, its data, and some recent results', *Lagrangian analysis and prediction of coastal and ocean dynamics* pp. 39–67.

Lutjeharms, J. (1976), 'The agulhas current system during the northeast monsoon season', *Journal of Physical Oceanography* **6**(5), 665–670.
URL: *https://doi.org/10.1175/1520-0485(1976)006¡0665:TACSDT¿2.0.CO;2*

Lutjeharms, J. (1988), 'Remote sensing corroboration of retroflection of the east Madagascar current', *Deep Sea Research Part A. Oceanographic Research Papers* **35**(12), 2045–2050.
URL: *https://doi.org/10.1016/0198-0149(88)90124-0*

Lutjeharms, J., Bang, N. & Duncan, C. (1981), 'Characteristics of the currents east and south of Madagascar', *Deep Sea Research Part A. Oceanographic Research Papers* **28**(9), 879–899.
URL: *https://doi.org/10.1016/0198-0149(81)90008-X*

Lutjeharms, J. & Machu, E. (2000), 'An upwelling cell inshore of the East Madagascar Current', *Deep Sea Research Part I: Oceanographic Research Papers* **47**(12), 2405–2411.
URL: *https://doi.org/10.1016/S0967-0637(00)00026-1*

Lutjeharms, J. R. (2006), *The Agulhas Current*, Vol. 2, Springer.

Lutjeharms, J., Wedepohl, P. & Meeuwis, J. (2000), 'On the surface drift of the east Madagascar and mozambique currents.', *South African Journal of Science* **96**(3).

Lynn, R. J. & Simpson, J. J. (1987), 'The California Current System: The seasonal variability of its physical characteristics', *Journal of Geophysical Research: Oceans* **92**(C12), 12947–12966.
URL: *https://doi.org/10.1029/JC092iC12p12947*

Machu, E., Lutjeharms, J., Webb, A. & Van Aken, H. (2002), 'First hydrographic evidence of the southeast Madagascar upwelling cell', *Geophysical research letters* **29**(21).
URL: *https://doi.org/10.1029/2002GL015381*

Maes, C., Grima, N., Blanke, B., Martinez, E., Paviet-Salomon, T. & Huck, T. (2018), 'A surface "superconvergence" pathway connecting the south Indian Ocean to the subtropical south Pacific gyre', *Geophysical Research Letters* **45**(4), 1915–1922.
URL: *https://doi.org/10.1002/2017GL076366*

Manghisi, A., Morabito, M., Boo, G. H., Boo, S. M., Bonillo, C., Clerck, O. D. & Gall, L. L. (2015), 'Two novel species of yonagunia (halymeniales, rhodophyta) were uncovered in the south of Madagascar during the Atimo-Vatae Expedition', *Cryptogamie, Algologie* **36**(2), 199–217.
URL: *https://doi.org/10.7872/crya.v36.iss2.2015.199*

Marchant, R., Mumbi, C., Behera, S. & Yamagata, T. (2007), 'The Indian Ocean dipole–the unsung driver of climatic variability in east africa', *African Journal of Ecology* **45**(1), 4–16.
URL: *https://doi.org/10.1111/j.1365-2028.2006.00707.x*

Masumoto, Y. & Meyers, G. (1998), 'Forced rossby waves in the southern tropical Indian Ocean', *Journal of Geophysical Research: Oceans* **103**(C12), 27589–27602.
URL: *https://doi.org/10.1029/98JC02546*

Maximenko, N., Niiler, P., Centurioni, L., Rio, M.-H., Melnichenko, O., Chambers, D., Zlotnicki, V. & Galperin, B. (2009), 'Mean dynamic topography of the ocean derived from satellite and drifting buoy data using three different techniques', *Journal of Atmospheric and Oceanic Technology* **26**(9), 1910–1919.
URL: *https://doi.org/10.1175/2009JTECHO672.1*

Middleton, J. F., Arthur, C., Van Ruth, P., Ward, T. M., McClean, J. L., Maltrud, M. E., Gill, P., Levings, A. & Middleton, S. (2007), 'El nino effects and upwelling off south australia', *Journal of Physical Oceanography* **37**(10), 2458–2477.
URL: *https://doi.org/10.1175/JPO3119.1*

Morioka, Y., Tozuka, T. & Yamagata, T. (2013), 'How is the indian ocean subtropical dipole excited?', *Climate dynamics* **41**(7-8), 1955–1968.
URL: *https://doi.org/0.1007/s00382-012-1584-9*

Nauw, J., Van Aken, H., Webb, A., Lutjeharms, J. & De Ruijter, W. (2008), 'Observations of the southern east Madagascar current and undercurrent and countercurrent system', *Journal of Geophysical Research: Oceans* **113**(C8).
URL: *https://doi.org/10.1029/2007JC004639*

Ollitrault, M. & Rannou, J.-P. (2013), 'Andro: An argo-based deep displacement dataset', *Journal of Atmospheric and Oceanic Technology* **30**(4), 759–788.

Oram, J. J., McWilliams, J. C. & Stolzenbach, K. D. (2008), 'Gradient-based edge detection and feature classification of sea-surface images of the southern california bight', *Remote Sensing of Environment* **112**(5), 2397–2415.
URL: *https://doi.org/10.1016/j.rse.2007.11.010*

Othman, Z., Abdullah, A. & Prabuwono, A. S. (2012), A statistical approach of multiple resolution levels for canny edge detection, *in* 'Intelligent Systems Design and Applications (ISDA), 2012 12th International Conference on', IEEE, pp. 837–841.
URL: *https://doi.org/10.1109/ISDA.2012.6416646*

Palastanga, V., Van Leeuwen, P. & De Ruijter, W. (2006), 'A link between low-frequency mesoscale eddy variability around Madagascar and the large-scale Indian Ocean variability', *Journal of Geophysical Research: Oceans* **111**(C9).
URL: *https://doi-org/10.1029/2005JC003081*

Palastanga, V., Van Leeuwen, P., Schouten, M. & De Ruijter, W. (2007), 'Flow structure and variability in the subtropical Indian Ocean: Instability of the south Indian Ocean countercurrent', *Journal of Geophysical Research: Oceans* **112**(C1).
URL: *https://doi-org/10.1029/2005JC003395*

Paubert, M. T., Rijasoa, F. & Remanevy, M. E. (2015), 'Ressources halieutiques potentielles et propositions d'adaptation aux variabilités climatiques dans l'extrême sud de Madagascar', *Mediterránea: serie de estudios biológicos* **10**(26), 183–235.
URL: *http://dx.doi.org/10.14198/MDTRRA2015.ESP.09*

Pedlosky, J., Pratt, L. J., Spall, M. A. & Helfrich, K. R. (1997), 'Circulation around islands and ridges', *Journal of Marine Research* **55**(6), 1199–1251.
URL: *https://doi-org.ezproxy.uct.ac.za/10.1357/0022240973224085*

Perlin, A., Moum, J. & Klymak, J. (2005), 'Response of the bottom boundary layer over a sloping shelf to variations in alongshore wind', *Journal of Geophysical Research: Oceans* **110**(C10).
URL: *https://doi.org/10.1029/2004JC002500*

Pfeiffer, M. & Dullo, W.-C. (2006), 'Monsoon-induced cooling of the western equatorial Indian Ocean as recorded in coral oxygen isotope records from the seychelles covering the period of 1840–1994 ad', *Quaternary Science Reviews* **25**(9-10), 993–1009.
URL: *https://doi.org/10.1016/j.quascirev.2005.11.005*

Ping, B., Su, F., Meng, Y., Du, Y. & Fang, S. (2016), 'Application of a sea surface temperature front composite algorithm in the Bohai, Yellow, and East China Seas', *Chinese Journal of Oceanology and Limnology* **34**, 597–607.
URL: *https://doi.org/10.1007/s00343-015-4356-7*

Ponsoni, L., Aguiar-González, B., Maas, L., van Aken, H. & Ridderinkhof, H. (2015), 'Long-term observations of the east Madagascar undercurrent', *Deep Sea Research Part I: Oceanographic Research Papers* **100**, 64–78.
URL: *https://doi.org/10.1016/j.dsr.2015.02.004*

Ponsoni, L., Aguiar-González, B., Ridderinkhof, H. & Maas, L. R. (2016), 'The East Madagascar Current: Volume transport and variability based on long-term observations', *Journal of Physical Oceanography* **46**(4), 1045–1065.
URL: *http://dx.doi.org/10.1175/JPO-D-15-0154.1*

Pripp, T., Gammelsrød, T. & Krakstad, J. (2014), 'Physical influence on biological production along the western shelf of Madagascar', *Deep Sea Research Part II: Topical Studies in Oceanography* **100**, 174–183.
URL: *https://doi.org/10.1016/j.dsr2.2013.10.025*

Quartly, G. D., Buck, J. J., Srokosz, M. A. & Coward, A. C. (2006), 'Eddies around Madagascar—The retroflection re-considered', *Journal of Marine Systems* **63**(3), 115–129.
URL: *https://doi.org/10.1016/j.jmarsys.2006.06.001*

Quartly, G. & Srokosz, M. (2004*a*), 'Eddies in the southern Mozambique Channel', *Deep Sea Research Part II: Topical Studies in Oceanography* **51**(1), 69–83.
URL: *https://doi.org/10.1016/j.dsr2.2003.03.001*

Quartly, G. & Srokosz, M. (2004*b*), 'Following the fate of the East Madagascar Current'.

Raj, R. P., Peter, B. N. & Pushpadas, D. (2010), 'Oceanic and atmospheric influences on the variability of phytoplankton bloom in the southwestern Indian Ocean', *Journal of Marine Systems* **82**(4), 217–229.
URL: *https://doi.org/10.1016/j.jmarsys.2010.05.009*

Rakotoarinivo, A. W. (1998), Les petits poissons pélagiques de la région de Toliara Sud Ouest de Madagascar: biologie, écologie, exploitation et aménagement., PhD thesis, Université de Toliara.
URL: *http://hdl.handle.net/1834/9456*

Randriamahefasoa, T. M. S. (2013), Variability of summer rainfall over southwestern Madagascar, PhD thesis, University of Cape Town.

Reason, C. (2000), 'Multidecadal climate variability in the subtropics/mid-latitudes of the southern hemisphere oceans', *Tellus A: Dynamic Meteorology and Oceanography* **52**(2), 203–223.
URL: *https://doi.org/10.3402/tellusa.v52i2.12259*

Reason, C. & Mulenga, H. (1999), 'Relationships between south african rainfall and sst anomalies in the southwest Indian Ocean', *International Journal of Climatology: A Journal of the Royal Meteorological Society* **19**(15), 1651–1673.
URL: *https://doi-org.ezproxy.uct.ac.za/10.1002/(SICI)1097-0088(199912)19:15¡1651::AID-JOC439¿3.0.CO;2-U*

Ridderinkhof, W., Le Bars, D., Heydt, A. & Ruijter, W. (2013), 'Dipoles of the South East Madagascar Current', *Geophysical Research Letters* **40**(3), 558–562.
URL: *https://doi.org/10.1002/grl.50157*

Ridgway, K. & Dunn, J. (2007), 'Observational evidence for a Southern Hemisphere oceanic supergyre', *Geophysical Research Letters* **34**(13).
URL: *https://doi.org/10.1029/2007GL030392*

Rio, M., Guinehut, S. & Larnicol, G. (2011), 'New cnes-cls09 global mean dynamic topography computed from the combination of grace data, altimetry, and in situ measurements', *Journal of Geophysical Research: Oceans* **116**(C7).

Rio, M.-H. & Hernandez, F. (2004), 'A mean dynamic topography computed over the world ocean from altimetry, in situ measurements, and a geoid model', *Journal of Geophysical Research: Oceans* **109**(C12).

Rio, M.-H., Mulet, S. & Picot, N. (2014), 'Beyond GOCE for the ocean circulation estimate: Synergetic use of altimetry, gravimetry, and in situ data provides new insight into geostrophic and ekman currents', *Geophysical Research Letters* **41**(24), 8918–8925.
URL: *https://doi.org/10.1002/2014GL061773*

Risien, C. M. & Chelton, D. B. (2008), 'A global climatology of surface wind and wind stress fields from eight years of quikscat scatterometer data', *Journal of Physical Oceanography* **38**(11), 2379–2413.
URL: *https://doi.org/10.1002/2014GL061773*

Roughan, M. & Middleton, J. H. (2002), 'A comparison of observed upwelling mechanisms off the east coast of australia', *Continental Shelf Research* **22**(17), 2551–2572.
URL: *https://doi.org/10.1016/S0278-4343(02)00101-2*

Sætre, R. & Da Silva, A. J. (1984), 'The circulation of the Mozambique Channel', *Deep Sea Research Part A. Oceanographic Research Papers* **31**(5), 485–508.
URL: *https://doi.org/10.1016/0198-0149(84)90098-0*

Saji, N., Goswami, B., Vinayachandran, P. & Yamagata, T. (1999), 'A dipole mode in the tropical Indian Ocean', *Nature* **401**(6751), 360.
URL: *https://doi.org/10.1038/43854*

Saji, N. & Yamagata, T. (2003), 'Structure of sst and surface wind variability during Indian Ocean dipole mode events: Coads observations', *Journal of Climate* **16**(16), 2735–2751.
URL: *https://doi.org/10.1175/1520-0442(2003)016¡2735:SOSASW¿2.0.CO;2*

Schaeffer, A., Roughan, M. & Morris, B. D. (2013), 'Cross-shelf dynamics in a western boundary current regime: Implications for upwelling', *Journal of Physical Oceanography* **43**(5), 1042–1059.
URL: *https://doi.org/10.1175/JPO-D-12-0177.1*

Schaeffer, A., Roughan, M. & Wood, J. (2014), 'Observed bottom boundary layer transport and uplift on the continental shelf adjacent to a western boundary current', *Journal of Geophysical*

Research: Oceans **119**(8), 4922–4939.
URL: *https://doi.org/10.1002/2013JC009735*

Schott, F. A., Dengler, M. & Schoenefeldt, R. (2002), 'The shallow overturning circulation of the Indian Ocean', *Progress in Oceanography* **53**(1), 57–103.
URL: *https://doi.org/10.1016/S0079-6611(02)00039-3*

Schott, F. A. & McCreary, J. P. (2001), 'The monsoon circulation of the Indian Ocean', *Progress in Oceanography* **51**(1), 1–123.
URL: *https://doi.org/10.1016/S0079-6611(01)00083-0*

Schott, F. A., Xie, S.-P. & McCreary, J. P. (2009), 'Indian Ocean circulation and climate variability', *Reviews of Geophysics* **47**(1).
URL: *https://doi.org/10.1029/2007RG000245*

Shchepetkin, A. F. & McWilliams, J. C. (2005), 'The regional oceanic modeling system (ROMS): a split-explicit, free-surface, topography-following-coordinate oceanic model', *Ocean Modelling* **9**(4), 347–404.
URL: *https://doi.org/10.1016/j.ocemod.2004.08.002*

Shirtliffe, G. (1999), 'Quikscat science data product user's manual, overview and geophysical data products. version 1.0', *Jet Propulsion Laboratory, Pasadena, CA* .

Siedler, G., Rouault, M., Biastoch, A., Backeberg, B., Reason, C. J. & Lutjeharms, J. R. (2009), 'Modes of the southern extension of the east Madagascar current', *Journal of Geophysical Research: Oceans* **114**(C1).
URL: *https://doi.org/10.1029/2008JC004921*

Simhadri, K. K., Iyengar, S., Holyer, R. J., Lybanon, M. & Zachary, J. M. (1998), 'Wavelet-based feature extraction from oceanographic images', *IEEE Transactions on Geoscience and Remote Sensing* **36**(3), 767–778.
URL: *https://doi.org/10.1109/36.673670*

Sousa, M., Santos, F., Dias, J., Gómez-Gesteira, M. et al. (2016), 'How will somali coastal upwelling evolve under future warming scenarios?', *Scientific reports* **6**, 30137.
URL: *https://doi.org/10.1038/srep30137*

Srokosz, M., Robinson, J., McGrain, H., Popova, E. & Yool, A. (2015), 'Could the Madagascar bloom be fertilized by madagascan iron?', *Journal of Geophysical Research: Oceans* **120**(8), 5790–5803.
URL: *https://doi.org/10.1002/2015JC011075*

Stommel, H. (1948), 'The westward intensification of wind-driven ocean currents', *Eos, Transactions American Geophysical Union* **29**(2), 202–206.
URL: *https://doi.org/10.1029/TR029i002p00202*

Sverdrup, H. U. (1947), 'Wind-driven currents in a baroclinic ocean; with application to the equatorial currents of the eastern Pacific', *Proceedings of the National Academy of Sciences* **33**(11), 318–326.
URL: *http://www.pnas.org/content/33/11/318.short*

Swallow, J., Fieux, M. & Schott, F. (1988), 'The boundary currents east and north of Madagascar: 1. geostrophic currents and transports', *Journal of Geophysical Research: Oceans* **93**(C5), 4951–4962.
URL: *https://doi.org/10.1029/JC093iC05p04951*

Talley, L. D. (2013), 'Closure of the global overturning circulation through the indian, Pacific, and southern oceans: Schematics and transports', *Oceanography* **26**(1), 80–97.
URL: *URL: http://www.jstor.org/stable/24862019*

Tomczak, M. & Godfrey, J. S. (2013), *Regional oceanography: an introduction*, Vol. An Introduction (2nd Edition), New York: Pergamon Press.

Trenberth, K. E. (1997), 'The definition of el nino', *Bulletin of the American Meteorological Society* **78**(12), 2771–2777.
URL: *https://doi.org/10.1175/1520-0477(1997)078¡2771:TDOENO¿2.0.CO;2*

Ullgren, J., van Aken, H., Ridderinkhof, H. & de Ruijter, W. (2012), 'The hydrography of the Mozambique Channel from six years of continuous temperature, salinity, and velocity observations', *Deep Sea Research Part I: Oceanographic Research Papers* **69**, 36–50.

Uz, B. M. (2007), 'What causes the sporadic phytoplankton bloom southeast of Madagascar?', *Journal of Geophysical Research: Oceans* **112**(C9).
URL: *https://doi.org/10.1029/2006JC003685*

Vazquez-Cuervo, J., Dewitte, B., Chin, T. M., Armstrong, E. M., Purca, S. & Alburqueque, E. (2013), 'An analysis of SST gradients off the Peruvian Coast: The impact of going to higher resolution', *Remote Sensing of Environment* **131**, 76–84.
URL: *https://doi.org/10.1016/j.rse.2012.12.010*

Vázquez, D. P., Atae-Allah, C. & Escamilla, P. L. L. (1999), 'Entropic approach to edge detection for sst images', *Journal of Atmospheric and Oceanic Technology* **16**(7), 970–979.
URL: *https://doi.org/10.1175/1520-0426(1999)016¡0970:EATEDF¿2.0.CO;2*

Veitch, J. A. (2009), 'Equilibrium dynamics of the Benguela system: a numerical modelling approach'.
URL: *http://hdl.handle.net/11427/12153*

Veitch, J., Penven, P. & Shillington, F. (2010), 'Modeling equilibrium dynamics of the benguela current system', *Journal of Physical Oceanography* **40**(9), 1942–1964.
URL: *https://doi.org/10.1175/2010JPO4382.1*

Vic, C., Gula, J., Roullet, G. & Pradillon, F. (2018), 'Dispersion of deep-sea hydrothermal vent effluents and larvae by submesoscale and tidal currents', *Deep Sea Research Part I: Oceanographic Research Papers* .
URL: *https://doi.org/10.1016/j.dsr.2018.01.001*

Voldsund, A. (2011), The dynamics of the East Madagascar Current system and its influence on the biological production associated to the shelf-an observational study, Master's thesis, The University of Bergen.
URL: *http://hdl.handle.net/1956/5198*

Wentz, F. J. (1992), 'Measurement of oceanic wind vector using satellite microwave radiometers', *IEEE Transactions on Geoscience and Remote Sensing* **30**(5), 960–972.

Wilkinson, C. R., Lindén, O., Cesar, H. S., Hodgson, G., Rubens, J. & Strong, A. E. (1999), 'Ecological and socioeconomic impacts of 1998 coral mortality in the Indian Ocean: An enso impact and a warning of future change?', *Ambio* **28**(2), 188.
URL: *http://hdl.handle.net/1783.1/82153*

Wilson, C. & Qiu, X. (2008), 'Global distribution of summer chlorophyll blooms in the oligotrophic gyres', *Progress in Oceanography* **78**(2), 107–134.
URL: *https://doi.org/10.1016/j.pocean.2008.05.002*

Wu, R. & Kirtman, B. P. (2004), 'Understanding the impacts of the Indian Ocean on enso variability in a coupled gcm', *Journal of climate* **17**(20), 4019–4031.
URL: *https://doi.org/10.1175/1520-0442(2004)017¡4019:UTIOTI¿2.0.CO;2*

Wyrtki, K. (1971), Oceanographic atlas of the international Indian Ocean expedition, national science foundation publication, oce, Technical report, NSF 86–00-001, Washington, DC.

Wyrtki, K. (1973), Physical oceanography of the Indian Ocean, *in* 'The biology of the Indian Ocean', Springer, pp. 18–36.

Yamagata, T., Behera, S. K., Luo, J.-J., Masson, S., Jury, M. R. & Rao, S. A. (2004), 'Coupled ocean-atmosphere variability in the tropical Indian Ocean', *Earth's Climate* pp. 189–211.
URL: *https://doi.org/10.1029/147GM12*

Yu, L. & Rienecker, M. M. (1999), 'Mechanisms for the Indian Ocean warming during the 1997–98 el nino', *Geophysical Research Letters* **26**(6), 735–738.
URL: *https://doi-org.ezproxy.uct.ac.za/10.1029/1999GL900072*

Appendix A

Appendix

Upwelling index extension

To investigate the inter-annual variability of the coastal upwelling, we combined the MUR SST and AVHRR SST (Version 5) to extend the upwelling index (Equation 4.2) in each Core. There is limited SST product which can cover a long-term period beyond 30 years. The AVHRR SST covers the period from 1982 to 2009 within a 4 km resolution grid. The MUR SST covers the period from 2013 to 2017 within 1.1 km resolution. Figure A.1 shows the correspondence of time series between the upwelling index derived from AVHRR SST and MUR SST. Both time series are combined to get 35 years of upwelling index time series.

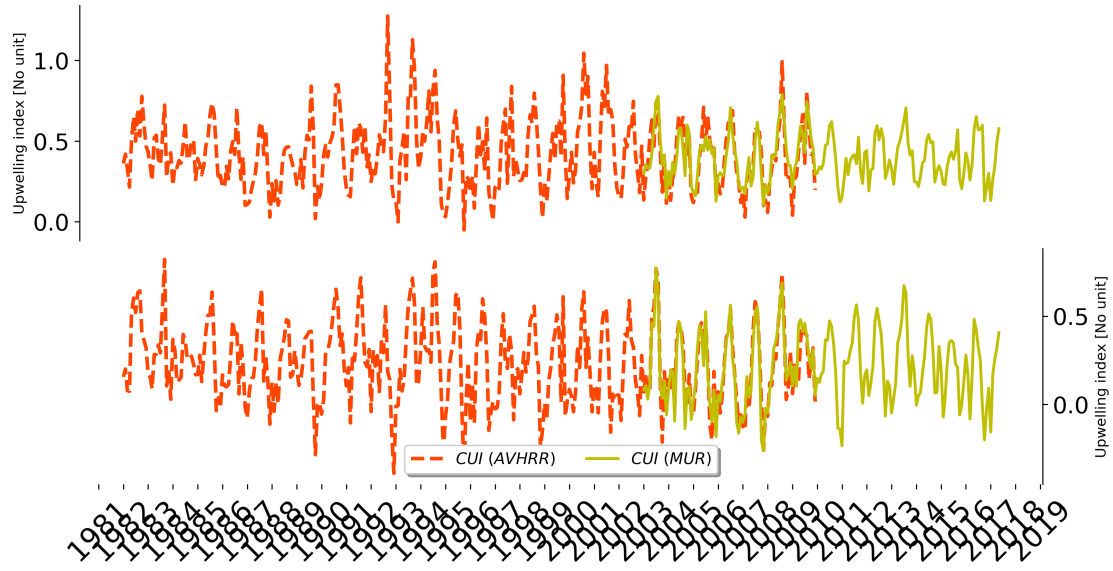

Figure A.1: Time series of upwelling index reconstructed in each Core. Time series coloured in red is the upwelling index derived from AVHRR SST product. Time series coloured in yellow is the upwelling index retrieved from MUR SST product.

Upwelling index and Chlorophyll response

Figure A.2 and Figure A.3 show the time series of chlorophyll concentration (green) and the upwelling index (black) in Core 1. The chlorophyll time series is the combination between SeaWIFS, 4 km grid resolution during the period of 1997 to 2002, and the MODIS AQUA, 4 km grid resolution during the period of 2003 to 2016, in monthly time scale. The upwelling index is the upwelling index utilized in Chapter 6.

Figure A.2 confirms the correspondence between the upwelling index and Chlorophyll concentration generated for Core 1.

Figure A.3 also highlights the high linear relationship the upwelling index and Chlorophyll concentration in Core 2.

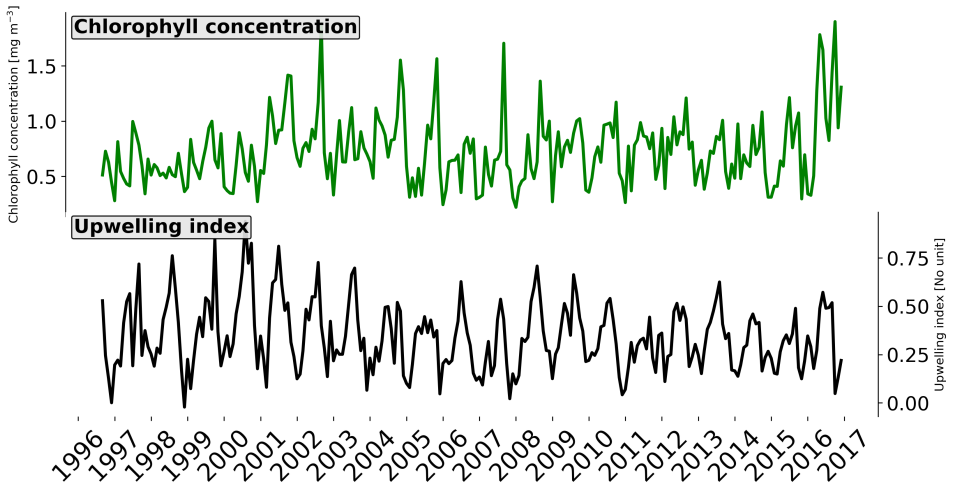

Figure A.2: Time series of chlorophyll concentration (green) and the upwelling index (black) in Core 1

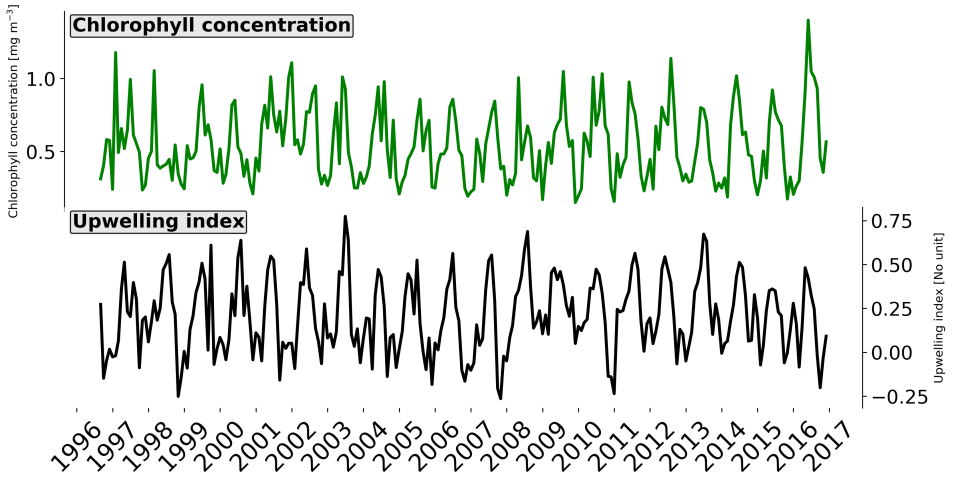

Figure A.3: Time series of chlorophyll concentration (green) and the upwelling index (black) in Core 2

Figure A.4 show the wavelet analysis of the Chlorophyll A concentration at the south of Madagascar. Modis AQUA, 1 km resolution grid, is used.

Four stations, Core 1 and Core 2 and southern extension of EMC and SMACC, have been selected to represent the variation of chlorophyll-a concentration at south of Madagascar.

The wavelet analysis of chlorophyll-a data is computed to analyse the periodicity and frequency of the time series in each station in the map (bottom right).

The first wavelet power in station 1 shows a significant bi-annual cycle during the period 2005 to 2006 and 2007 until 2013. This means that the chlorophyll-a has a two high consecutive production periods, i.e. summer production and winter production.

The chlorophyll A concentration is very high in station 2. A strong energy is observed in 12 months period and low in 6 months for the Station 2 in the wavelet map and the spectral analysis. This is an indication that high chlorophyll A production occurs generally during the austral winter and remains intense throughout the years.

The wavelet power shows a significant energy of signal in the 12-month period continues and remains stronger throughout the year in station 3. The global power spectrum also confirm that an important energy reach the 95% of significance in station 2. Indeed, station 3 is dominated by seasonality marked by an important peak at 12 month period.

Station 4 has the lowest chlorophyll A production. The maximum concentration is about 1/5 of the maximum of chlorophyll A concentration in station 1. The periodicity is dominated by an annual cycle similar than in station 3.

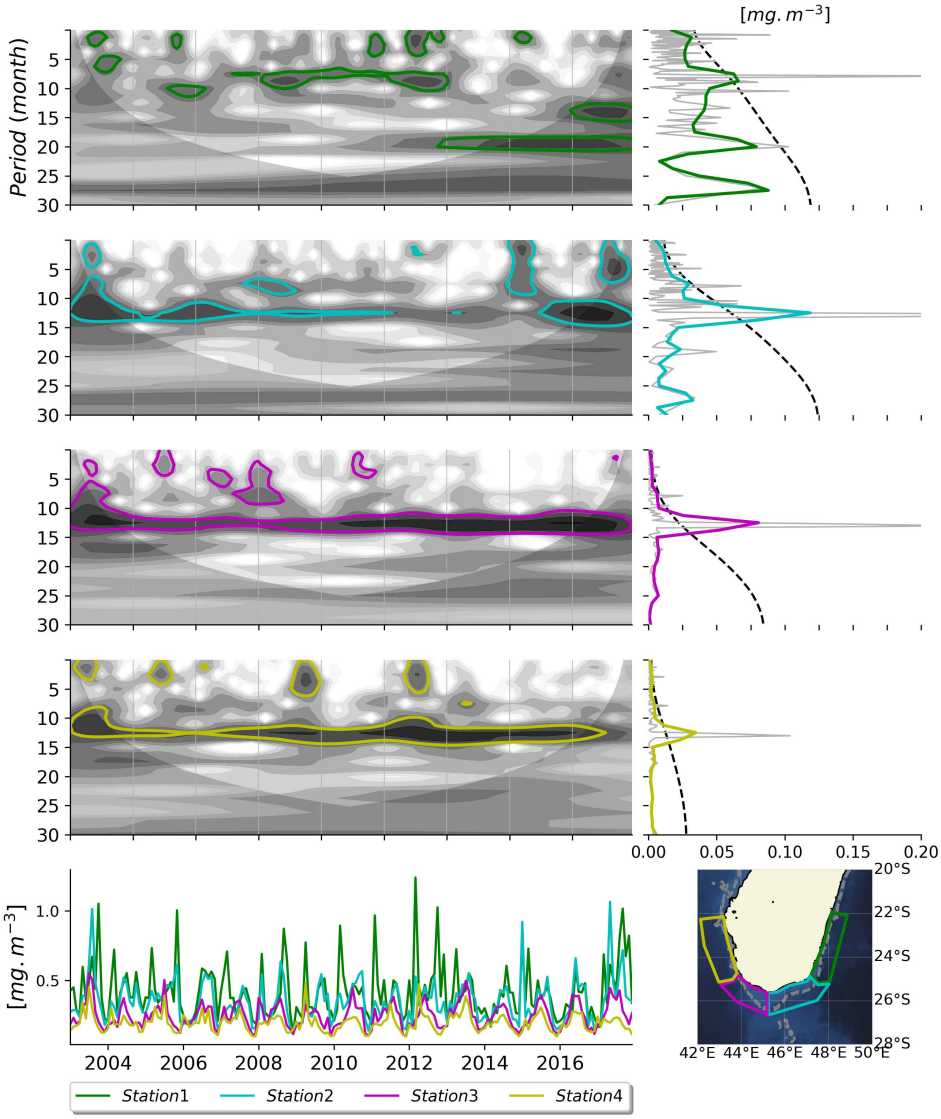

Figure A.4: Periodicity of chlorophyll-A concentration using wavelet Analysis. Four panels on the top right are wavelet power spectrum of the monthly chlorophyll-A concentration of each station encountoured with respective colors. Contours color represents specific station where time series were extracted: Green represents to station 1, cyan represents to station 2, magneta corresponds to station3 and yellow corresponds to station 4. Contours denote the 95% of significance levels above a red noise background spectrum. Cross-hatched and shaded areas indicate the "*cone of influence*" where the edge effects become important. Four panels on the top left are the global wavelet power spectrum assuming the same significance level and background spectrum as in the wavelet power spectrum for each station. Above dashed lines correspond to the 95% significance level. Left bottom panel contain time series of chlorophyll-A concentration in monthly time scale of each station. Right bottom panel illustrate stations on a map where the time series for the wavelet analysis are extracted.

Approximation of the Coastal and Regional Ocean COmmunity model (CROCO) equations

The following section will describe the approximated equations solved by CROCO numerical model to reproduce the state of the ocean.

• **Equations of motion**

Here below are the primitive equations of motion, under Boussinesq and hydrostatic approximation for an incompressible ocean (Shchepetkin & McWilliams 2005), solved in CROCO in Cartesian coordinates:

$$\frac{\partial u}{\partial t} + \vec{v}.\nabla u - fv = -\frac{\partial \phi}{\partial x} + F_u + D_u \tag{A.1}$$

$$\frac{\partial v}{\partial t} + \vec{v}.\nabla v + fu = -\frac{\partial \phi}{\partial y} + F_v + D_v \tag{A.2}$$

$$\frac{\partial T}{\partial t} + \vec{v}.\nabla T = F_T + D_T \tag{A.3}$$

$$\frac{\partial S}{\partial t} + \vec{v}.\nabla S = F_S + D_S \tag{A.4}$$

$$\frac{\partial \phi}{\partial z} = -\frac{\rho g}{\rho_o} \tag{A.5}$$

$$\frac{\partial u}{\partial x} + \frac{\partial v}{\partial y} + \frac{\partial w}{\partial z} = 0 \tag{A.6}$$

$$\rho = \rho(T, S, P) \tag{A.7}$$

- Equation A.1 and A.4: the horizontal momentum equations.

- Equation A.3 and A.4: the advection-diffusion governing the potential temperature. T and salinity S.

- Equation A.5: the hydrostatic ad mass balance.

- Equation A.6: the continuity equation for an incompressible fluid.

- Equation A.7: the equation of state for seawater (Shchepetkin & McWilliams 2005).

• **Vertical Boundary Conditions**

At the surface and bottom boundary conditions, CROCO introduces external forcing terms through vertical viscosity and diffusivity.

1) At the surface (z=ζ(x,y,t)) as:

Atmospheric wind stress at sea surface, in x and y directions:

$$K_v \frac{\partial u}{\partial z} = \frac{\tau_s^x}{\rho_o}(x,y,t) \tag{A.8}$$

$$K_v \frac{\partial v}{\partial z} = \frac{\tau_s^y}{\rho_o}(x,y,t) \tag{A.9}$$

Thermal and freshwater fluxes at the sea surface:

$$K_T \frac{\partial T}{\partial z} = \frac{Q_T}{\rho_o C_p} \tag{A.10}$$

$$K_S \frac{\partial S}{\partial z} = \frac{(E_v - P_r)S}{\rho_o} \tag{A.11}$$

Vertical velocities associated with the variation of the sea surface:

$$w = \frac{\partial \zeta}{\partial t} \tag{A.12}$$

The surface wind stress components are given by:

$$\tau_s^x = \rho_{air} C_D \sqrt{u_{10}^2 + v_{10}^2}.u_{10} \tag{A.13}$$

and

$$\tau_s^y = \rho_{air} C_D \sqrt{u_{10}^2 + v_{10}^2}.v_{10} \tag{A.14}$$

2) At the seafloor: z=-H(x,y) as:

Momentum transferred into the ocean by friction at seafloor:

$$K_v \frac{\partial u}{\partial z} = \frac{\tau_b^x}{\rho_o}(x,y,t) \tag{A.15}$$

$$K_v \frac{\partial v}{\partial z} = \frac{\tau_b^y}{\rho_o}(x,y,t) \tag{A.16}$$

Vertical thermal and salt fluxes at the sea-floor (which is non-existent):

$$K_T \frac{\partial T}{\partial z} = 0 \tag{A.17}$$

$$K_S \frac{\partial S}{\partial z} = 0 \tag{A.18}$$

Non-crossing of the topography by the flow at sea-floor:

$$-w + \vec{v}.\nabla uH = 0 \tag{A.19}$$

The bottom stress is parametrized by a choice between linear, quadratic, or logarithmic terms. Bottom friction is established as:

$$\tau_b^x = (\gamma_1 + \gamma_2 \sqrt{u^2 + v^2}).u \tag{A.20}$$

and

$$\tau_b^y = (\gamma_1 + \gamma_2 \sqrt{u^2 + v^2}).v \tag{A.21}$$

Symbols in the equations:

• x,y,z - are the zonal, meridional and vertical directions (m) in the Cartesian coordinate system.

• u,v,w - are the components of the vector velocity $\vec{v}$ (m s^{-1}) in x,y,z respectively.

• t - is the time in seconds (s).

- f - is the Coriolis parameter (s^{-1}).
- ϕ - is the dynamic pressure (m^2 s^{-2}).
- F_u, F_v, F_T, F_S - are the possible forcings terms.
- D_u, D_v, D_T, D_S - are the dissipative terms.
- T - is the potential temperature (°C).
- S - is the salinity (psu)
- $\vec{g}$ - is the acceleration of gravity (m s^2).
- ρ - is the seawater density (kg m^{-3}).
- ρ_o - is the mean seawater density (kg m^{-3}).
- P - is the total pressure (N m^{-2} or Kg m^{-2}).
- ζ - is the sea surface variation (m).
- τ_s^x, τ_s^y - are the surface wind stress (N m^{-2}), in x and y directions respectively.
- τ_b^x, τ_b^y - are the bottom wind stress (N m^{-2}), in x and y directions respectively.
- Q_T - is the surface heat flux (W m^{-2}).
- K_v - is the coefficient of vertical eddy viscosity (m^2 s^{-1}).
- K_T, K_S - are coefficients of vertical eddy diffusivity (m^2 s^{-1}).
- E_r - is the evaporation rate (cm day^{-1}).
- P_r - is the precipitation rate (cm day^{-1}).
- C_p - is the heat capacity of seawater (J kg^{-1} °C).
- H - is the total ocean depth (m).
- u_{10}, v_{10} - are the horizontal components of the wind vector in x and y respectively, measured at 10 m above sea level.
- C_D - is a non-dimensional wind-drag coefficient.
- ρ_{air} - is the density of atmospheric air (kg m^{-3}).
- γ_1 - is the coefficient of linear bottom friction.
- γ_2 - is the coefficient of quadratic bottom friction.

SMACC extension

Figure A.5 shows the second portion of the SADCP transects in Figure 5.3. Figure A.5 reveals the extension of the SMACC which can reach the southerntip toward the Core 1. This demonstrated the result seen in the Lagrangian experimentation explaining that the upwelled water

arrive from the SMACC to fill the Core 1.

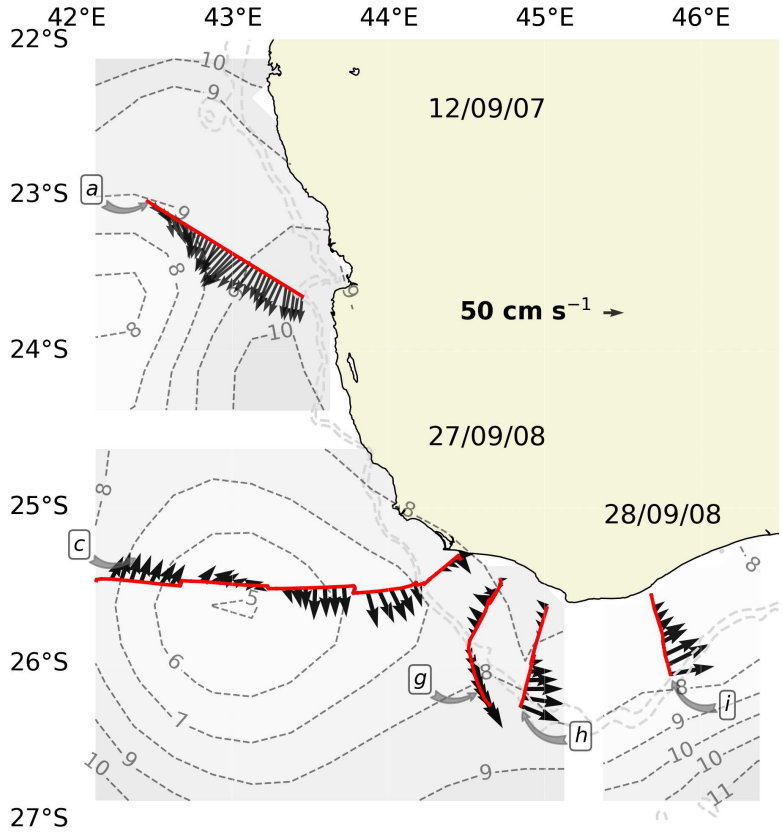

Figure A.5: Second part of the measured near surface current from SADCP data on board the R/V *Fridtjof Nansen* shown in Figure 5.3. Transect *a*, *c*, *g* are transect of SADCP in Figure 5.3 and Sea Surface Height from AVISO associated with the same period of the SADCP measurement. Transect *h*, *i* are transect of SADCP showing the eastern extension of the coastal jet and the Sea Surface Height from AVISO associated.

Mean surface currents

Figure A.6 shows the mean geostrophic currents derived from mean dynamic topographies from model solution, satellite observations (RIO 2005, CLS 2009, CLS 2013, Maximenko 2015) and ARGO floats displacement (ANDRO).

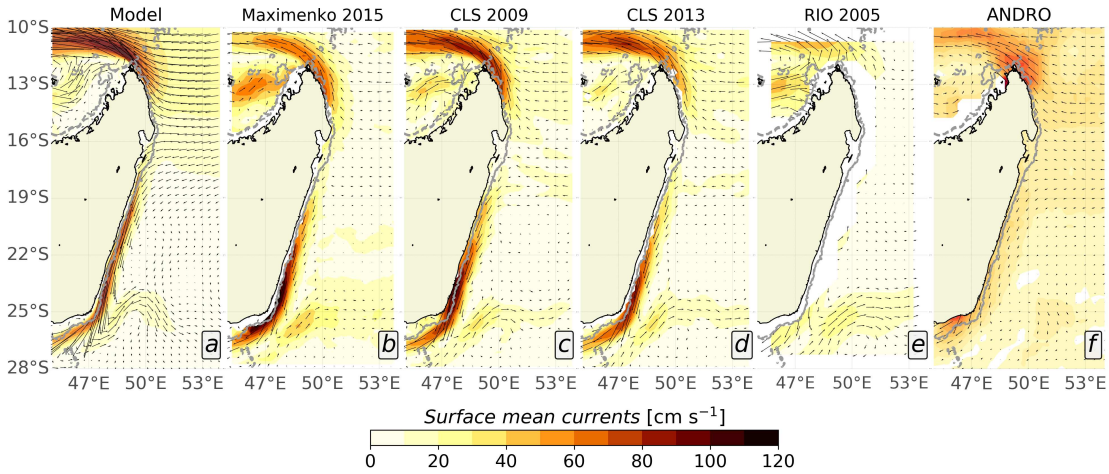

Figure A.6: Mean surface currents derived from different mean dynamic topographies: a- Model solutions, b- (Maximenko et al. 2009), c- CLS-2009 (Rio et al. 2011), d- CLS-2013 (Rio et al. 2014), e- RIO-2005 (Rio & Hernandez 2004) and from ARGO floats surface displacement f- (Ollitrault & Rannou 2013).